Study of an Improved Comprehensive Magnetic Field Inversion Analysis for *Swarm*

Nils Olsen, Terence J. Sabaka, and Luis R. Gaya-Pique

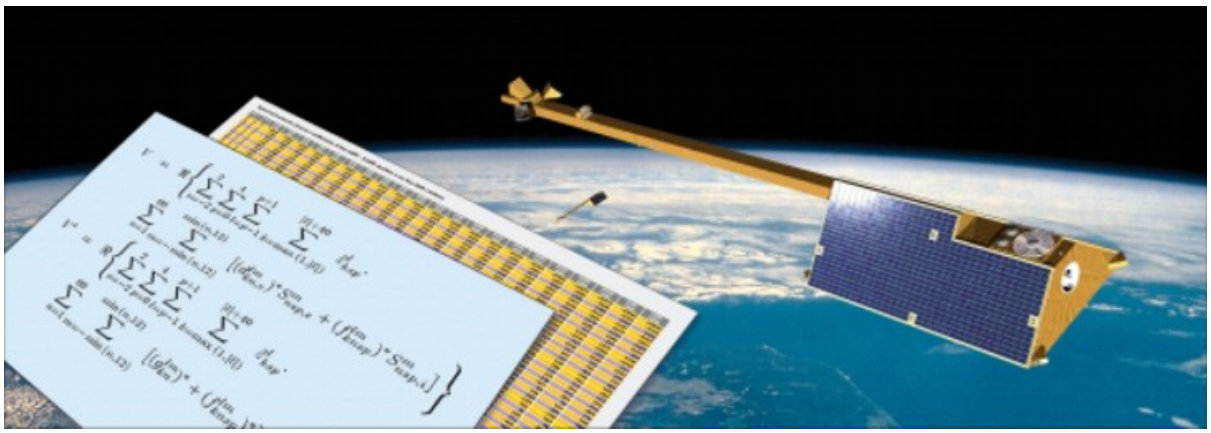

Danish National Space Center (DNSC)

DANISH NATIONAL
SPACE CENTER

Draft Final Report

March 15, 2007

Planetary Geodynamics
GSFC
NASA
698
Studying the Solid Earth and Planets from Space

Contents

Chapter 1

Introduction

This report describes the results of activities performed during the Science Study "Study of an Improved Comprehensive Magnetic Field Inversion Analysis for *Swarm*" (ESTEC Contract No. 11570/05/NL/AR). The work has been conducted by Nils Olsen and Terence J. Sabaka, with strong support from Alexei Kuvshinov, Luis R. Gaya-Pique and Lars Tøffner-Clausen.

The goal of the study is to investigate the improvement in modeling Earth's magnetic field that can be obtained using advanced algorithms for analyzing *Swarm* magnetic field observations, including the differences of the magnetic field measured by the two lower satellites.

The proposed activity is a natural extension of the *Swarm* End-to-End Mission Performance Analysis [Olsen et al., 2004] performed by our team during Phase A of the mission, and the outcome of that activity will be used as a starting point for the current study.

The objectives of this study are:

- An adaptation of the Comprehensive Inversion (CI) approach to account for magnetic vector differences, and to treat the magnetic data in the measurement frame.
- An optimization of the analysis chain to be able to "quickly" respond to questions related to magnetic field mission performance.
- An analysis of the impact of product quality degradation on the mission performance related to geomagnetic field models.

Regarding the first objective, improvement is expected by taking advantage of the constellation aspect through treatment of the lower satellite pair vector data as magnetic field differences, together with an optimal combination with data from the high satellite. This requires a design and implementation of procedures for handling the differences of the vector magnetic data and tuning the comprehensive inversion approach to include differences in an optimal sense. It also includes an in-flight co-estimation of the alignment parameters defining the rotation between the vector magnetometer and the star imager. A mission performance analysis with the most recent choices of orbits and launch dates will be performed including specific "failure" cases. During the development process of improving the End-to-End mission performance simulator, special emphasis will be put on optimizing procedures to arrive at "quick" response tools for assessment of mission performance relevant to models of the internal magnetic field. This will be used during the development and first operational phase of the mission.

1.2 Study Logic

The study has been organized in three main tasks and structured as indicated in Figure 1.1, while Figure 1.2 shows the work breakdown structure.

The forward scheme for the production of the synthetic data is described in chapter 2.

Impact of the data sampling rate on the recovery of the lithospheric field is discussed in chapter 3.

Lithospheric field recovery using magnetic field differences measured by the lower satellite pair (*Swarm A* and *B*) is the topic of chapter 4.

While all the results obtained in chapters 3 and 4 are obtained using perfectly aligned data (i.e. vector data in the NEC system), a mult-satellite in-flight alignment is discussed in chapter 5.

A combination of the two approaches, and a first application to some test cases, is discussed in chapter 6. Application to the mission baseline and various failure cases is presented in chapter 7. Chapter 8 presents the results of an along-track analysis of the magnetic field

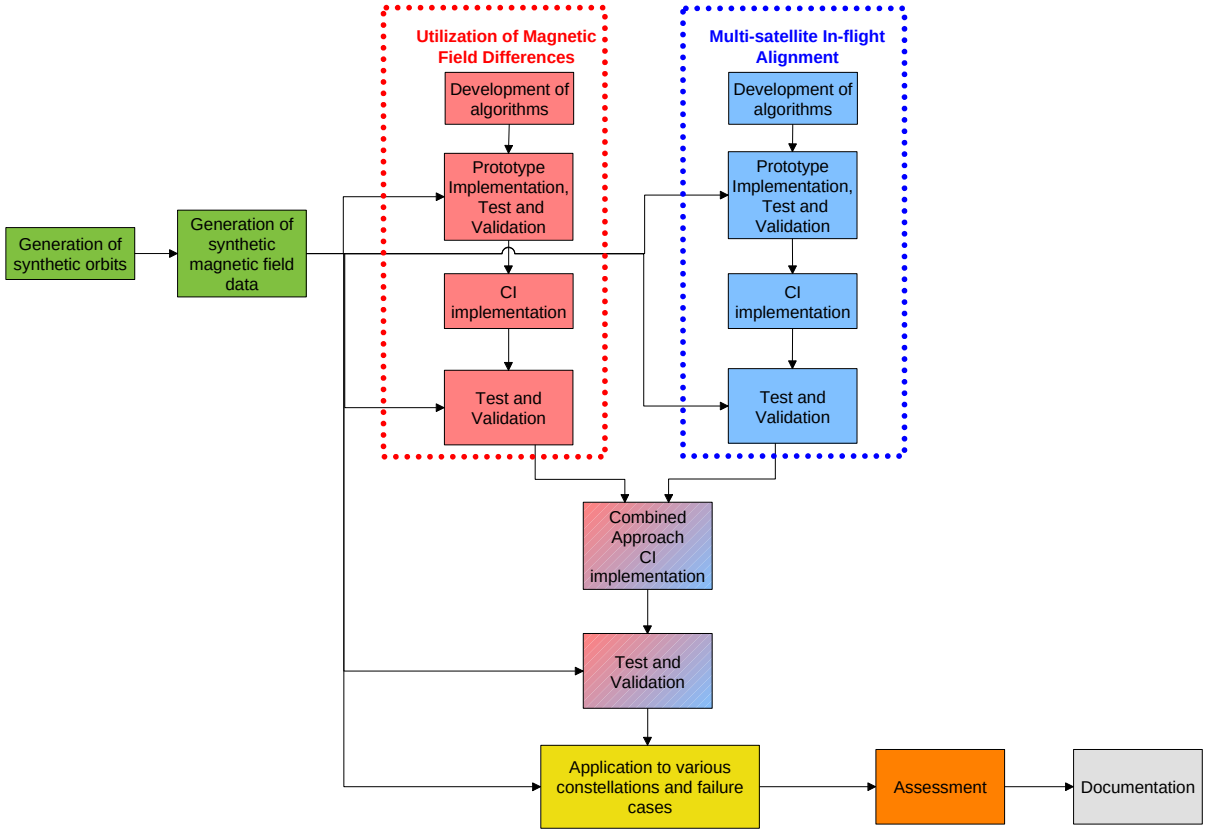

Figure 1.1: Study Logic

residuals (data minus model predictions) for the mission baseline analysis and a few failure cases. Finally, chapter 9 gives recommendations for future studies.

1.3 Test quantities and criteria

For the present study we used similar assesment criteria as for the Phase A E2E activities. In particular:

- **Spectra of differences, degree error, and accumulated error**. The Mauersberger-Lowes spectrum (degree variance), R_n, of the differences between the original and the recovered model coefficients, $\Delta g_n^m, \Delta h_n^m$, in combination with the spectrum of the original model, has been used to evaluate a recovered model. Degree error is defined as $\sqrt{R_n}$, and accumulated error at degree n is defined as $c_n = \sqrt{\sum_{l=l_{\min}}^{n} R_l}$.

- **Spectra of differences, azimuthal error**. Although the R_n spectrum provides the mean-squared field magnitude at Earth's surface for degree n, it is rotationally invariant and provides no phase information. Alternatively, one may look at the power spectrum as a function of the ratio $a = m/n$, reminicient of an azimuthal number, which varies from 0 for zonal terms to 1 for g_n^n and -1 for h_n^n sectorial terms. This spectrum, denoted as R_a, provides the mean-squared field magnitude at Earth's surface for azimuth a. Because the cardinality of the set of a values is usually large, R_a is often smoothed in order to reveal general trends.

Figure 1.2: Work breakdown structure

- **Degree correlation**, ρ_n, [Langel and Hinze, 1998, eq. 4.23] between the original and the recovered model has also been used to evaluate a recovered model. Models are considered compatible up to that degree n where ρ_n drops below $\sqrt{2} \approx 0.7$ since this corresponds to an angle greater than 45° between the recovered and the original model vector.

- **Sensitivity matrix** is the relative error of each coefficient in a degree versus order matrix and was used to investigate systematic errors. The difference (recovered minus original model) of all the coefficients is determined and subsequently normalized by the mean spectral amplitude of the associated degree n.

- Finally, **global maps** of field differences (for instance of B_r) between the original and the recovered model are used to find geographically confined deficiencies in the recovered models, for instance in connection with the size of the polar gaps.

1.4 Meetings and Workshops

The following meetings and workshops have been held in connection with the activities described in this report:

- **Kick-off meeting (KO)** at DNSC Copenhagen/Denmark, January 27, 2006
- **Progress meeting 1 (PM1)** at DNSC Copenhagen/Denmark, March 29, 2006
- **Mid Term Review (MTR)** at ESTEC Noordwijk/Netherlands, June 26, 2006
- **Progress meeting 2 (PM2)** at DNSC Copenhagen/Denmark, November 3, 2006
- **Working Meeting 1 (WM1)** at DNSC Copenhagen/Denmark, February 2, 2007

Chapter 2

Forward Calculation

This chapter describes the production of synthetic data for the simulated *Swarm* mission. Involved in this task are the working packages WP-1100 "Orbit Determination", and WP-1200 "Magnetic Field Generation".

2.1 Introduction

Figure 2.1 shows a flow chart of the forward scheme.

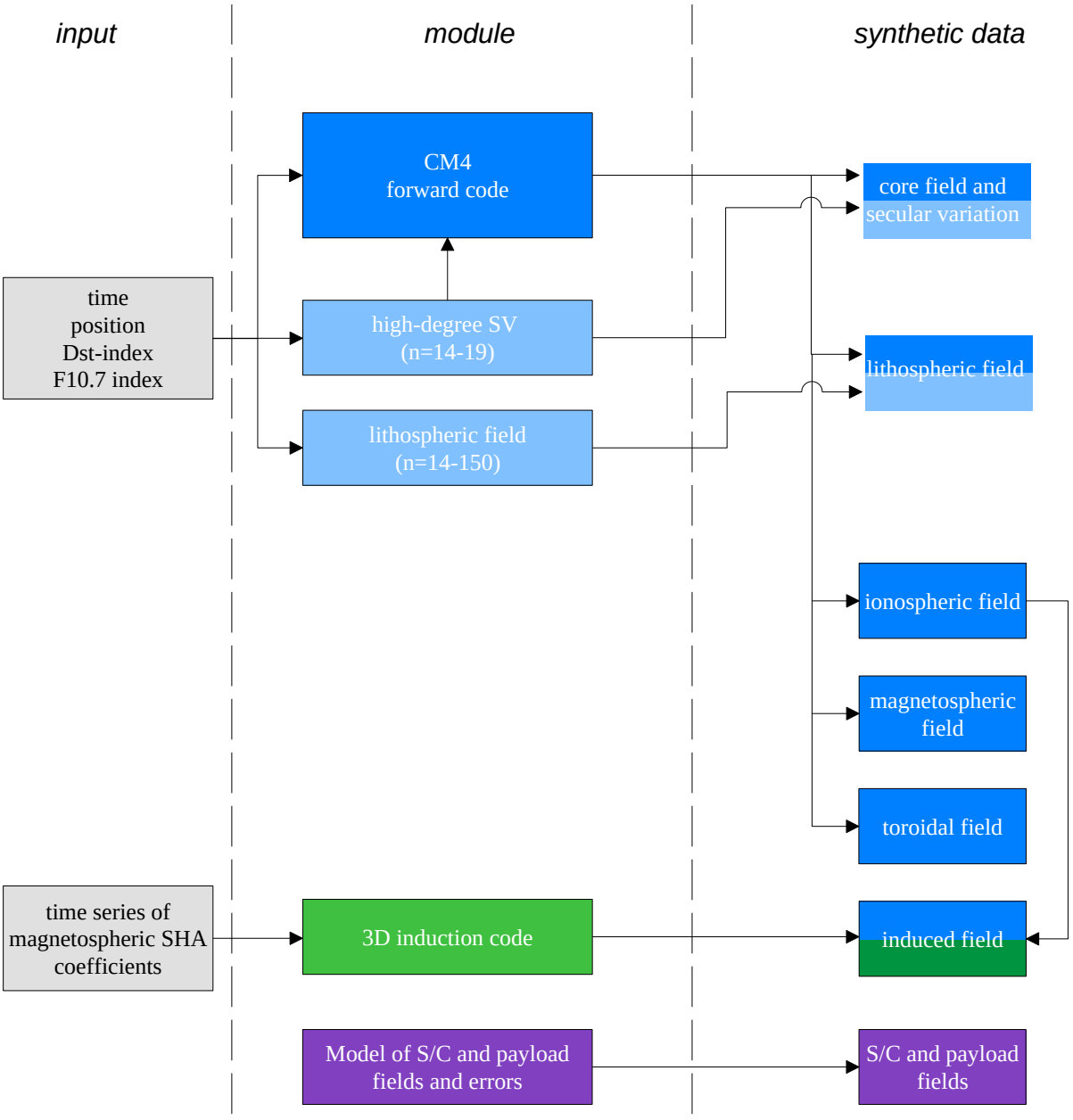

Figure 2.1: Flow chart of the forward scheme.

2.2 A fast approach for generating synthetic orbits

This section describes the approach that we developed for calculating synthetic orbits (positions). This activity relates to WP 1100 "Orbit Determination".

In the following we only consider the two effects that have the largest impact on orbit evolution

- secular variation in the *Right Ascension of the Ascending Node*, Ω, because of Earth's oblateness, and
- decay of the orbit altitude due to air drag.

For a circular orbit with semi-major axis a_{sma} and orbit inclination i the nodal drift rate $\dot{\Omega}$ due to Earth's oblateness (expressed by the dimensionless geopotential coefficient $J_2 = 1082.63 \cdot 10^{-6}$) in the *International Celestial Reference Frame* (ICRF) is given by

$$\dot{\Omega} = -1.5 n J_2 \left(\frac{a}{a_{sma}}\right)^2 \cos(i) \tag{2.1}$$

$$= -2.06474 \cdot 10^{14} a_{sma}^{-7/2} \cos(i) \tag{2.2}$$

[Wertz and Larson, 1999, eq. 6-19], where a is Earth's (equatorial) radius and n is mean motion. Orbit period T_p is

$$T_p = 2\pi \sqrt{\frac{a_{sma}^3}{\mu}}, \tag{2.3}$$

with $\mu = 3.986005 \cdot 10^{14} \mathrm{m}^3\mathrm{s}^{-2}$ as the geocentric gravitational constant.

In our approach we first calculate the position vector $\mathbf{r_{ORF}}$ of a circular orbit of radius a_{sma} in a coordinate system that is fixed with the orbit plane (Orbit Reference Frame, ORF). Its z-axis coincides with the z-axis of the *International Celestial Reference Frame* ICRF, but the orbit plane is declined w.r.t. the z axis by the inclination i:

$$\mathbf{r}_{ORF} = \begin{pmatrix} x_{ORF} \\ y_{ORF} \\ z_{ORF} \end{pmatrix} = a_{sma} \begin{pmatrix} \cos(\alpha) \\ \sin(\alpha)\cos i \\ \sin(\alpha)\sin i \end{pmatrix} \tag{2.4}$$

with

$$\alpha = 2\pi \frac{t - t_0}{T_p} + \nu$$

where t is time, t_0 is epoch, and ν is mean anomaly at epoch t_0. We then rotate about the z-axis by $\beta = (t - t_0)\dot{\Omega} - \Omega$ to get position in ICRF coordinates:

$$\begin{pmatrix} x_{ICRF} \\ y_{ICRF} \\ z_{ICRF} \end{pmatrix} = \begin{pmatrix} +\cos\beta & -\sin\beta & 0 \\ +\sin\beta & +\cos\beta & 0 \\ 0 & 0 & 1 \end{pmatrix} \begin{pmatrix} x_{ORF} \\ y_{ORF} \\ z_{ORF} \end{pmatrix} \tag{2.5}$$

Finally, a rotation about the z-axis by -GAST (where GAST is *Greenwich Apparent Sidereal Time*, cf. Seeber [2004]) yields position and velocity in the coordinates of the *International Terrestrial Reference Frame*, ITRF:

$$\begin{pmatrix} x_{ITRF} \\ y_{ITRF} \\ z_{ITRF} \end{pmatrix} = \begin{pmatrix} +\cos GAST & +\sin GAST & 0 \\ -\sin GAST & +\cos GAST & 0 \\ 0 & 0 & 1 \end{pmatrix} \begin{pmatrix} x_{ICRF} \\ y_{ICRF} \\ z_{ICRF} \end{pmatrix} \tag{2.6}$$

After the gravity field the second largest force acting on a satellite at this altitude is the atmospheric drag. The modeling of the atmospheric density is based on the MSIS-86 model [Hedin, 1987] making use of the 3-hourly geomagnetic indices (Ap), as well as the daily solar flux ($F_{10.7}$) and the average solar flux over 3 solar rotations (81 days).

Orbit calculation is done using the following steps:

1. Initial conditions a_{sma}, ν, and Ω are obtained for epoch t_0
2. positions $\mathbf{r}_{ITRF}$ are calculated for one day, i.e. for $t = t_0 - t_0 + 86400$ s and 1 min sampling rate, assuming constant values for a_{sma} and T_p.
3. Air-density ρ is calculated for each location from the MSIS model [Hedin, 1987, 1991], considering the geomagnetic activity Ap and solar radiation $F_{10.7}$
4. The decrease Δa_{sma} of the semi-major axis a_{sma} due to air drag during the day in consideration is calculated in the following way: According to eq. (4.431) of Flury [2000], the change of the semi-major axis *per orbit* is

$$\Delta a_{sma} = -2\pi\overline{\rho}\frac{a_{sma}^2}{B} \tag{2.7}$$

   where $\overline{\rho} = \frac{1}{T_p}\int_0^{T_p} \rho dt$ is the mean air density, averaged over one orbit,

$$B = \frac{m}{AC_D} \tag{2.8}$$

   is the ballistic coefficient, m is satellite mass, A is the satellite cross-section area, and C_D is the drag coefficient. Since the number of orbits per day is 86400 s/T_p, the change of the semi-major axis *per day* is

$$\Delta a_{sma} = -\overline{\rho}\frac{\sqrt{\mu a_{sma}}}{B} \tag{2.9}$$

   where $\overline{\rho} = \frac{1}{1\text{day}}\int_0^{1\text{day}} \rho dt$ is the mean air density, averaged over one day.
5. The decrease of a_{sma} is linearly interpolated (distributed) over the 24 hours in consideration:

$$\mathbf{r}_{ICRF}^{\text{final}} = \left[1 + (t - t_0)\frac{\Delta a_{sma}}{a_{sma}}\right]\mathbf{r}_{ICRF} \tag{2.10}$$

6. New staring values a_{sma}, ν, and Ω for the new epoch $t_0 = t_0 + 1$ day are calculated and the above steps 2 to 6 are repeated for the next day, until the end of the mission.

2.2.1 Validation of the method

The method is tested by comparison with the observed orbit decay of the CHAMP satellite. For this comparison we used the following initial conditions for the CHAMP orbit: inclination $i = 87.255°$, semi-major axis $a_{sma} = a + 457.1$ km, $\nu = 63.816°$, and $\Omega = 144.43°$ for epoch $t = 213.0$ MD2000 (August 1, 2000, 00:00 UT).

A critical issue is the value of the ballistic coefficient $B = \frac{m}{AC_D}$. A is the effective satellite cross section, which depends on the actual flight direction and on the strength and direction of across-track winds. The cross section area perpendicular to the CHAMP x-axis (which is the nominal flight direction) is $A_x = 0.74$ m^2; the value for the two other axes are $A_y = 3.12$ m^2 and

$A_z = 4.2$ m^2. Initial CHAMP satellite mass was $m = 505$ kg. Using this mass, A_x as the cross section area, and a value of $C_D = 2.2$ results in a ballistic coefficient of $B = 170$ kg/m^2. This value is, however, much lower than those based on observations of the actual CHAMP orbit decay [Liu and Lühr, 2005]. According to Hermann Lühr (personal communication, 2006), an effective cross section area of $A = 0.9$ m^2 and a value of $C_D = 2.3 - 2.4$, resulting in $B = 230$ kg/m^2 is in much better agreement with the observations. For the following comparison we therefore used $B = 230$ kg/m^2.

Figure 2.2 shows the geomagnetic activity index Ap (left) and solar radio flux $F_{10.7}$ (right) for the period in consideration.

Two major orbit maneuvers were performed for CHAMP in 2002, which resulted in an increase of altitude of several kilometers, cf. the black curve in the top panel of Figure 2.3, which presents the observed CHAMP altitude. We accounted for these two orbit maneuvers by increasing the semi-major axis a_{sma} of our prediction by 12.5 km on June 11, 2002, and by 14.5 km on December 10, 2002.

Since the exact value of the ballistic parameter B are not known, we performed the calculations for different values of B. A value of $B = 230$ kg/m^2 (blue line) gave the best agreement with observations (black line). The difference between observed and simulated altitude for that values of B is shown in left panel of Figure 2.4; the right panel shows the difference between simulated and observed Local Time.

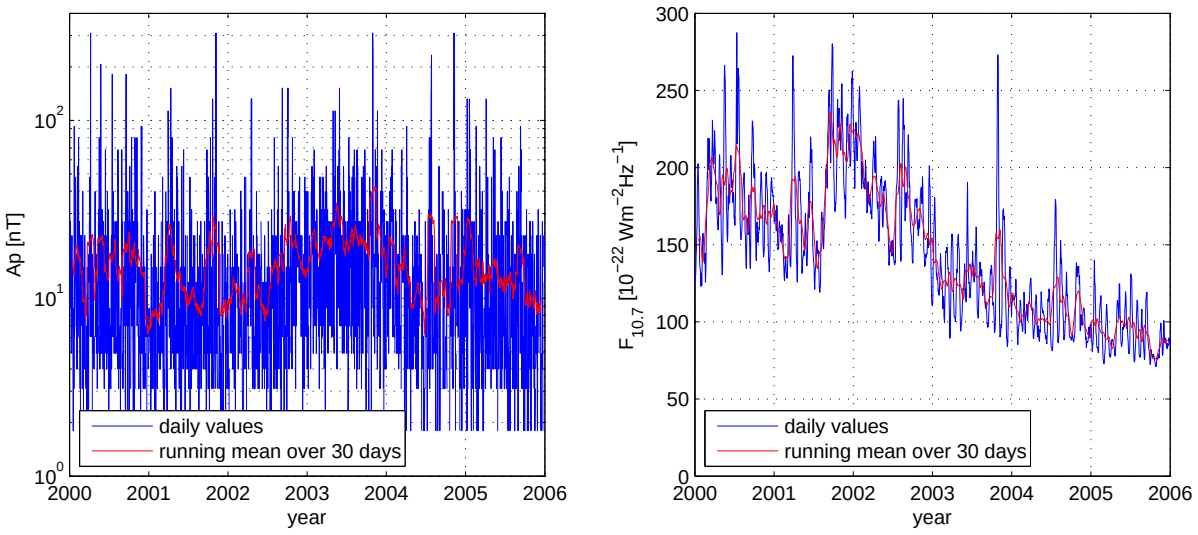

Figure 2.2: Left: Geomagnetic activity index Ap. Right: Solar Radio Flux $F_{10.7}$.

The difference between daily mean values of the simulated and observed CHAMP altitude is less then 3 km, and the difference in Local Time is below 3 min. From these numbers we conclude that our approach is able to predict the main characteristics of a *Swarm*-like satellite orbit.

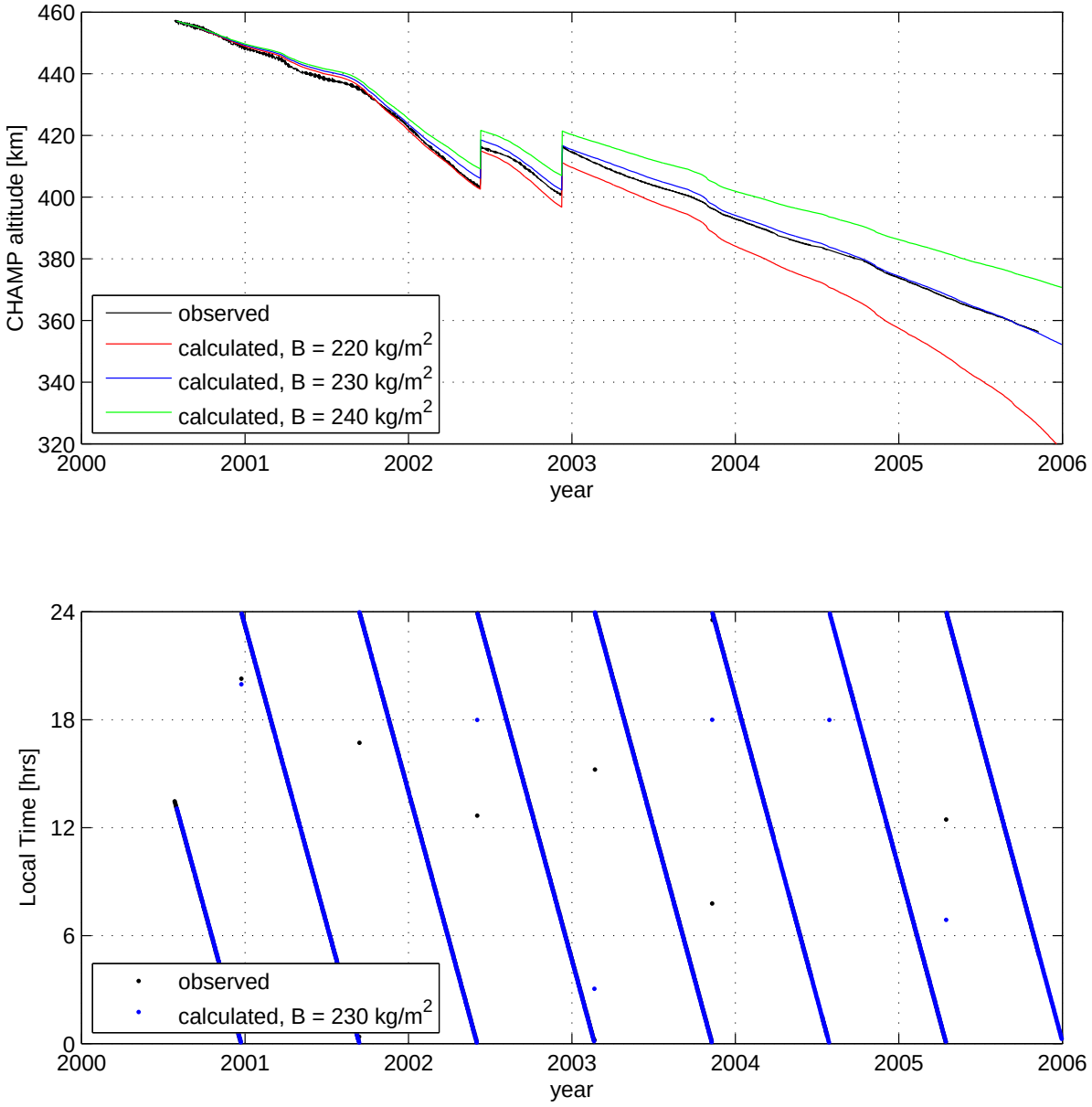

Figure 2.3: Top: observed (black) and simulated orbit decay (daily means) for the CHAMP satellite. Bottom: Observed and simulated Local Time development for CHAMP.

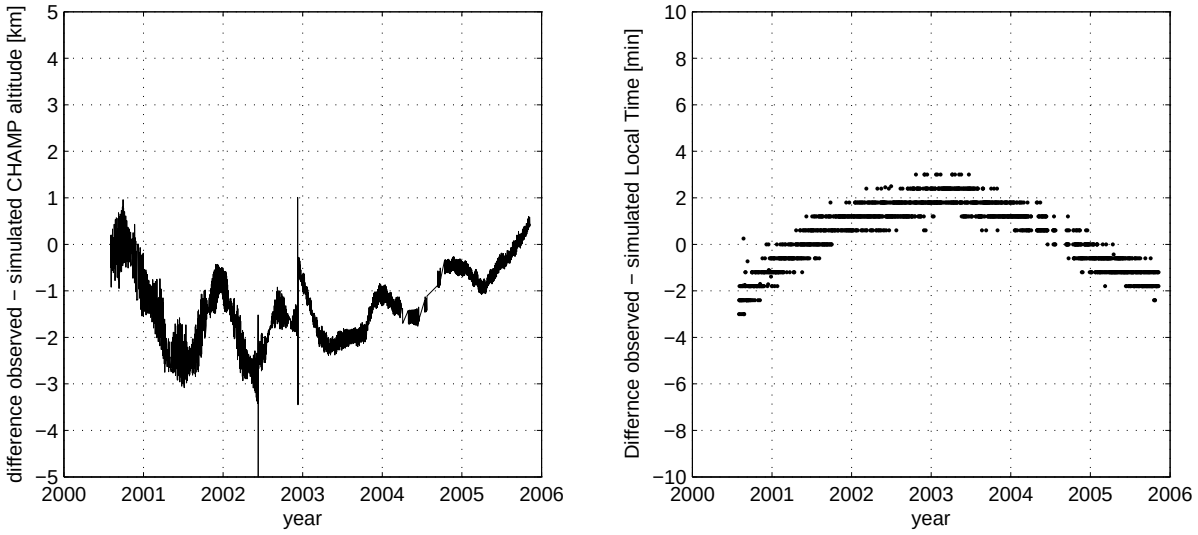

Figure 2.4: Left: Difference between observed and simulated daily means of CHAMP altitude (for $B = 230$ kg/m^2). Right: Difference between observed and simulated CHAMP Local Time (for $B = 230$ kg/m^2).

2.3 Constellation # 3

For test purposes, we have generated synthetic orbits and data for a constellation – denoted as Constellation #3 (constellation #1 and 2 were the ones analyzed in the E2E mission performance simulation, cf. Olsen et al. [2004]) – that has the following characteristics:

	Prerequisites
Epoch for simulations	1997.0 (Launch expected in 2008.0)
Reference radius for altitudes	$a = 6371.2$ km
Earth gravitational constant	$\mu = 3.986004418 \cdot 10^{14}$ m^{3}s^{-2} (IERS Conventions 2003)
Drag coefficients	$C_D = 2.2$
Cross-section area	A = 0.82 m^{-2} (0.75 m^{-2} + 10% margin)
Satellite mass	m = 400 kg
	Low Satellites
Swarm **A**	
Inclination	$i = 86.8°$
RAAN	$\Omega = 0°$
Eccentricity	$\epsilon = 0$
Argument of Perigee	$\omega = 0°$
Mean Anomaly at Epoch	$M = 0°$
Mean Altitude	$h =\sim 450$ km
Semi-Major Axis	$a_{\mathrm{sma}} = 6821.2$ km
Swarm **B**	
Inclination	$i = 86.8°$
RAAN	$\Omega = 358.5°(= -1.5°)$
Eccentricity	$\epsilon = 0$
Argument of Perigee	$\omega = 0°$
Mean Anomaly at Epoch	$M = 0°$
Mean Altitude	$h =\sim 450$ km
Semi-Major Axis	$a_{\mathrm{sma}} = 6821.2$ km
	High Satellite
Swarm **C**	
Inclination	$i = 87.3°$
RAAN	$\Omega = 0°$
Eccentricity	$\epsilon = 0$
Argument of Perigee	$\omega = 0°$
Mean Anomaly at Epoch	$M = 90°$
Mean Altitude	$h =\sim 530$ km
Semi-Major Axis	$a_{\mathrm{sma}} = 6901.2$ km

Table 2.1: Kepler elements used for Constellation #3, for epoch January 1, 1997, 00:00 UT (launch).

Since this constellation was only used for test purposes, it will not be considered further.

2.4 Constellation # 4

We have used orbit parameters that cover the following points:

- The orbits of all spacecraft shall be circular and near-polar.
- Two satellites (*Swarm A and B*) shall fly at 450 km initial altitude, and separated in longitude by 1.4°.
- The third satellite (*Swarm C*) shall fly at 530 km initial altitude.
- The two orbital planes shall have slightly different inclinations giving rise to a difference in nodal drift by some 90° in 3 years.

Based on this criteria we designed Constellation #4, which has the following characteristics:

For our simulation we assumed a launch of the *Swarm* satellites on July 1, 1998, 00:00 UT, i.e. approximately one solar cycle (11 years) before the anticipated launch in 2010. Start of the simulation one solar cycle before the anticipated launch was done in order to have similar ambient conditions, but have access to actual input values to parameterize e.g. the atmospheric drag model, the Earth rotation variations, etc. And start in July 1998 (rather than January 1999, which would have been exactly 11 years before the anticipated launch in 2010) was done since this terminate the simulated mission before January 2003. This is necessary in order to use the rather sophisticated model of magnetospheric contributions that we developed during Phase A and which is only valid between 1997.0 and 2003.0

Observed and predicted solar flux and geomagnetic activity for the years 1980 - 2015 are shown in Figure 2.5. Note that geomagnetic activity lags solar activity, especially concerning the activity minima.

Due to increasing solar activity, a launch later than July 1998 would require more attitude maintenance in order to guarantee a 4.5 year mission lifetime (assuming a 6 months commissioning phase followed by 4 years of science phase). This is illustrated in Figure 2.6 which shows orbit decay as a function of mission lifetime, for several launch dates and orbit maintenance scenarii.

In order to get a mission of 4.5 years duration in combination with a launch in July 1998, we included four orbit maneuvers for the lower pair: we increased the altitude of *Swarm A* and *B* by 15 km on April 1, 2001 and September 1, 2001, respectively, and by 12 km on November 15, 2001 and April 1, 2002, respectively. The obtained altitude is shown by the blue curve in the left panel of Figure 2.6.

Obtained Local Time, Local Time difference between the upper satellite and the lower pair, and satellite altitude as a function of time is shown in Figure 2.7.

The orbits of *Swarm B* were calculated from those of *Swarm A* in the following way:

- Shift of longitude by 1.4°
- Shift of time stamp by Δt, where Δt increases linearly from 2 secs to 10 secs within 60 days, followed by a re-set to the initial value of 2 secs (saw-tooth function). This simulates the requirement that "The maximum time difference between Swarm A and Swarm B when crossing the equator shall be 10 seconds".

	Prerequisites
Epoch for simulations	1998.5 (Launch expected in 2010)
Reference radius for altitudes	$a = 6371.2$ km
Earth gravitational constant	$\mu = 3.986004418 \cdot 10^{14}$ m^{3}s^{-2} (IERS Conventions 2003)
Ballistic coefficients	$B = 230$ kg/m^2
	Low Satellites
Swarm **A**	
Inclination	$i = 87.4°$
RAAN	$\Omega = 0°$
Eccentricity	$\epsilon = 0$
Argument of Perigee	$\omega = 0°$
Mean Anomaly at Epoch	$M = 0°$
Mean Altitude	$h =\sim 450$ km
Semi-Major Axis	$a_{\text{sma}} = 6821.2$ km
Swarm **B**	
Inclination	$i = 87.4°$
RAAN	$\Omega = 358.6°(= -1.4°)$
Eccentricity	$\epsilon = 0$
Argument of Perigee	$\omega = 0°$
Mean Anomaly at Epoch	$M = 0°$
Mean Altitude	$h =\sim 450$ km
Semi-Major Axis	$a_{\text{sma}} = 6821.2$ km
	High Satellite
Swarm **C**	
Inclination	$i = 88.0°$
RAAN	$\Omega = 0°$
Eccentricity	$\epsilon = 0$
Argument of Perigee	$\omega = 0°$
Mean Anomaly at Epoch	$M = 90°$
Mean Altitude	$h =\sim 530$ km
Semi-Major Axis	$a_{\text{sma}} = 6901.2$ km

Table 2.2: Kepler elements used for Constellation #4, for epoch July 1, 1998, 00:00 UT (launch).

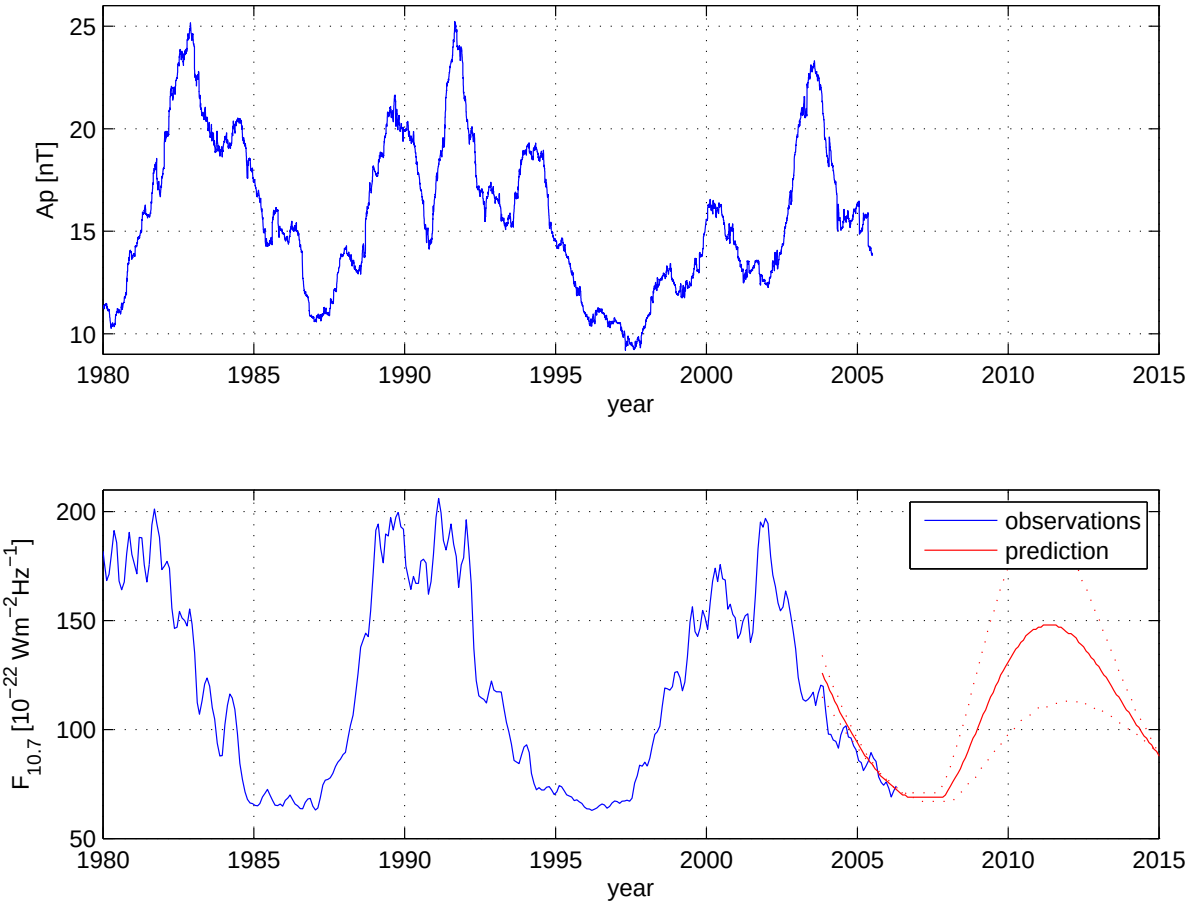

Figure 2.5: Geomagnetic (top) and solar (bottom) activity. Observations are shown in blue, predictions (by K. Schatten) in red.

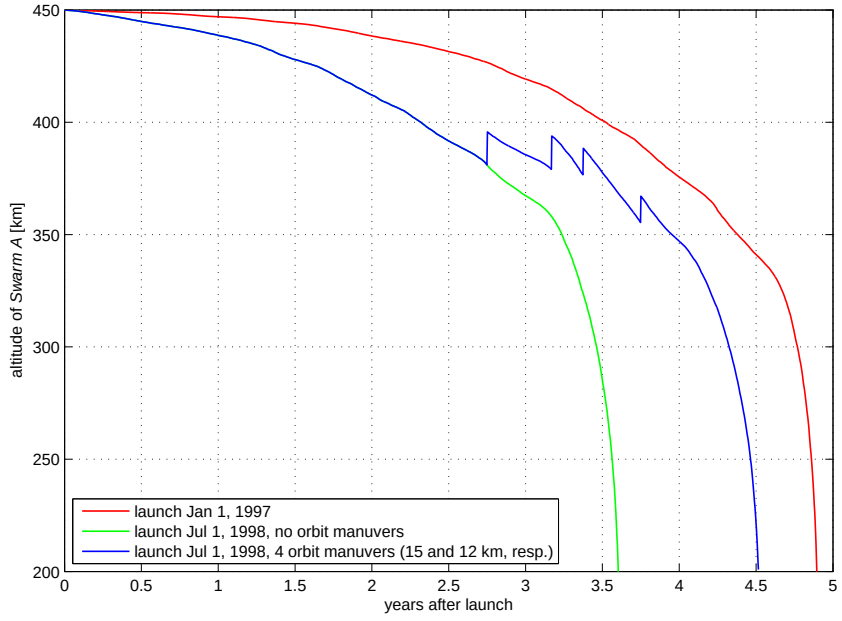

Figure 2.6: Orbit decay for *Swarm A*, for various launch times.

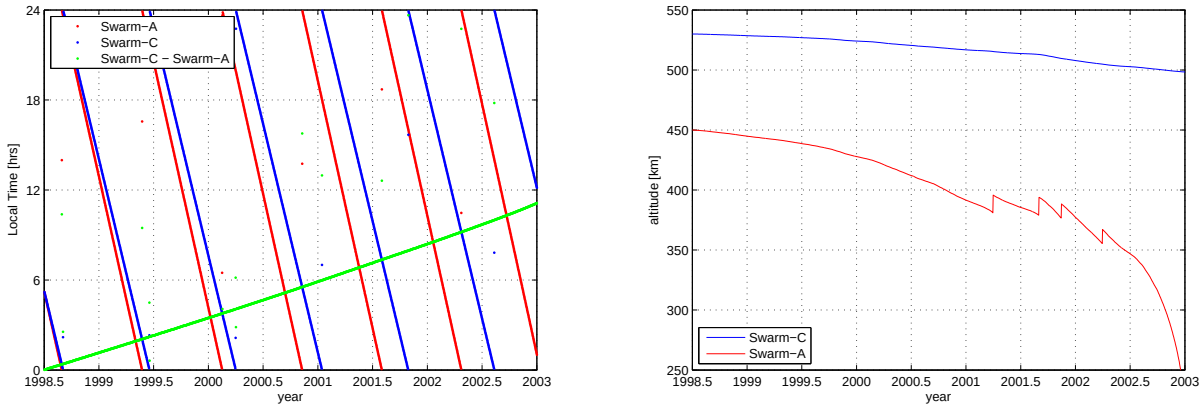

Figure 2.7: Left: Local Time, Local Time difference between the upper satellite and the lower pair, for constellation # 4. Right: obtained altitude.

2.5 Magnetic Field Generation

Magnetic field generation follows mainly the approach used during Phase A of the mission [Olsen et al., 2004, section 3.5]. However, since the toroidal synthetic data generated in Phase A were found to be unrealistic (due to the extrapolation from the Ørsted altitude between 650 and 850 km down to *Swarm* altitudes of 450 km an lower) and thus not included in the Phase A field recovery, we now generated toroidal magnetic fields assuming a fixed altitude of 750 km (i.e. the mean Ørsted altitude). This implies that the in-situ ionospheric currents that are responsible for the toroidal magnetic field do not change with altitude.

Data availability

Data of Constellation #4 are available as daily files with 15 secs sampling rate at ftp.spacecenter.dk/data/magnetic-satellites/Swarm/E2Eplus/constellation_4/. The data are provided as text files (gzipped); The filename follows the naming scheme `swarm4_4_991201.txt.gz` which means data of satellite swarm4, Constellation #4, and for December 1, 1999.

Chapter 3

Impact of the sampling rate: a re-analysis of Phase A data

This section discusses the impact of the sampling rate on the quality of the high-degree lithospheric field recovery. Involved in this task are the working packages WP-3100 "Mission Performance Analysis", and WP-3200 "Mission Performance Analysis, Support".

Recall from the Phase A Task 2 and 3 crustal field recoveries that CI performed well for $n < 90$, but that the results of *Maus et al.* were superior for $n \geq 90$. The high degree recovery in CI was hampered by a peculiar contamination that was manifested as a "hemispherical" degradation pattern in the sensitivitly matrix centered on $m = 0$ with roughly $n > 84$ shown in Fig. 3.1 along with that of *Maus et al.*. It was unclear as to whether the feature was due to

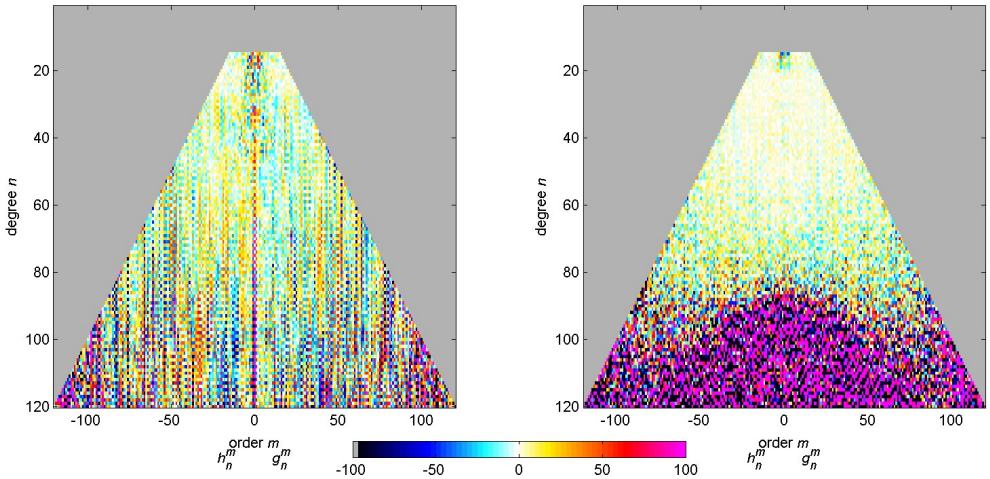

Figure 3.1: Sensitivity matrices for the lithospheric field recovery of two different methods. Left: Gradient approach by *Maus et al.*, cf. section 6.2.8 of the Final E2E Report. Right: Three satellite Comprehensive Inversion result by *Sabaka et al.*, cf. section 6.1.7 of the Final E2E Report.

contamination from a particular magnetic source or perhaps a deficiency in data distribution. Therefore, a series of three test cases were performed over the last year of the mission: only the crustal source was included in the data and parameterized in the model; the magnetospheric field and its parameterization were added; and then finally the field induced by the magnetosphere and its parameterization were added. The results show near perfect recovery when only crust is considered, but the same degradation pattern when adding the magnetosphere and then the induced field. These results indicate that a portion of the time-varying, non-crustal field is being fit by crustal field parameters corresponding consistently to $n > 84$.

Consider that the sampling rate of constellation #1 data is once per minute with an angular speed of the low satellites at approximately $3.84° - 4.03°$/min. This means that Fourier circular functions having wavenumbers above about $k = 88$ are free to oscillate about a low satellite orbit, which overlaps the transition from $n = 85 - 90$ to the degraded regime. In terms of surface spherical harmonics, let this orbit plane coincide with the equatorial plane of a spherical coordinate system, i.e., the plane $\theta = \pi/2$. In this system the harmonics of order $m > 88$ would be free to oscillate between the sampling nodes. If the orbit plane is now rotated by its inclination angle into the usual geographic system, then the pattern of freely oscillating coefficients would change, but the degree bounds of affected coefficients would remain $n > 88$ since surface spherical harmonics of degree n are an irreducible representation of the rotation group. To illustrate this, spherical harmonic coefficients of $m > 88$ were set to unity, otherwise

zero. The coefficient table is shown in the left panel of Fig. 3.2. These coefficients were then

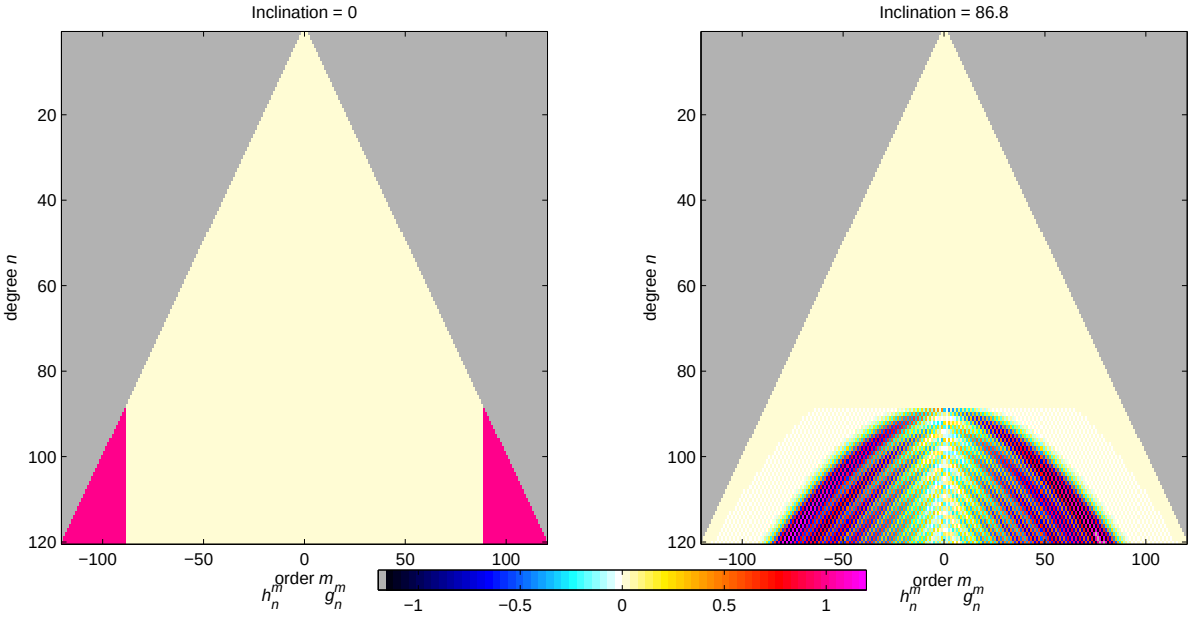

Figure 3.2: Coefficient tables with respect to two different coordinate systems. Left: Coefficients of unity for $m > 88$, otherwise zero, in a reference coordinate system. Right: Same coefficients, but in a system which has been rotated by 86.8° about the cartesian Y axis.

rotated by the low satellite inclination angle of 86.8° about the geographic cartesian Y axis, and the resulting pattern is shown in the right panel of the same figure. This rotation has dramatically changed the pattern such that it looks very similar to the degradation pattern seen in the sensitivity matrix for CI in Fig. 3.1. Although the minimum n of the CI crustal sensitivity matrix is a bit lower ($n = 86$), this strongly suggests that the degradation patterns seen in Phase A Task 2 and 3 may be related to some type of along-track undersampling due to the one minute sampling rate.

The previous discussion is based upon the sampling along a single orbit, but the task results are a function of the total orbit coverage from all satellites over the mission. Previous "crustal only" results clearly show that over time there is sufficient densification of sampling points such that the crustal harmonics are very well determined. Experiments by Sabaka and Olsen [2006] show that the same degradation pattern emerges when dealing with synthetic crustal and magnetospheric signals through either co-estimation or serial estimation. This means that non-crustal signal not fit by non-crustal parameters, on average over the sphere, must alias into the static crustal parameters, if the hypothesis is true. To this end, Task 3 was redone using a 30 sec sampling period so that the corresponding Nyquist wavenumber is about $n = 170$. The results show a dramatic improvement in crustal field recovery, which was synthesized and modelled to $n = 120$, well below the Nyquist wavenumber. The task was further redone using the $n = 150$ crustal model described in the Final E2E Report using both 30 sec and 15 sec sampling periods. The deviation R_n, coefficient difference, and degree correlation plots are shown in Fig. 3.3 for these two cases and the *Maus et al.* case, the best to date. Clearly the increased along-track sampling rate has made an enormous improvement, even from a 30 to 15 sec period, and has allowed for a satisfactory recovery of crustal field coefficients through the entire $n = 150$ spectrum and not just to $n = 140$ as in *Maus et al.*. Further information is

provided by sensitivity matrices in Fig. 3.4 where faint spikes are seen near $m = 0$ and $m = \pm 32$ above about $n = 65$ for the CI recoveries, but whose elements are generally much nearer zero than in the *Maus et al.* case.

To understand such a marked improvement, consider that both the induced and magnetospheric fields are linearly interpolated in time between static expansions centered on the hour. This means that it is highly likely that any two consecutive samples at one minute or shorter periods will be highly positively correlated, and so also the portions of their signal not described by the non-crustal model, which could easily be as significant as the true crustal signal above the Nyquist wavenumber. However, samples taken over the same geographical position but at much

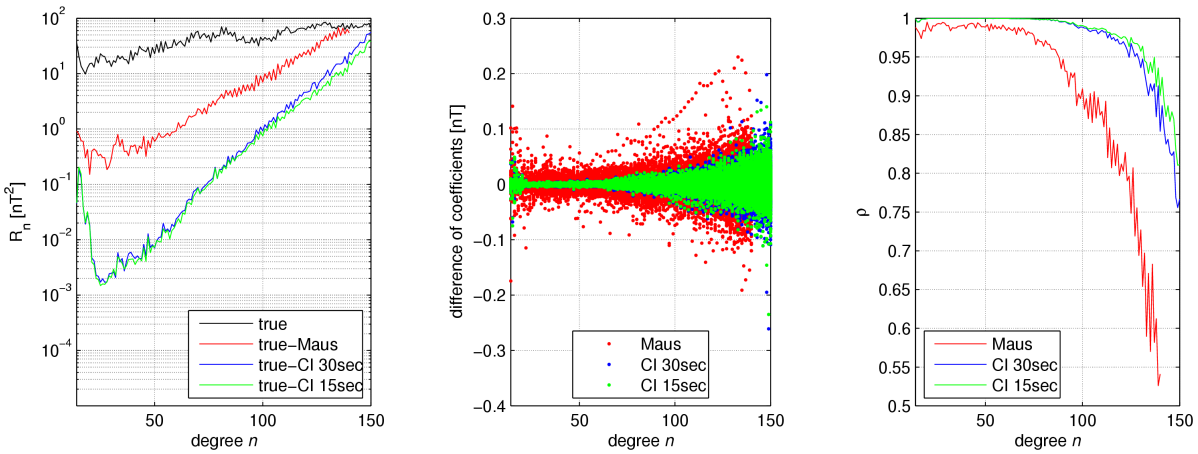

Figure 3.3: Left: R_n spectra of the true (black) crustal field for $n > 13$ and those of its difference with the *Maus et al.* (red), CI 30 sec (blue), and 15 sec (green) sampling period models. Middle: Coefficient differences of the various models (same color scheme) with respect to the true model. Right: Degree correlation of the various models (same color scheme) with respect to the true model.

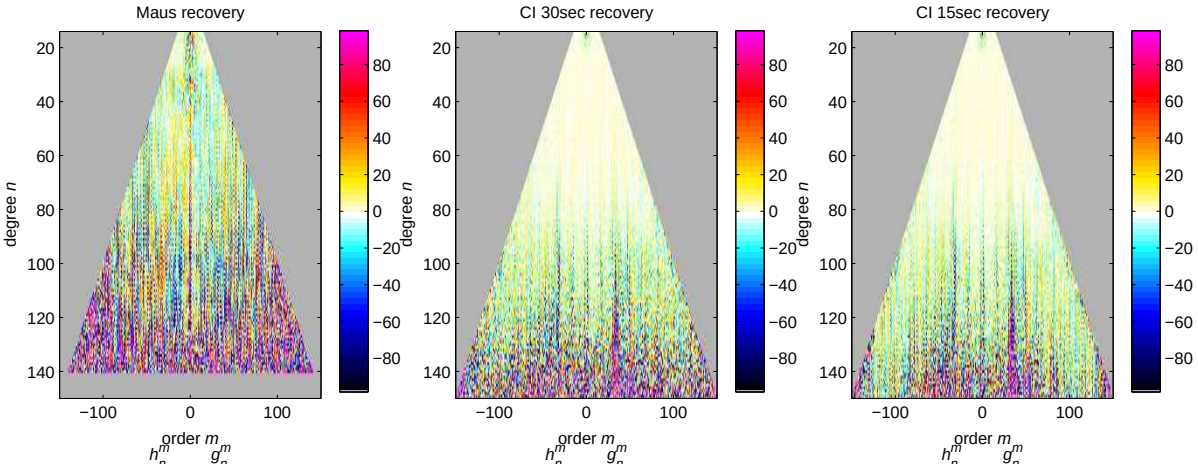

Figure 3.4: Sensitivity matrices for the lithospheric field recovery of two different methods. Left: Gradient approach by *Maus et al.*, cf. section 6.2.8 of the Final E2E Report. Middle: Three satellite Comprehensive Inversion result using a 30 sec sampling period. Right: Same as middle, but with a 15 sec sampling period.

different times will likely not be highly correlated in these remaining signals. Therefore, the leakage of non-crustal signal into crustal parameters is likely driven by consecutive, temporally correlated samples. If these signals are large enough, then the reduction of the least-squares cost function will be worth the crustal field fitting these signals with coefficients above the Nyquist wavenumber. Now if samples are taken every 30 seconds, then there will be a point midway between the original one minute samples. If this point has remaining non-crustal signal which is not positively correlated with that of the two adjacent samples, e.g., it is strongly negative while the adjacent signals are strongly positive, then there is a chance that these three signals can be fit by crustal parameters above the original Nyquist wavenumber. However, if the signal is positively correlated, e.g., all signals are strongly positive or negative, then their fitting will be prohibited since the crustal harmonics above the Nyquist wavenumber must oscillate about the zero level between the one minute samples. That is, a good fit to the one minute samples will result in a large misfit to the 30 sec sample midway between and perhaps an increase in the cost function. It is expected that 30 sec samples will indeed be strongly positively correlated, and so this is thought to be the reason for the large reduction in non-crustal leakage into the crustal spectrum above the Nyquist wavenumber. Note that by this argument the 15 sec period would not be expected to have much advantage over the 30 sec case, and this is corroborated in Figs. 3.3 and 3.4.

In summary, undersampling of the time varying non-crustal field along track, with respect to the crustal field harmonics, can result in aliasing of prominent portions of this field into crustal field parameters. A higher sampling rate can reduce this aliasing, but this probably depends upon the nature of the remaining non-crustal field; if it is not strongly positively correlated from point to point, then this problem may remain. In general, non-crustal models of higher resolution, when supported by adequate data coverage, are the key to mitigating this problem.

Chapter 4

Improved Lithospheric Field Recovery Using Magnetic Field Differences

This chapter describes the development, test and implementation of an approach to utilize the magnetic field difference ("gradient") of the lower *Swarm* satellite pair. Involved in this task are the working packages WP-2110 "Difference Approach: Algorithm Development", and WP-2120 "Difference Approach: CI Implementation".

Perhaps one of the most innovative features of the *Swarm* mission is the east-west pairing of the lower satellites whose near-polar orbit planes are separated by 1.5°. A simple differencing of the data will result in an enhancement of their potential field signal as a function of spherical harmonic order m. Advantage may be taken of this enhancement to resolve crustal structure much smaller than possible by an analysis of the usual field components at the same altitude. These ideal gain factors are shown in Fig. 4.1 for longitudinal separations of $\Delta\phi = 1°$, 1.5°, and 2°.

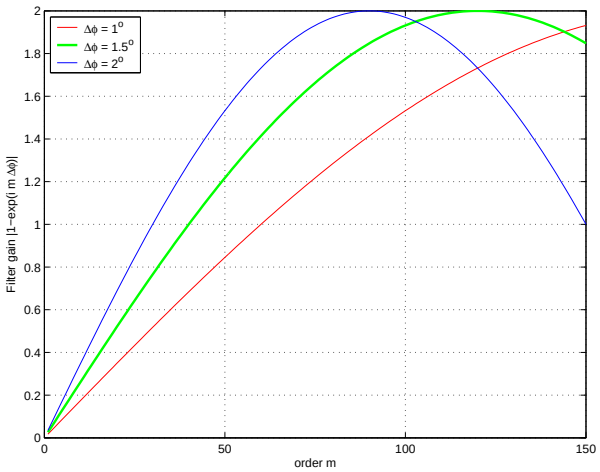

Figure 4.1: Gain factor for order m from data differences at longitude differences of $\Delta\phi = 1°$, 1.5°, and 2°.

A sequential analysis may be undertaken in which non-crustal fields are first removed from either the field components or directly from the difference or gradient data. These data are then fit with a crustal field. However, these types of sequential estimations have been shown to be sub-optimal in their separation of signals from the various sources [Sabaka and Olsen, 2006]. The CI approach attempts to parameterize and estimate all major sources simultaneously to avoid these separation problems. The following section will introduce a methodology in which the sensitivity of the gradient data to small-scale crustal structure is exploited while non-crustal parameters are determined by the whole data set all within the CI framework.

4.1 Selective Infinite-Variance Weighting

The key to this approach is producing and/or identifying data subsets that are particularly sensitive to certain parameter subsets and applying appropriate weighting such that these data strongly influence the determination of such parameters. The weighting employed here will be termed "selective infinite-variance weighting" (SIVW) for reasons now to be discussed. Consider the following simple linear model where the data vector $\mathbf{d}$ is related to the model parameter vector $\mathbf{x}$ through a linear operator A

$$\mathbf{d} = A\mathbf{x} + \nu, \tag{4.1}$$

$$= A\mathbf{x} + B\mathbf{y} + \mathbf{e}, \tag{4.2}$$

where ν is the noise vector having both a random part, $\mathbf{e}$ and a systematic part $B\mathbf{y}$. Here B is a linear operator and $\mathbf{y}$ is the underlying state. Let $\mathbf{e}$ and $\mathbf{y}$ be uncorrelated and normally distributed such that $\mathbf{e} = N(\mathbf{0}, C)$ and $\mathbf{y} = N(\mu, Q)$. Therefore, ν is normally distributed such that $\nu = N(B\mu, C + BQB^T)$. Given that least-squares is the estimator of choice, a critical restriction is then imposed on the treatment of the noise vector, i.e., that which is accounted for in the data covariance matrix W^{-1}, which is its expected value is to be zero. This is equivalent to choosing finite C and Q covariance matrices such that

$$\begin{aligned} W &= (C + BQB^T)^{-1}, && (4.3)\\ &= C^{-1} - C^{-1}B(Q^{-1} + B^TC^{-1}B)^{-1}B^TC^{-1}. && (4.4) \end{aligned}$$

The corresponding least-squares solution $\tilde{\mathbf{x}}$ is then given by

$$\begin{aligned} \tilde{\mathbf{x}} &= (A^TWA)^{-1}A^TWd, && (4.5)\\ &= (A^TWA)^{-1}A^TW(A\mathbf{x} + B\mathbf{y} + \mathbf{e}), && (4.6)\\ &= \mathbf{x} + (A^TWA)^{-1}A^TW(B\mathbf{y} + \mathbf{e}), && (4.7) \end{aligned}$$

with expected value

$$E[\tilde{\mathbf{x}}] = \mathbf{x} + (A^TWA)^{-1}A^TWB\mu. \quad (4.8)$$

If $E[\nu] = \mu = \mathbf{0}$, in accordance with least-squares, then the solution is unbiased, otherwise not. This violation in the assumption of zero expected value of the noise occurs frequently in geomagnetic field modelling, usually in the context of unparameterized natural field sources. Because they are accounted for solely through W^{-1} by attempting to assign a finite variance, they are necessarily assumed to be zero-mean by the restrictions imposed by least-squares. Note that even if a natural field is a zero-mean process over some characteristic time interval, it most certainly does not have a zero-valued realization at the time a measurement was taken.

Aside from the restriction of zero-mean noise processes, one is free to choose the variance, σ^2, of the process in the least-squares weighting. Recall that as σ^2 increases, the distribution curve remains centered on zero, but becomes flatter. In fact, for finite σ^2, the distribution is always centered on zero. However, for infinite variances the central tendency, and thus, the mean of the distribution becomes undefined. This is a very useful result in that it allows for undefined (non-zero) means within the restrictive framework of least-squares. Now let $Q = \sigma^2\tilde{Q}$ and let $\sigma^2 \to \infty$ in eq. 4.4 such that

$$\begin{aligned} W_\infty &\equiv \lim_{\sigma^2\to\infty} W, && (4.9)\\ &= \lim_{\sigma^{-2}\to 0} C^{-1} - C^{-1}B(\sigma^{-2}\tilde{Q}^{-1} + B^TC^{-1}B)^{-1}B^TC^{-1}, && (4.10)\\ &= C^{-1} - C^{-1}B(B^TC^{-1}B)^{-1}B^TC^{-1}. && (4.11) \end{aligned}$$

The corresponding least-squares solution is now given by

$$\begin{aligned} \tilde{\mathbf{x}} &= (A^TW_\infty A)^{-1}A^TW_\infty d, && (4.12)\\ &= (A^TW_\infty A)^{-1}A^TW_\infty(A\mathbf{x} + B\mathbf{y} + \mathbf{e}), && (4.13)\\ &= \mathbf{x} + (A^TW_\infty A)^{-1}A^TW_\infty\mathbf{e}. && (4.14) \end{aligned}$$

The term in B in eq. 4.13 has dropped out of eq. 4.14 because

$$\begin{aligned} W_\infty B &= (C^{-1} - C^{-1}B(B^TC^{-1}B)^{-1}B^TC^{-1})B, && (4.15)\\ &= C^{-1}B - C^{-1}B(B^TC^{-1}B)^{-1}B^TC^{-1}B, && (4.16)\\ &= C^{-1}B - C^{-1}B, && (4.17)\\ &= 0. && (4.18) \end{aligned}$$

In fact, if eq. 4.1 is prewhitened such that $C = I$, then $W_\infty = \mathcal{N}_B$, where $\mathcal{N}_B$ is the projection matrix onto the nullspace of the column span of B. Thus, W_∞ imposes a harder bound on $\tilde{\mathbf{x}}$ than does W such that all signal that can be represented by $B\mathbf{y}$ is eliminated from the estimation. This can be seen from

$$E[\tilde{\mathbf{x}}] = \mathbf{x}, \tag{4.19}$$

and so the solution is always unbiased independent of the state of $\mathbf{y}$. Sabaka and Olsen [2006] have shown that the solution given in eq. 4.12 is equivalent to the solution one gets when least-squares co-estimating $\mathbf{y}$ with $\mathbf{x}$ in eq. 4.2. Thus, one finds that co-estimating $\mathbf{y}$ with $\mathbf{x}$ is equivalent to treating $\mathbf{y}$ as a normally distributed infinite-variance process requiring infinite-variance weighting.

One can now begin to see the mechanism by which infinite-variance weighting may be used to selectively minimized the influence of certain data subsets on certain parameter subsets. Define two data subsets, $\mathbf{d}_1$ and $\mathbf{d}_2$, which are linear functions of two parameter subsets of interest, $\mathbf{x}$ and $\mathbf{y}$, associated with linear operators A and B, respectively. Let the corresponding data noise vectors be $\nu_1 = N(\mathbf{0}, I)$ and $\nu_2 = \mathbf{e} + B_2\mathbf{z}$, where $\mathbf{e} = N(\mathbf{0}, I)$ and $\mathbf{z}$ is deterministic and represents a systematic contamination of $\mathbf{y}$ in the $\mathbf{d}_2$ data. In order to account for ν_1, $\mathbf{e}$, and $\mathbf{z}$ the following W is constructed which treats $\mathbf{z}$ as an infinite-variance process

$$W = \begin{pmatrix} I & 0 \\ 0 & I - B_2(B_2^T B_2)^{-1} B_2^T \end{pmatrix} = \begin{pmatrix} I & 0 \\ 0 & \mathcal{N}_{B_2} \end{pmatrix}. \tag{4.20}$$

Since W is idempotent it may be used directly to prewhiten the augmented system equations

$$\begin{pmatrix} \mathbf{d}_1 \\ \mathbf{d}_2 \end{pmatrix} = \begin{pmatrix} A_1 & B_1 \\ A_2 & B_2 \end{pmatrix} \begin{pmatrix} \mathbf{x} \\ \mathbf{y} \end{pmatrix} + \begin{pmatrix} \nu_1 \\ \nu_2 \end{pmatrix}, \tag{4.21}$$

such that

$$\begin{pmatrix} \mathbf{d}_1 \\ \mathcal{N}_{B_2}\mathbf{d}_2 \end{pmatrix} = \begin{pmatrix} A_1 & B_1 \\ \mathcal{N}_{B_2}A_2 & \mathcal{N}_{B_2}B_2 \end{pmatrix} \begin{pmatrix} \mathbf{x} \\ \mathbf{y} \end{pmatrix} + \begin{pmatrix} \nu_1 \\ \mathcal{N}_{B_2}\nu_2 \end{pmatrix}, \tag{4.22}$$

$$= \begin{pmatrix} A_1 & B_1 \\ \mathcal{N}_{B_2}A_2 & 0 \end{pmatrix} \begin{pmatrix} \mathbf{x} \\ \mathbf{y} \end{pmatrix} + \begin{pmatrix} \nu_1 \\ \mathcal{N}_{B_2}\mathbf{e} \end{pmatrix}. \tag{4.23}$$

Note from eq. 4.23 that this W has selectively eliminated the direct influence of $\mathbf{d}_2$ on the determination of $\mathbf{y}$ via the B_2 matrix while allowing all data to continue to influence $\mathbf{x}$. The equivalent system of equations for co-estimation is given by

$$\begin{pmatrix} \mathbf{d}_1 \\ \mathbf{d}_2 \end{pmatrix} = \begin{pmatrix} A_1 & B_1 & 0 \\ A_2 & 0 & B_2 \end{pmatrix} \begin{pmatrix} \mathbf{x} \\ \mathbf{y} \\ \mathbf{n} \end{pmatrix} + \begin{pmatrix} \nu_1 \\ \mathbf{e} \end{pmatrix}, \tag{4.24}$$

where $\mathbf{n} = \mathbf{y} + \mathbf{z}$ are considered "nuisance parameters". From an operational standpoint, solving eq. 4.24 is much preferred to solving eq. 4.23, since the latter requires an explicit formation of the dense matrix $\mathcal{N}_{B_2}$, which has square dimensions of order $\dim \mathbf{d}_2$.

The application of selective infinite-variance weighting to the current problem is now straight forward. Let $\mathbf{d}_1$, $\mathbf{d}_2$, and $\mathbf{d}_3$ be the data from *Swarm* low satellites 1 and 2 and high satellite 3. Assume that $\dim \mathbf{d}_1 = \dim \mathbf{d}_2$ and that their elements are chronologically matched. Let $\mathbf{x}$ be the non-crustal parameters related to the data through A and let $\mathbf{y}$ be the crustal field

parameters related through B. Let ν_1, ν_2, and ν_3 be the noise vectors corresponding to the data. Consider the following rotation of the prewhitened system equations

$$\begin{pmatrix} \frac{1}{\sqrt{2}} & \frac{1}{\sqrt{2}} & 0 \\ \frac{1}{\sqrt{2}} & \frac{-1}{\sqrt{2}} & 0 \\ 0 & 0 & 1 \end{pmatrix} \begin{pmatrix} \mathbf{d}_1 \\ \mathbf{d}_2 \\ \mathbf{d}_3 \end{pmatrix} = \begin{pmatrix} \frac{1}{\sqrt{2}} & \frac{1}{\sqrt{2}} & 0 \\ \frac{1}{\sqrt{2}} & \frac{-1}{\sqrt{2}} & 0 \\ 0 & 0 & 1 \end{pmatrix} \left[\begin{pmatrix} A_1 & B_1 \\ A_2 & B_2 \\ A_3 & B_3 \end{pmatrix} \begin{pmatrix} \mathbf{x} \\ \mathbf{y} \end{pmatrix} + \begin{pmatrix} \nu_1 \\ \nu_2 \\ \nu_3 \end{pmatrix} \right] \quad (4.25)$$

$$\begin{pmatrix} \mathbf{d}_s \\ \mathbf{d}_d \\ \mathbf{d}_3 \end{pmatrix} = \begin{pmatrix} A_s & B_s \\ A_d & B_d \\ A_3 & B_3 \end{pmatrix} \begin{pmatrix} \mathbf{x} \\ \mathbf{y} \end{pmatrix} + \begin{pmatrix} \nu_s \\ \nu_d \\ \nu_3 \end{pmatrix}, \quad (4.26)$$

where the subscripted "s" and "d" indicate sums and differences, respectively.

The gain factors in Fig. 4.1 correspond to the difference data only. It turns out that the gain factors for sums of data are complementary to this. That is, if the difference gain for order m is $g_d(m)$, then the corresponding sum gain is $g_s(m) = 2 - g_d(m)$. This suggests that higher order crustal coefficients should be determined by difference data only while the lower order coefficients should be determined by sum data and possibly data from the high satellite. Let the lower order crustal coefficients be designated by $\mathbf{y}_\ell$ and the higher order by $\mathbf{y}_h$ and let them be related to the data through B^ℓ and B^h, respectively. The resulting system equations are given by

$$\begin{pmatrix} \mathbf{d}_s \\ \mathbf{d}_d \\ \mathbf{d}_3 \end{pmatrix} = \begin{pmatrix} A_s & B_s^\ell & 0 & 0 & B_s^h \\ A_d & 0 & B_d^h & B_d^\ell & 0 \\ A_3 & B_3^\ell & 0 & 0 & B_3^h \end{pmatrix} \begin{pmatrix} \mathbf{x} \\ \mathbf{y}_\ell \\ \mathbf{y}_h \\ \mathbf{n}_\ell \\ \mathbf{n}_h \end{pmatrix} + \begin{pmatrix} \mathbf{e}_s \\ \mathbf{e}_d \\ \mathbf{e}_3 \end{pmatrix}, \quad (4.27)$$

where $\mathbf{n}_\ell$ and $\mathbf{n}_h$ are the nuisance parameters in the low and high order crustal coefficient regimes, respectively. These parameters are a combination of true crustal signal and a systematic noise component due to such things as non-crustal signal leakage. Thus, while the $\mathbf{x}$ parameters are influenced directly by all data, the $\mathbf{y}$ parameters are determined by different combinations of data, depending on their sensitivity. Note that if the distinction between $\mathbf{y}$ and $\mathbf{n}$ were not made, then eq. 4.27 would reduce to the original, unrotated system in eq. 4.25. Clearly, this method may be further refined, for example, by distinguishing again between sums, differences, and high satellite data collected on the dayside versus nightside.

4.2 Application to the Gradient problem

The application of SIVW to the gradient problem was carried out on synthesized data from constellation # 3 using a 15 sec sampling interval. Specifically, the difference data were focused on coefficients of order $m > 20$, while all data, including sums and differences, were focused on $m \leq 20$. The change in recovery of low-order coefficients when difference data are focused on them or not is negligible in this case. Therefore, eq. 4.27 now becomes

$$\begin{pmatrix} \mathbf{d}_s \\ \mathbf{d}_d \\ \mathbf{d}_3 \end{pmatrix} = \begin{pmatrix} A_s & B_s^\ell & 0 & B_s^h \\ A_d & B_d^\ell & B_d^h & 0 \\ A_3 & B_3^\ell & 0 & B_3^h \end{pmatrix} \begin{pmatrix} \mathbf{x} \\ \mathbf{y}_\ell \\ \mathbf{y}_h \\ \mathbf{n}_h \end{pmatrix} + \begin{pmatrix} \mathbf{e}_s \\ \mathbf{e}_d \\ \mathbf{e}_3 \end{pmatrix}. \quad (4.28)$$

Fields whose parameters reside in $\mathbf{x}$ include core and associated SV, ionosphere and associated induced, and magnetosphere and associated induced in the form of explicit high-frequency

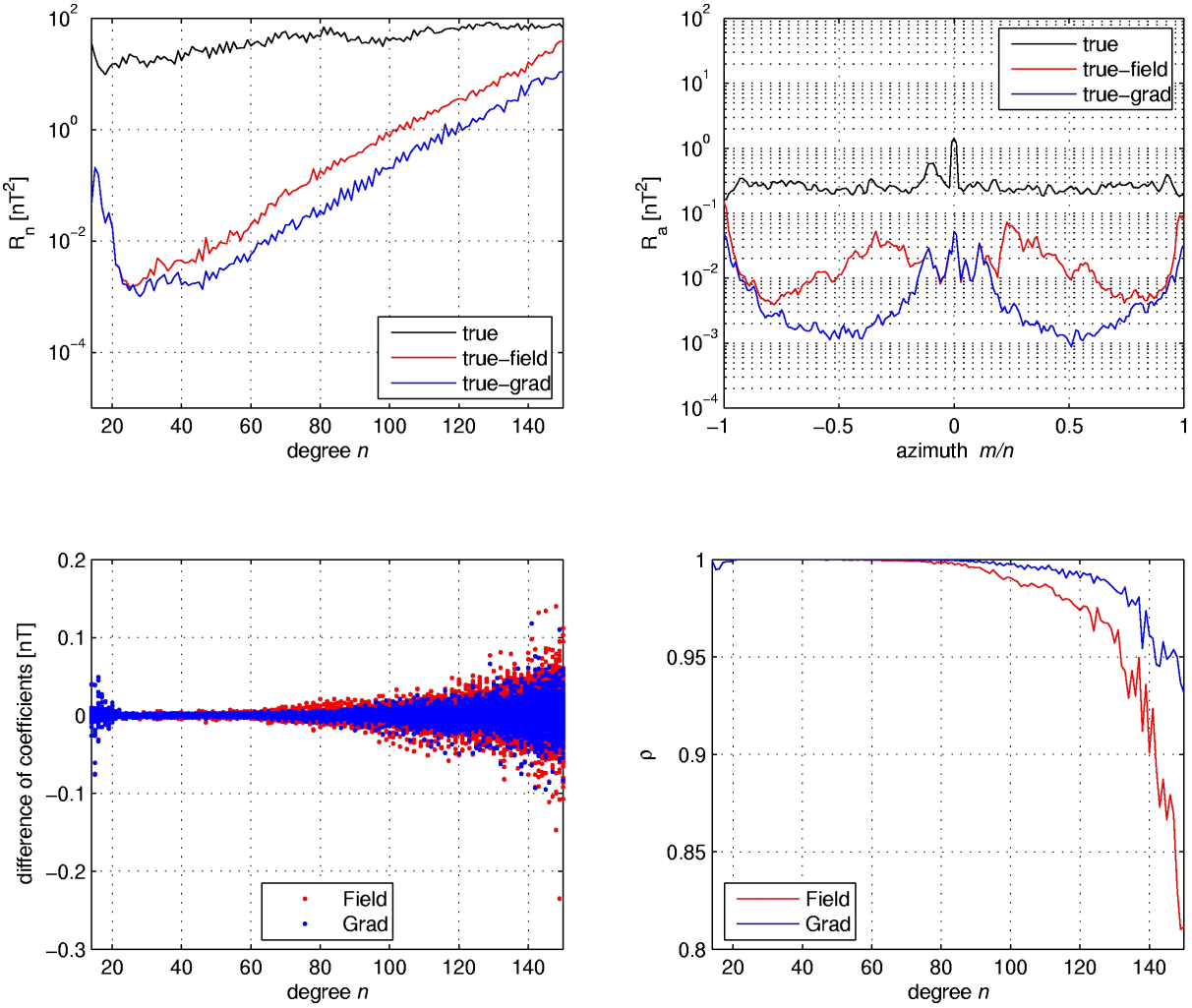

Figure 4.2: Upper-left: R_n spectra of the true (black) crustal field for $n > 13$ and those of its difference with CI applied directly to field values (red) and to low satellite sums and differences and high satellite data (blue). Upper-right: R_a (azimuthal) spectra. Lower-left: Coefficient differences with respect to the true model. Lower-right: Degree correlation with respect to the true model.

internal expansions, and follow the E2E study of Sabaka and Olsen [2006]. The data are prewhitened by the usual equal-area factor, $\sqrt{\sin\theta}$, where θ is the geographic colatitude of the data position.

A comparison of the performance of CI applied directly to the field components measured by the satellites versus a solution to the system in eq. 4.28 is illustrated in Fig. 4.2. The upper-left panel shows the R_n spectra of the former (red), the latter (blue), and the true model (black) and indicates a roughly two-fold reduction in power in the error per degree above about $n = 45$ when difference data are exploited. Looking at the upper-right panel shows an error that is as much as three times less for azimuthal, (m/n), numbers near 0.5, but consistently less when using difference data for $|m/n| > 0.2$. Interestingly, both cases show nearly identical behavior for low azimuthal numbers, which are dominated by low-order m and high-degree n. Recall that this regime ($m \leq 20$) is sensitive to all data, and so this is not unexpected. The lower-left panel shows the coefficient differences between the true and recovered models and confirms that

the SIVW applied to the rotated data system extracts coefficients at least as accurate as the traditional approach, but much more so for high n. The increased spread of the differences for $n \leq 20$ is due to the fact that SV is present and is more of a challenge to resolve than static coefficients. Finally, the lower-right panel indicates a far superior recovery of coefficients with the new method with regards to phase of the models, i.e., degree correlation. The new method is now recovering a field that is positively correlated with the true field at the 0.93 level for $n = 150$, the degree limit of the synthetic signal. Again, note the slight excursion below $n = 20$ due to SV.

A more complete view of the performance of the traditional field value method versus the gradient method can be seen by comparing the sensitivity matrices in Fig. 4.3. The gradient recovery is excellent for mid-valued m, as confirmed by the R_a plots in Fig. 4.2, but is nearly identical to the traditional approach for the $m \leq 20$ regime. There is also some improvement for the purely sectorial terms (left and right edges). All of these results strongly suggest that the *Swarm* constellation is capable of accurately recovering very small-scale lithospheric structure, perhaps even smaller than indicated in these tests. This will go far in closing the gap in intermediate lithospheric wavelength coverage that exists now between satellites and aeromagnetic surveys.

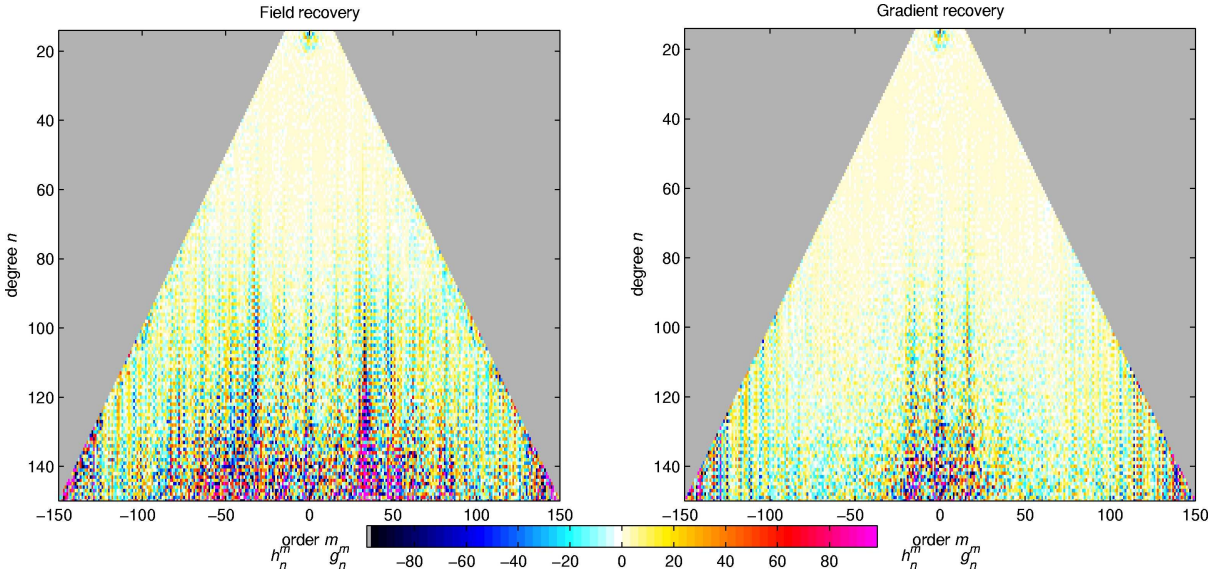

Figure 4.3: Sensitivity matrices for the lithospheric field recovery from CI applied directly to field values (left) and to low satellite sums and differences and high satellite data (right).

It is clear from the previous discussion that SIVW has successfully exploited the difference data from the low satellites to extract high order lithospheric field coefficients without degrading those of low order. Furthermore, Figs. 4.4 and 4.5 show that neither the magnetospheric nor the associated high-frequency induced coefficient recoveries have suffered. Not only do the magnetospheric coefficient time series show good agreement with the true series (blue), but the results from the traditional (red) and gradient approach (green) are identical. Notice, however, that certain recovered coefficients, such as q_1^1, show large excursions from the true model at the beginning of the mission. This has been discussed by Sabaka and Olsen [2006] and is due to the minimal separation in local time of the low and high satellite orbital planes in co-rotation phase, which affects some coefficients. The high-frequency induced coefficients also show exact agreement between the two recovered time series. Again, there are large discrepancies between

certain recovered and true coefficients at the beginning and end of the mission due to minimal orbital plane separation. Indeed, it appears that SIVW applied to sums, differences, and high data to target high-order lithospheric recovery is performing precisely as hoped. That is, it is exploiting the enhanced signal to noise ratio of the high-order lithospheric field in the low satellite difference data to obtain superior recovery of this portion of the field without degrading the recovery of low-order lithospheric and non-lithospheric field parameters.

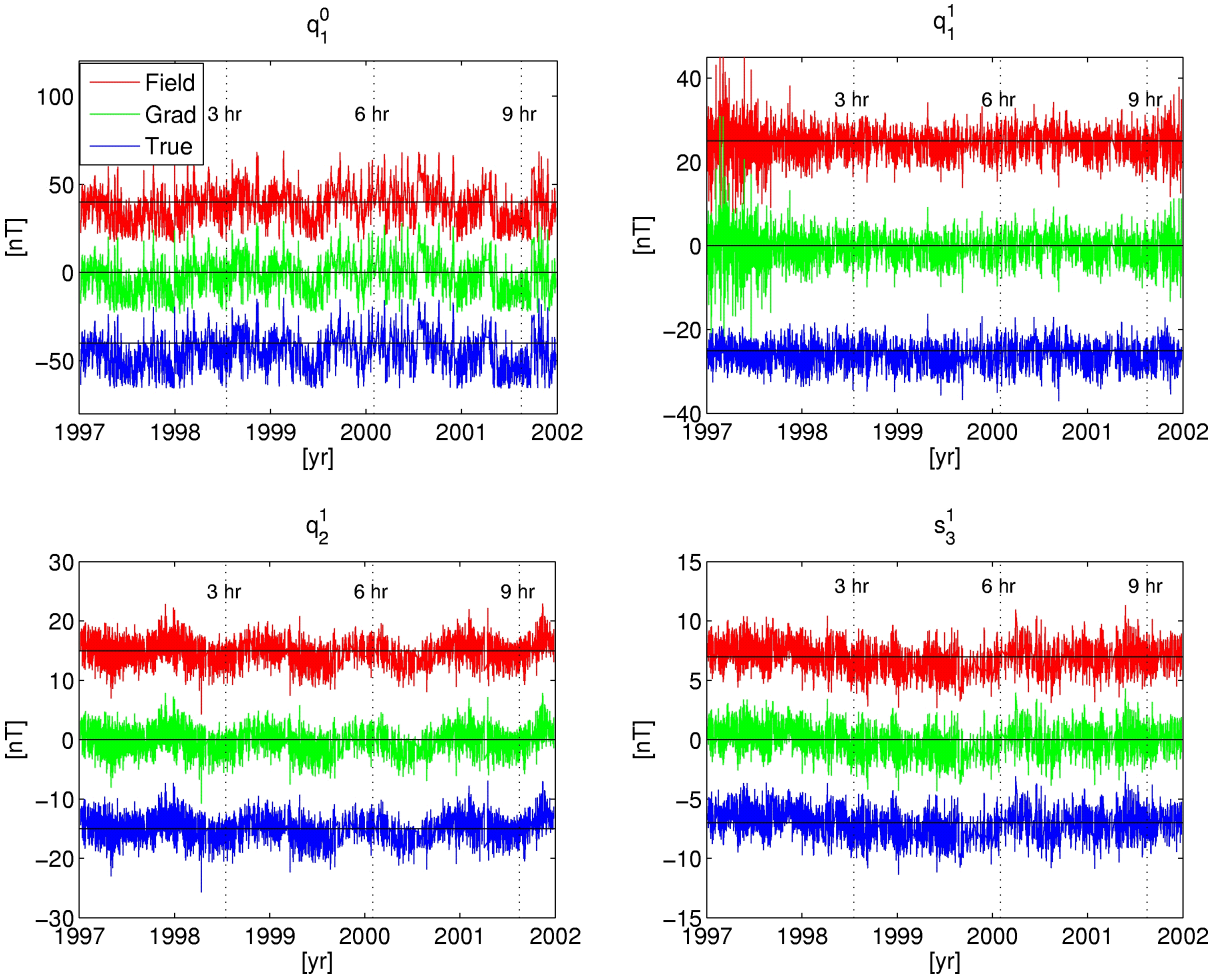

Figure 4.4: Time series of selected magnetospheric coefficients from the true model (blue) and from CI applied directly to field values (red) and to low satellite sums and differences and high satellite data (green). The blue and red lines have been shifted for clarity. Local time differences between the low and high satellite orbital planes are delineated by vertical dotted lines at 3, 6 and 9 hr separation.

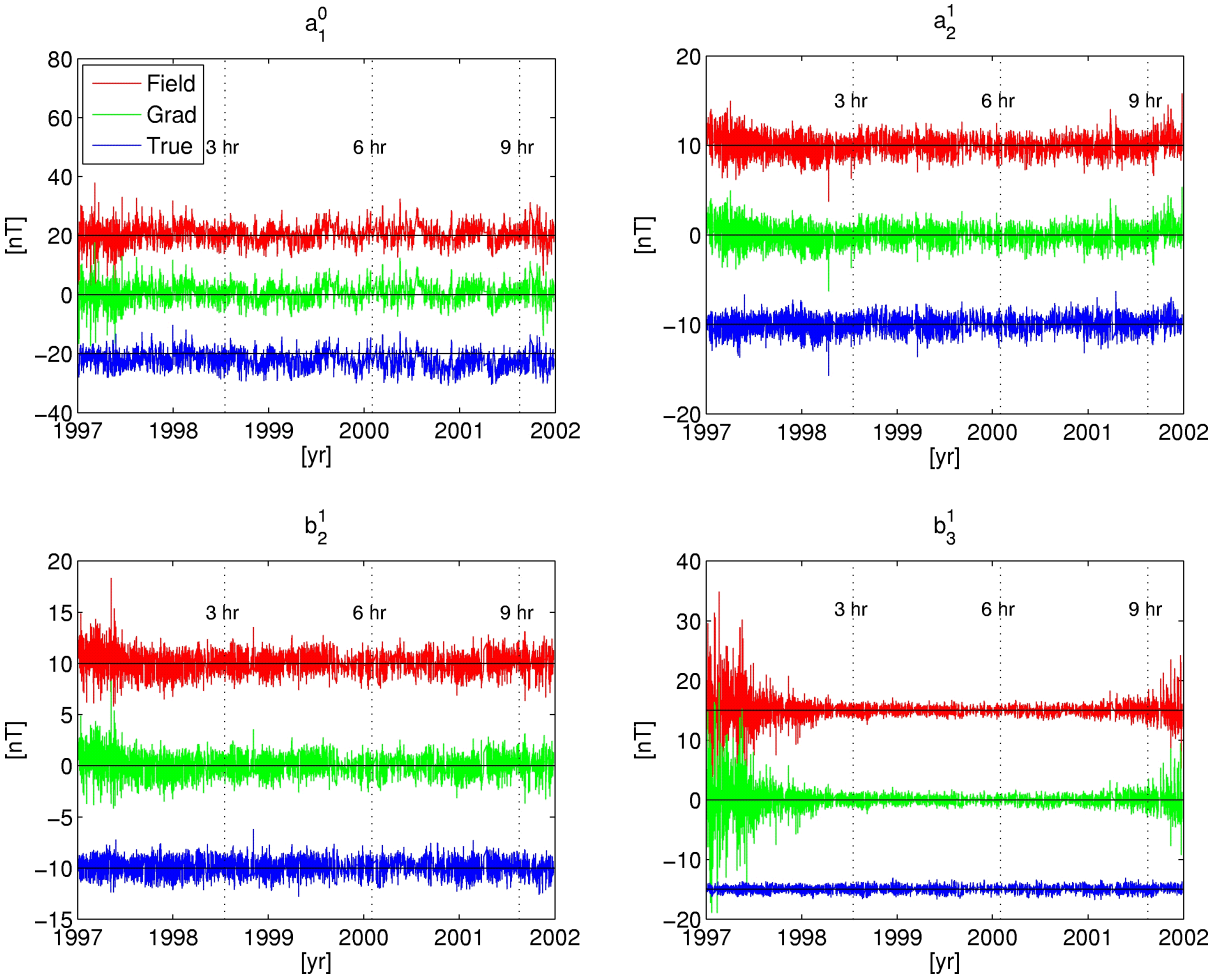

Figure 4.5: Time series of selected high-frequency induced coefficients from the true model (blue) and from CI applied directly to field values (red) and to low satellite sums and differences and high satellite data (green). The blue and red lines have been shifted for clarity. Local time differences between the low and high satellite orbital planes are delineated by vertical dotted lines at 3, 6 and 9 hr separation.

Chapter 5

Multi-Satellite In-Flight VFM/STR Alignment

This section describes the in-flight alignment of the *Swarm* magnetometers, i.e. the determination of the transformation between the coordinate frame of the vector magnetometer (VFM) and that of the star camera (STR). This transformation is described by means of three Euler angles (α, β, γ). Involved in this task are the working packages WP-2210 "Multi-Satellite Alignment: Algorithm Development", and WP-2120 "Multi-Satellite Alignment: CI Implementation". The described activity is an extension of the experiments that have been performed during Phase A [cf. section 4.2 of Olsen et al., 2004].

To obtain the magnetic field in the North-East-Center (NEC) coordinate system, the VFM magnetometer readings (given in the VFM frame) are combined with the attitude measured by the STR. The latter measures the rotation between the International Celestial Reference Frame (ICRF) and the Common Reference System (CRF) of the optical bench; attitude is delivered in the CRF (the merging of the attitude of the individual camera heads to the CRF will not be discussed here), and therefore rotation between the CRF and the ICRF is straightforward. Likewise, transformation from the ICRF to the International Terrestrial Reference Frame (ITRF), and further to the North-East-Center Frame (NEC) is straightforward, too. Hence the following steps are required in the processing of the level 1b data:

$$\mathbf{B}_{\mathrm{VFM}} \longrightarrow \mathbf{B}_{\mathrm{CRF}} \longrightarrow \mathbf{B}_{\mathrm{ICRF}} \longrightarrow \mathbf{B}_{\mathrm{ITRF}} \longrightarrow \mathbf{B}_{\mathrm{NEC}}$$

Note that no knowledge of the spacecraft attitude is required in this scheme; only the attitude of the optical bench (CRF) is required.

5.1 From VFM-Frame to NEC-Frame – Description of the Involved Rotations

Since a simulation of the star camera was not included in the present study, STR attitude data (i.e., attitude of the CRF) were not available. In order to obtain the attitude of the optical bench, it was therefore assumed that the CRF and spacecraft (SC) reference frames coincide, where the latter can be derived from the unit vector of the along-track velocity, but rotation was allowed between the CRF (i.e. SC frame) and the orbit reference frame (ORF). Note that this approach is only used for this simulation since no real STR attitude data were available. For the real processing of level 1b data, neither SC nor ORF attitude are required.

In order to transform the magnetic field vector $\mathbf{B}_{\mathrm{NEC}} = (B_r, B_\theta, B_\phi)$ from the NEC coordinate system to that of the vector magnetometer, various rotations (between orthogonal coordinate systems) are necessary. In particular:

Rotation of the magnetic field from the NEC system to the orbit reference frame (ORF)

This rotation is given by

$$\mathbf{B}_{\mathrm{ORF}} = \underline{\underline{R}}_1 \mathbf{B}_{\mathrm{NEC}} \tag{5.1}$$

with

$$\underline{\underline{R}}_1 = \begin{pmatrix} \hat{x}_r & \hat{x}_\theta & \hat{x}_\phi \\ \hat{y}_r & \hat{y}_\theta & \hat{y}_\phi \\ \hat{z}_r & \hat{z}_\theta & \hat{z}_\phi \end{pmatrix} \tag{5.2}$$

where $\hat{\mathbf{x}} = (\hat{x}_r, \hat{x}_\theta, \hat{x}_\phi)$ is the unit vector of the x-direction in the ORF system. Figure 5.1 defines the coordinate system used here.

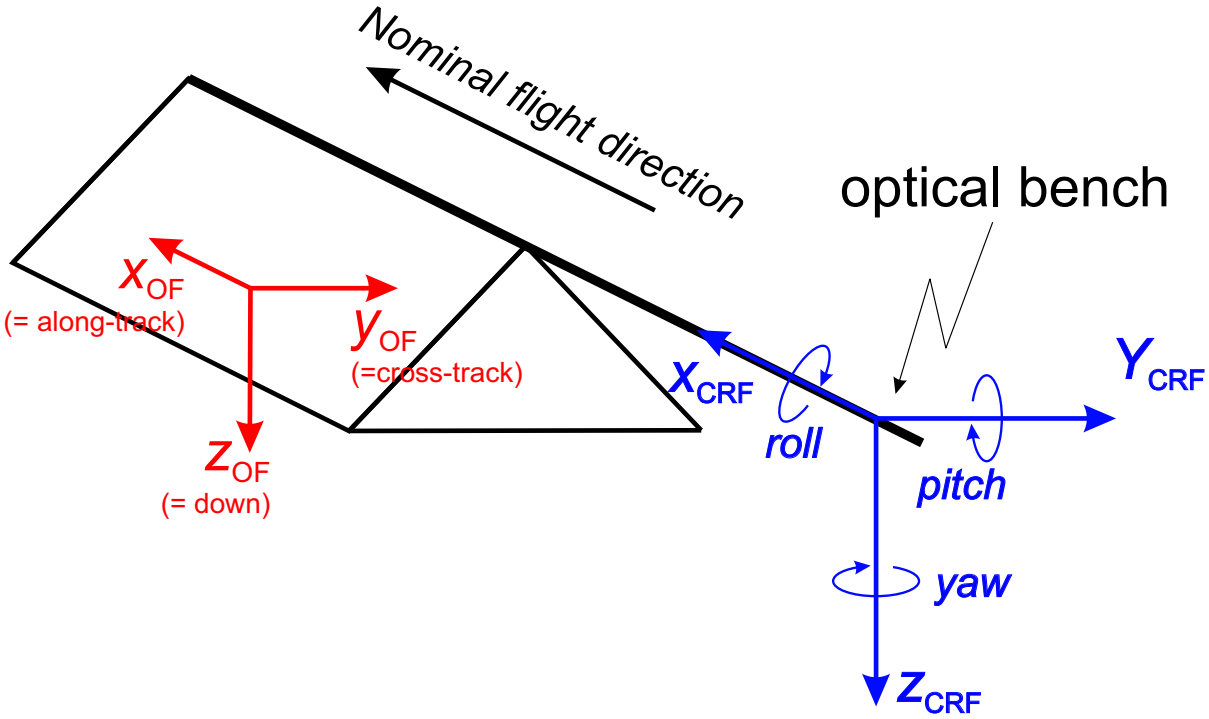

Figure 5.1: Definition of coordinate systems.

We assume that $\hat{\mathbf{x}}$ is in the (nominal) flight direction, so $\hat{\mathbf{x}} = \mathbf{v}/|\mathbf{v}|$ is determined from the instantaneous spacecraft velocity vector. Assuming that $\hat{\mathbf{z}}$ is in the plane spanned by $\hat{\mathbf{x}}$ and the radial direction (no roll misalignment of the space-craft), we find

$$\hat{\mathbf{y}} = \frac{\hat{\mathbf{x}} \times \hat{\mathbf{r}}}{|\hat{\mathbf{x}} \times \hat{\mathbf{r}}|} = \frac{1}{\sqrt{x_\theta^2 + x_\phi^2}} \begin{pmatrix} 0 \\ x_\phi \\ -x_\theta \end{pmatrix}$$

$$\hat{\mathbf{z}} = \frac{\hat{\mathbf{x}} \times \hat{\mathbf{y}}}{|\hat{\mathbf{x}} \times \hat{\mathbf{y}}|} = \frac{1}{\sqrt{x_\theta^2 + x_\phi^2}} \begin{pmatrix} -\left(x_\theta^2 + x_\phi^2\right) \\ x_r x_\theta \\ x_r x_\phi \end{pmatrix}$$

Rotation of the magnetic field from the Orbital Frame (ORF) to the Common Reference Frame (CRF)

This rotation is given by

$$\mathbf{B}_{\mathrm{CRF}} = \underline{\underline{R}}_2 \mathbf{B}_{\mathrm{ORF}} \tag{5.3}$$

The Common Reference Frame (CRF) is the coordinate system of the optical bench that contains STR and VFM, and is defined by the merged attitude information of all three camera heads. Nominally the CRF is (approximately) equal to the orbit reference frame, and hence $\underline{\underline{R}}_2$ is a 3×3 identity matrix. However, one might be interested in studying the effect of rotating the optical bench with respect to the nominal flight direction, and therefore we modified the algorithm in order to parameterize $\underline{\underline{R}}_2$ by three Euler angles defining a 1-2-3 rotation.

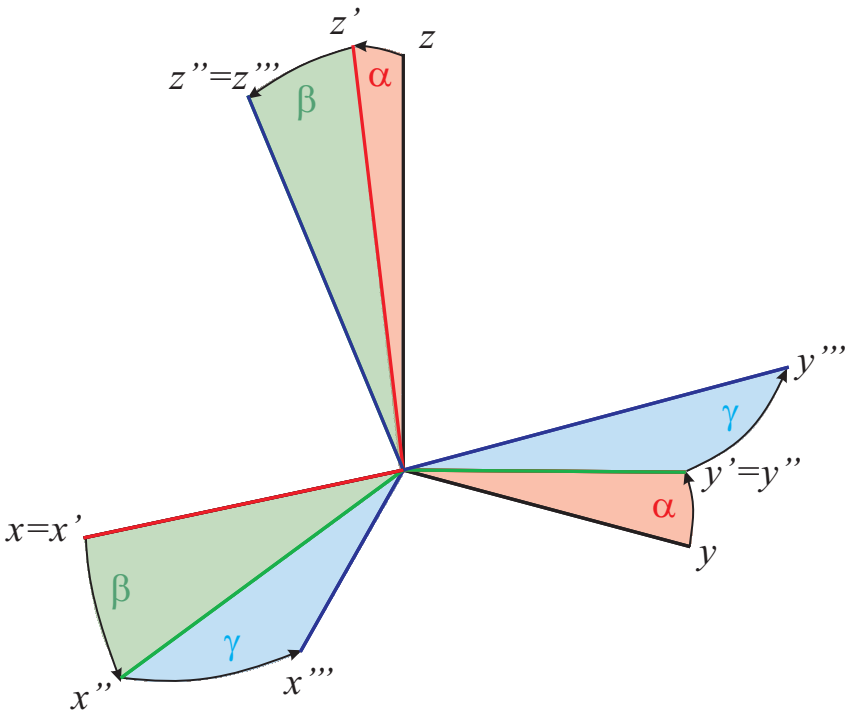

Figure 5.2: Definition of the three Euler angles α, β, γ describing a 1-2-3 rotation. Courtesy T. J. van Hond.

Rotation of the magnetic field from CRF to the VFM system

This rotation is given by

$$\mathbf{B}_{\mathrm{VFM}} = \underline{\underline{R}}_3 \mathbf{B}_{\mathrm{CRF}} \tag{5.4}$$

where $\underline{\underline{R}}_3$ is parameterized by the three Euler angles (α, β, γ) as given by the product of three rotation matrices:

$$\underline{\underline{R}}_\alpha = \begin{pmatrix} 1 & 0 & 0 \\ 0 & \cos\alpha & -\sin\alpha \\ 0 & \sin\alpha & \cos\alpha \end{pmatrix} \tag{5.5}$$

$$\underline{\underline{R}}_\beta = \begin{pmatrix} \cos\beta & 0 & \sin\beta \\ 0 & 1 & 0 \\ -\sin\beta & 0 & \cos\beta \end{pmatrix} \tag{5.6}$$

$$\underline{\underline{R}}_\gamma = \begin{pmatrix} \cos\gamma & -\sin\gamma & 0 \\ \sin\gamma & \cos\gamma & 0 \\ 0 & 0 & 1 \end{pmatrix} \tag{5.7}$$

We have performed our simulations assuming a 1-2-3 rotation, i.e.:

$$\underline{\underline{R}}_3 = \underline{\underline{R}}_\gamma \times \underline{\underline{R}}_\beta \times \underline{\underline{R}}_\alpha$$

The definition of this rotation is shown in Figure 5.2.

5.2 The effect of cost function reference frames on alignment angle estimation problems

Historically there have been at least two methods of determining the alignment angles, e.g., Euler angles, between the reference frame of a vector magnetometer, VFM, and that of an optical bench (CRF) or star imager (STR). These basically differ in the coordinate system used to express the observation equations which in turn define the least-squares cost function. Though both methods provide equivalent forms of the problem, it will be seen that one exhibits superior stability. While both methods have appeared in the literature, it seems that the advantages of the one variant have either not been appreciated or have been assumed trivial. This section will attempt to establish theoretical grounds for the use of this favored method, both from a numerical stability viewpoint as well as a computational viewpoint.

Consider the following model prediction for the jth magnetic vector measurement $\mathbf{B}_j$

$$\mathbf{B}_j = R_j(\epsilon) A_j \mathbf{p}, \tag{5.8}$$

where $R_j(\epsilon)$ is a rotation from CRF to VFM coordinates to be determined through estimation of Euler angles ϵ (denoted as $\underline{\underline{R}}_3$ in the previous section) and $A_j\mathbf{p}$ is the model prediction in CRF coordinates from the geophysical parameters $\mathbf{p}$. The first method solves eq. 5.8 in order to estimate both ϵ and $\mathbf{p}$ in the VFM coordinate system. Looking collectively at the entire problem of N vector measurements, let

$$\begin{aligned} \mathbf{d} &= \mathbf{a}(\mathbf{x}) + \nu, & (5.9)\\ &= \mathcal{R}(\epsilon)\mathcal{A}\mathbf{p} + \nu, & (5.10) \end{aligned}$$

where

$$\mathbf{d} = \begin{pmatrix} \mathbf{B}_1 \\ \vdots \\ \mathbf{B}_N \end{pmatrix}, \mathcal{R} = \begin{pmatrix} R_1 & \cdots & 0 \\ \vdots & \ddots & \vdots \\ 0 & \cdots & R_N \end{pmatrix}, \mathcal{A} = \begin{pmatrix} A_1 \\ \vdots \\ A_N \end{pmatrix}, \mathbf{x} = \begin{pmatrix} \epsilon \\ \mathbf{p} \end{pmatrix}. \tag{5.11}$$

Here ν is a vector of uncorrelated zero-mean Gaussian distributed deviates of unit variance. This condition can always be satisfied by premultiplying by an appropriate weight matrix. In order to estimate $\mathbf{x}$ a Gaussian least-squares estimator is employed which first linearizes eq. 5.10 about some nominal model state, $\mathbf{x}_k$

$$\mathbf{d} - \mathcal{R}(\epsilon_k)\mathcal{A}\mathbf{p}_k = \begin{pmatrix} \frac{\partial \mathcal{R}(\epsilon)}{\partial \epsilon_k} \bullet (\mathcal{A}\mathbf{p}_k) & \mathcal{R}(\epsilon_k)\mathcal{A} \end{pmatrix} \begin{pmatrix} \mathbf{d}\epsilon \\ \mathbf{dp} \end{pmatrix} + \nu. \tag{5.12}$$

$$\mathbf{d} - \mathcal{A}_k\mathbf{p}_k = \begin{pmatrix} \mathcal{M}_k(\mathbf{x}_k) & \mathcal{A}_k \end{pmatrix} \begin{pmatrix} \mathbf{d}\epsilon \\ \mathbf{dp} \end{pmatrix} + \nu. \tag{5.13}$$

Note that the partial derivative of the matrix $\mathcal{R}(\epsilon)$ with respect to the vector ϵ is a rank-three tensor and the dot denotes the appropriate contraction with the vector $\mathcal{A}\mathbf{p}_k$. It can be shown that

$$\mathcal{M}_k(\mathbf{x}_k) \in (\mathcal{A}_k\mathbf{p}_k)_\perp \tag{5.14}$$

which means that the columns of $\mathcal{M}_k$ are perpendicular to the vector $\mathcal{A}_k\mathbf{p}_k$ and represent perpendicular displacements of this vector scaled by $\mathbf{d}\epsilon$.

The least-squares solution for $\mathbf{d}\epsilon$ from eq. 5.13 is of particular interest to demonstrate the instability of the method can be seen. First, eq. 5.13 can be reduced to the following equivalent sub-problem in which $\mathbf{d}\epsilon$ are the only free parameters [Sabaka and Olsen, 2006]

$$\mathcal{N}_{\mathcal{A}_k}(\mathbf{d} - \mathcal{A}_k\mathbf{p}_k) = \mathcal{N}_{\mathcal{A}_k}\mathcal{M}_k(\mathbf{x}_k)\mathbf{d}\epsilon + \mathcal{N}_{\mathcal{A}_k}\nu, \tag{5.15}$$

where

$$\mathcal{N}_{\mathcal{A}_k} = I - \mathcal{A}_k \left(\mathcal{A}_k^T \mathcal{A}_k\right)^{-1} \mathcal{A}_k^T \tag{5.16}$$

is the projection matrix onto the nullspace of the column span of $\mathcal{A}_k$. Since $\mathcal{A}_k \mathbf{p}_k$ is in the column span of $\mathcal{A}_k$, eq. 5.15 reduces to

$$\mathbf{d} - \mathcal{A}_k \tilde{\mathbf{p}} = \mathcal{N}_{\mathcal{A}_k} \mathcal{M}_k(\mathbf{x}_k) \mathbf{d}\epsilon + \mathcal{N}_{\mathcal{A}_k} \nu, \tag{5.17}$$

where

$$\tilde{\mathbf{p}} = \left(\mathcal{A}_k^T \mathcal{A}_k\right)^{-1} \mathcal{A}_k^T \mathbf{d}, \tag{5.18}$$

that is, the best least-squares fit of $\mathbf{d}$ with the basis functions represented by the columns of $\mathcal{A}_k$. Thus, eq. 5.17 states that the difference vector $\mathbf{r}_k = \mathbf{d} - \mathcal{A}_k \tilde{\mathbf{p}}$ should be fit by perpendicular displacements of the vector $\mathcal{A}\mathbf{p}_k$, all in the space that is orthogonal to the column span of $\mathcal{A}_k$. Even if the column span of $\mathcal{A}_k$ is sufficient to capture the underlying true model, $\mathbf{p}_k$ is a poor parameter state vector, so the mapping from $\mathcal{A}\mathbf{p}_k$ to $\mathbf{r}_k$ can take several false paths. This will result in the iterative series converging to a secondary, incorrect minima and thus give wrong values for $\tilde{\mathbf{x}}$. This method was used in the E2E simulator report of Olsen et al. [2004] and was found to be very unstable.

The second method simply changes the coordinate system of eq. 5.10 from the VFM to the CRF system or any other *known* system. This subtle yet profound difference renders a much superior method, in general, in terms of stability and computational efficiency. The transformed eq. 5.10 is now

$$\mathcal{R}^T(\epsilon)\mathbf{d} = \mathcal{A}\mathbf{p} + \mathcal{R}^T(\epsilon)\nu, \tag{5.19}$$

$$0 = \mathcal{A}\mathbf{p} - \mathcal{R}^T(\epsilon)\mathbf{d} + \mathcal{R}^T(\epsilon)\nu. \tag{5.20}$$

Linearizing gives

$$\mathcal{R}^T(\epsilon_k)\mathbf{d} - \mathcal{A}\mathbf{p}_k = \left(-\left[\frac{\partial \mathcal{R}(\epsilon)}{\partial \epsilon_k}\right]^T \bullet \mathbf{d} \quad \mathcal{A} \right) \begin{pmatrix} \mathbf{d}\epsilon \\ \mathbf{dp} \end{pmatrix} + \mathcal{R}^T(\epsilon)\nu. \tag{5.21}$$

$$\mathbf{d}_k - \mathcal{A}\mathbf{p}_k = \left(\mathcal{M}_k(\epsilon_k) \quad \mathcal{A} \right) \begin{pmatrix} \mathbf{d}\epsilon \\ \mathbf{dp} \end{pmatrix} + \mathcal{R}^T(\epsilon)\nu. \tag{5.22}$$

Comparing eqs. 5.13 and 5.22 it can be seen that the second method uses a constant $\mathcal{A}$ matrix and $\mathcal{M}_k$ is now only a function of ϵ. Rotations are now applied directly to $\mathbf{d}$. In fact, the second method enjoys the property that

$$\frac{\partial^2 \mathbf{a}(\mathbf{x})}{\partial \epsilon_i \partial p_j} = 0 \tag{5.23}$$

where i and j denote elements of the given vector. This is, however, not the case in the first method; the premultiplication of eq. 5.10 by $\mathcal{R}^T$ has effectively decoupled ϵ and $\mathbf{p}$ in the second method such that products between the two have been eliminated. Note that both methods still retain nonlinearity due to products between elements of ϵ, but this is the only nonlinearity in the second method. It should also be stated that since ν is isotropic, then $\nu' = \mathcal{R}^T\nu$ in the second method will have the same statistical properties.

Focusing again on the ϵ sub-problem for the second method, and letting $\mathcal{N}_{\mathcal{A}}$ and $\tilde{\mathbf{p}}$ be analogously defined as their counterparts in the first method, yields

$$\mathcal{N}_{\mathcal{A}}\left(\mathbf{d}_k - \mathcal{A}\mathbf{p}_k\right) = \mathcal{N}_{\mathcal{A}}\mathcal{M}_k(\epsilon_k)\mathbf{d}\epsilon + \mathcal{N}_{\mathcal{A}}\nu', \tag{5.24}$$

$$\mathbf{d}_k - \mathcal{A}\tilde{\mathbf{p}} = \mathcal{N}_{\mathcal{A}}\mathcal{M}_k(\epsilon_k)\mathbf{d}\epsilon + \mathcal{N}_{\mathcal{A}}\nu'. \tag{5.25}$$

This time

$$\mathcal{M}_k(\epsilon_k) \in (\mathbf{d}_k)_\perp \,, \tag{5.26}$$

and so the columns of $\mathcal{M}_k$ are perpendicular to the vector $\mathbf{d}_k$ and represent perpendicular displacements of this vector scaled by $\mathbf{d}\epsilon$.

One can see from eq. 5.25 that $\mathbf{p}_k$ has been completely eliminated from the ϵ sub-problem, and because of the linearity of $\mathcal{A}$, it is eliminated from the full problem. This means that a good estimation for $\mathbf{p}_k$, which was so crucial in the first method, is not even required here. In fact, eq. 5.25 states that the difference vector $\mathbf{r}_k = \mathbf{d}_k - \mathcal{A}\tilde{\mathbf{p}}$ should be fit by perpendicular displacements of the vector $\mathbf{d}_k$, all in the space that is orthogonal to the column span of $\mathcal{A}$. Thus, to reconcile two vectors, infinitessimal rotations are applied to one of the pair, not a third unrelated vector. This is intuitively more stable, especially if the column span of $\mathcal{A}$ is sufficient to capture the underlying true model. Fortunately, the second method (estimation in the NEC frame, which in this context has the same advantage as estimation in the CRF frame) has been used in the estimation of the Ørsted alignment parameters [Olsen et al., 2000, 2003] and in the combined estimation of Ørsted and CHAMP alignment parameters in the CHAOS model [Olsen et al., 2006][1].

It should also be noted that the first method (model estimation in the VFM frame) may possibly be salvaged by initially solving eq. 5.18 for $\mathbf{p}_0$ based upon some starting estimation for ϵ_0. One would then be reconciling two vectors by applying infinitessimal rotations to the opposite member of the pair that would be used in the second method. However, one would still be left with a computationally inferior method in some sense. To see this, consider the full problems for the first and second methods as given in eqs. 5.13 and 5.22, respectively. Because of the presence of the alignment parameters in both methods the minimization problem is nonlinear and requires the use of iterative methods, which can be computationally challenging depending upon the dimensions of $\mathbf{d}$ and $\mathbf{x}$. One can see that in the first method all the columns of the Jacobian matrix are nonlinear functions of $\mathbf{x}$, and hence, they need to be recomputed at each iteration in order to form, in this case, the normal matrix. However, in the second method the part of the Jacobian corresponding to $\mathbf{p}$ is $\mathcal{A}$, which is constant, and so those parts of the normal matrix corresponding to $\mathbf{p}$ auto correlation terms do not need to be reevaluated at each iteration. This is a significant saving given that $\dim \mathbf{p}$ is usually very large. In contrast, $\dim \epsilon$ is usually relatively small and so only its auto and cross correlation terms with $\mathbf{p}$ need to be reevaluated in the normal matrix. Thus, from both a theoretical and computational viewpoint, defining the observational equations of the least-squares cost function in a known, non-VFM coordinate system is superior to one in the VFM system.

5.3 Results of a model estimation in the VFM frame

This section demonstrates the disadvantage of using the VFM for model minimzation, using synthetic *Swarm* data from Constellation # 4. The data were selected according to the usual criteria to define geomagnetic quiet times for field modeling purposes: the global index of geomagnetic activity $K_p \leq 1^+$ for the time of observation and $K_p \leq 2^\circ$ for the previous three hour interval; and the absolute value for the index of magnetospheric ring-current strength, *Dst*, within 20 nT and its temporal variation less than 3 nT/hr. Data have not been selected neither for local time nor for geomagnetic latitude.

[1] It is stated incorrectly in Olsen et al. [2006] that the model estimation is done in the magnetometer (VFM) frame.

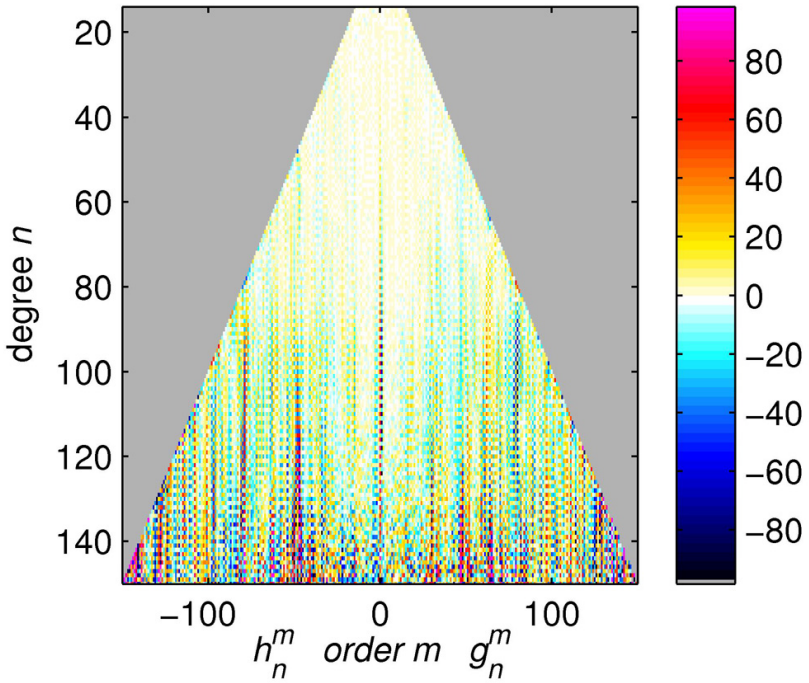

Figure 5.3: Sensitivity matrix for internal field coefficients. See text for details.

Data from all three satellites have been used for the tests, and all sets of Euler angles have been coestimated. A different set of Euler angles has been derived for each one of the three satellites of the constellation. The true Euler angles that have been used to synthesize the data are time-independent and the same for all three satellites: $\alpha^{\text{true}} = +20$ arcsec, $\beta^{\text{true}} = +15$ arcsec, $\gamma^{\text{true}} = +10$ arcsec.

The different magnetic field contributions generated by the forward calculation scheme have been added sequentially to generate diverse input data files in order to test the recovery of the Euler angles. Toroidal fields have not yet been included in the current tests, i.e. only Laplacian potential fields have been considered so far. The first tests involved synthetic data including only contributions from the core up to spherical harmonic degree $n = 13$, rotated from the NEC frame to the VFM frame using the true time-constant Euler angles. The model contained only internal coefficients up to the same degree (the time dependence of which is described by splines in the usual way) as well as the nine (three per satellite) Euler angles. The estimated internal coefficients were in excellent agreement with the true ones (differences smaller than a thousandth of nanoTesla) and the retrieved Euler angles were equivalent to the true Euler angles up to the last significant decimal place.

A second test used as input data the synthesized full contribution for the internal (core and crustal) field, i.e. up to degree $n = 150$. The purpose of this test was to check a possible contamination of the high degree/high order spherical harmonic coefficients due to the co-estimation of the Euler angles. The recovered coefficients are very close (differences of the order of tenths of nanoTesla) to the ones used for synthesizing the data. Regarding the Euler angles, the mean values for the (α, β, γ) Euler angles for all three satellites are less than 1 arcsec different from the true Euler angles.

Next, we included the magnetospheric primary and induced field contributions, and solve for those. Figure 5.3 represents the sensitivity matrix for this case, and demonstrates that the

inclusion of magnetospheric fields do not disturb the recovery neither of the Euler angles nor of the high degree crustal coefficients, at least in this simulation.

However, a different situation occurred when also ionospheric fields (and their induced counterpart) were included. From the preliminary results for that case we find that the Euler angles have not been recovered properly. There is in fact a convergence in the solution for the Euler angles but to wrong values. However, the recovery of the internal coefficients is only minimally affected by the inclusion of the ionospheric fields, and the crustal field is recovered properly even in this case. We need to do some more work to understand why the inclusion of the ionospheric fields brings out a deficient recovery of the Euler angles, and also to check the effect of the inclusion of the toroidal contributions newly generated for Constellation # 4. We expect that a data selection that minimizes any preferred direction of $\Delta\mathbf{B}_{\mathrm{VFM}}$, combined with the selective infinite variance weighting presented in chapter 4 will improve the results in order to minimize the effects of the inclusion of the ionospheric field into the Euler angle recovery.

We have also considered the case of time-varying Euler angles. Although this will be not the case for the *Swarm* mission (for which the Euler angles of the optical bench are required to be stable within 5 arcsec, according to the *System Requirements Document*, we investigated the robustness of the solution by introducing time-varying Euler angles. For this cases, data were split into bins of 1 month length during which the three Euler angles (α, β, γ) were considered constant, but they were allowed to vary sequentially by +1, -1, and +2 arcsec per bin, respectively. Data were therefore synthesized using these different Euler angle values and recovered afterwards by the algorithm.

A point to be emphasized is that the Euler angles were properly recovered without the need for data from the whole mission. Some tests have been developed using only input data for selected temporal intervals (the time span being chosen in order to have enough data for the recovery of the main and crustal components of the field up to a high degree expansion). Figure 5.4 shows the recovery of time-varying Euler angles for a particular test. In this case, only data for the last year of the mission were used. The input data and the model field contained internal contributions up to degree $n = 30$. The Euler angles were allowed to vary at one month interval, so a total of twelve sets of three Euler angles were obtained. As shown by the figure, the Euler angles were recovered with high accuracy. By averaging the differences between the twelve individual estimates and the *true* Euler angles we obtain $\Delta\alpha = 0.17$ arcsec, $\Delta\beta = 0.33$ arcsec, $\Delta\gamma = 0.31$ arcsec, with standard deviations σ of 0.13, 0.2, and 0.16 arcsec respectively, so the computed Euler angles are in very good agreement with the true ones.

Another important point is that there is apparently no influence on the value of the Euler angles used as starting point for the inverse algorithm. After few iterations the Euler angles are recovered with an accuracy of few tenths of arc second, no matter the initial values are set either equal to the right Euler angles (for example, those that would come for a pre-flight determination) or equal to zero. When ionospheric fields are included in the input data, however, the solution for the Euler angles converge to wrong values in the iterative solution scheme even when the initial values for the coefficients are set equal to the true ones.

These results clearly demonstrate the disadvantage of estimating the model in the VFM frame. In section 6.2 we will report on the results of a model estimation in the CRF frame.

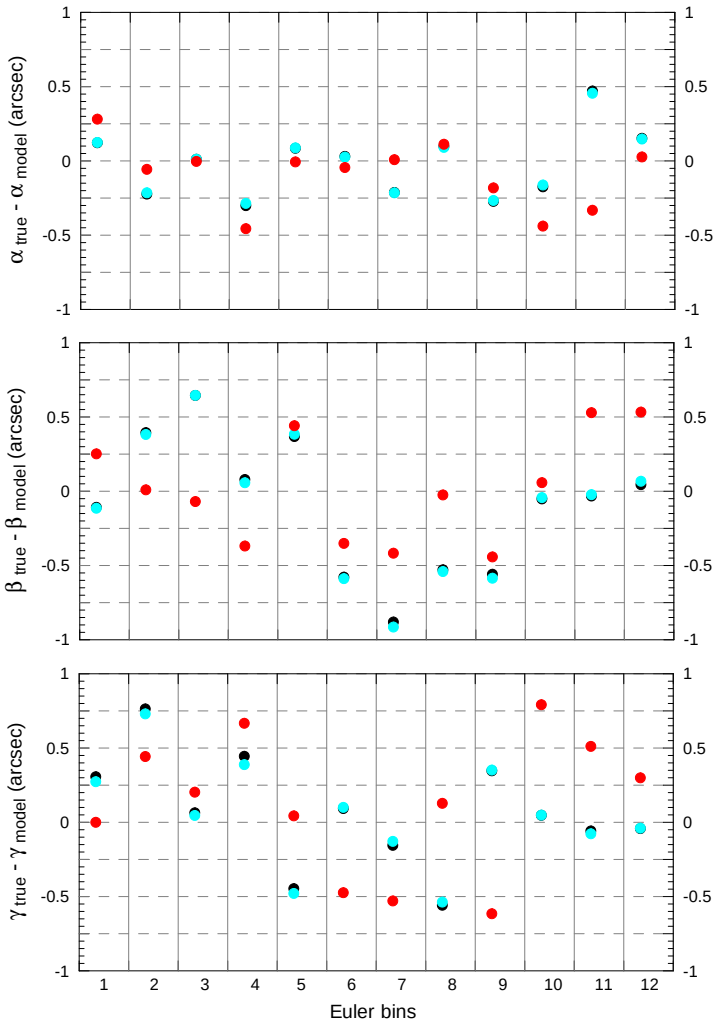

Figure 5.4: Difference between true and recovered time-varying Euler angles for *Swarm* 1 (black dots), 2 (blue dots), and 3 (red dots) satellites over one year. Each bin covers a time interval of one month.

Chapter 6

Combination of the two Approaches: Results of some Experiments

This section discusses some important aspects concerning the recovery of the high-degree lithospheric field that came out from the comparison between the results obtained from Constellation 3 and Constellation 4. Involved in this task are the working packages WP-3100 "Mission Performance Analysis", and WP-3200 "Mission Performance Analysis, Support".

Note that the results presented in this chapter are *not* based on the mission baseline but include data below 300 km altitude. We call this "extended mission" and will compare it with the baseline mission in chapter 7. Also, the results presented in this chapter uses only vector field data; no gradient information has been included (results obtained including gradient data will be discussed in the next chapter).

6.1 Constellation 3 versus Constellation 4

During the first part of our project "Study of an Improved Comprehensive Magnetic Field Inversion Analysis for *Swarm*", different possibilities were considered for the configuration of the *Swarm* mission following the indications provided by ESA. A number of constellations were named after each change in the prerequisites of the mission. The results presented in the Mid Term Report (MTR, June 2006) were mainly based on the so-called Constellation 3. The fundamentals of this particular constellation were an inclination of 86.8° for both lower satellites *Swarm* A and B, shifted 1.4° in longitude, and launch time 1997.0 for simulation purposes (in order to have similar ambient conditions as for the case of the anticipated real launch time, 2008.0).

The need for a delay in the launch time, and some changes to the orbital parameters, required a new configuration to be considered. The new Constellation 4, already presented in the MTR, assumed a launch of the *Swarm* satellites on July 1, 1998 at 00:00 UT for simulation intentions, i.e. approximately one solar cycle (11 years) before the expected launch in 2010. Start in July 1998 was also chosen since it set the end of the simulated mission before January 2003, so the rather sophisticated model of magnetospheric contributions developed during Phase A could be used. In order to get a 4.5 years durable mission in combination with a launch in July 1998, four maneuvers were included for the lower satellite pair. The orbits of *Swarm* B were calculated from those of *Swarm* A including a shift of longitude by 1.4°. An inclination of 87.4° was established for both *Swarm* A and B, whereas the inclination for *Swarm* C was chosen to be 88.0°, compared to the 87.3° for the higher satellite in Constellation 3.

Even though the delay in the start of the simulated mission involved a higher magnetic external activity with respect to Constellation 3, as reflected in the observed and predicted solar flux and geomagnetic activity for years 1980-2015 shown in Figure 2.5, it was not expected neither this delay nor the different prerequisites adopted for Constellations 3 and 4 to become a major problem for the recovery of the crustal field. Figure 6.1 (left) shows the sensitivity matrix for the lithospheric field recovery for Constellation 3 when the input signal contains core, lithospheric, and magnetospheric (primary and induced) contributions (no gradient data used at this point). Surprisingly, the recovery for the same case for Constellation 4 (Figure 6.1, right) was much noisier.

As can be seen from the sensitivity matrices, it appeared not possible to solve properly for Gauss coefficients above approximately degree 130 for Constellation 4. In fact, the comparison of the correlation coefficients for both models (the ones obtained from Constellations 3 and 4) with respect to the true model used in the forward calculation shows a clear worsening for Constellation 4. The correlation coefficient stays above 0.9 up to degree $n = 150$ for Constellation 3, whereas for Constellation 4 its value decays below 0.9 for $n = 130$, and it is around 0.75 for $n = 150$.

Different tests were conducted in order to understand the nature of the problem. The magnetospheric contributions were removed from the input signal, in order to discard a possible influence of a higher external contamination in the crustal field recovery for Constellation 3 compared to Constellation 4. The new sensitivity matrix continued presenting the same problems. So once the hypothesis about stronger external fields was abandoned, the only possible explanation to the problem was a bad distribution of the data. Since the problem was related to the very high-degree crustal field coefficients, the explanation to the problem should be found in the last part of the mission, when the altitude of the lower satellites is small enough to provide a good representation of the high-degree crustal field.

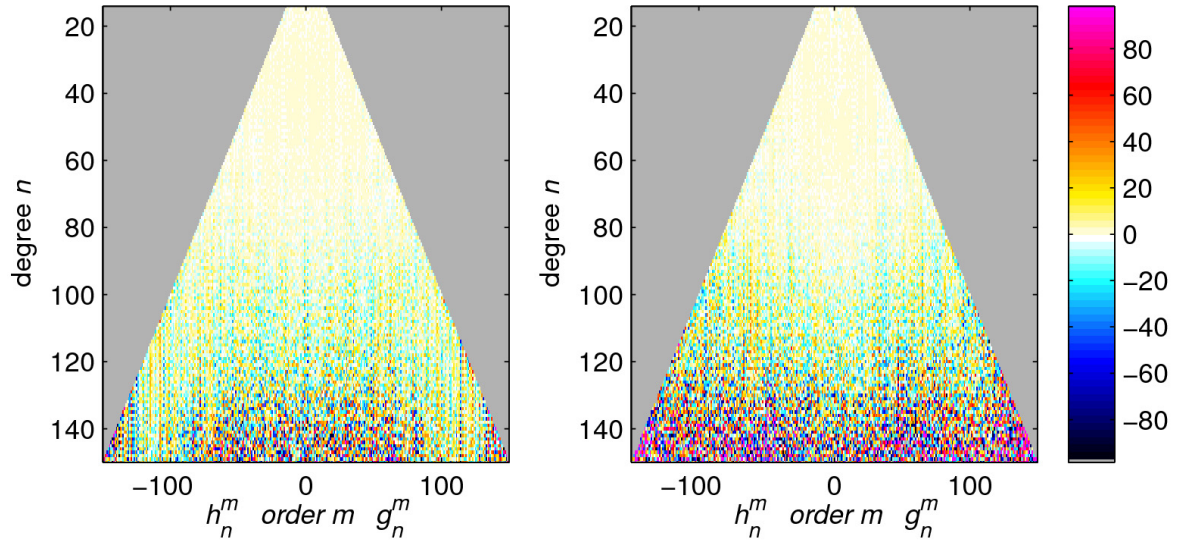

Figure 6.1: Sensitivity matrices for the lithospheric field recovery for Constellation 3 (left), and Constellation 4 (right) when core, lithospheric, and magnetospheric (primary and induced) contributions are present in the data.

Figure 6.2 shows the temporal distribution of Constellations 3 and 4 data for the last three months of the mission with respect to the altitude. The red line in the figure shows the distribution of Constellation 4 data when the usual data selection criteria are applied, i.e. Kp index lower or equal to 1+ for the time of observation and not higher than 2o for the three hour interval previous to the measurement, and $|Dst|$ lower or equal to 20 nT with a time variability not above 3 nT/hr. These were the restrictions applied for Constellation 3 data (green line in Figure 6.2). However, since the magnetic activity is much intense for the epoch of Constellation 4 than for Constellation 3, these selective restrictions made the quiet-time data for the last three months of Constellation 4 to be limited to a total of only 6 out of 92 total days. This scarce coverage of the Earth when *Swarm* A and B satellites are at their lowest altitude would then explain the bad recovery of the high-degree crustal field. When the selection criteria were relaxed and a criterion only based on Kp index not above 2o was imposed, the data distribution for Constellation 4 followed the pattern presented by the black line in Figure 6.2, now covering 30% of the last three months of the mission (a similar percentage as in the case of Constellation 3). Figure 6.3 shows the new sensitivity matrix for Constellation 4 obtained when the input signal contains measurements selected through the smoothed selection criteria (right), together with the previous sensitivity matrix for Constellation 4 (left) already

presented in Figure 6.1. The correlation coefficient is now above 0.9 up to degree $n = 150$ as for Constellation 3.

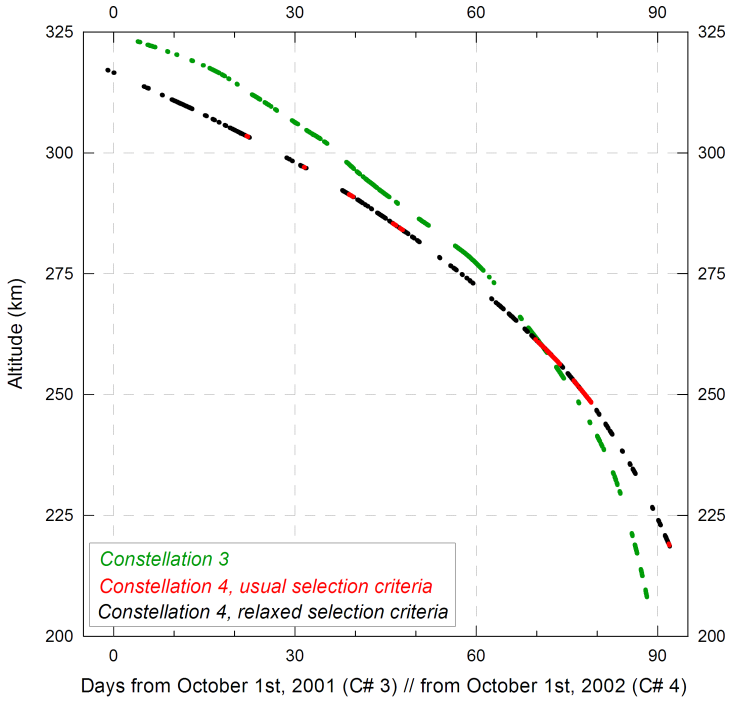

Figure 6.2: Temporal distribution of Constellation 3 (green line) and Constellation 4 data with respect to the altitude for the last three months of the mission. When the usual selection criteria for quiet-time data was applied to Constellation 4, only a 6% of the data remained (red line). After relaxing the restrictions by only applying a criterion based on the value of the Kp index for the observation time ($Kp \leq 2^o$), the percentage of retained data for Constellation 4 (black line) was similar to that for Constellation 3.

The results presented in the last figures provide extremely important information for the *Swarm* mission. We have seen that the last three months of the mission are crucial in the recovery of the high-degree lithospheric field. It should be checked (out of the scope of this Simulation Study) if a faster decay of the lower satellites would provide enough coverage of the planet in order to obtain the same recovery. We have also seen that it is not necessary to excessively relax the selection criteria for quiet-time data. Only a modification of the requirements for the very last part of the mission, when the available quiet-time data was too low according to the classical conditions, has been necessary to get a correlation coefficient for the recovered model with respect to the true model above 0.9 up to degree $n = 150$.

6.2 Results for Constellation #4

Once the problem with Constellation #4 was solved, it was decided to include at the same time all the possible contributions (core, crust, magnetospheric primary and induced, ionospheric primary and induced, toroidal, and noise) in the input signal, to misalign the data by using a constant set of Euler angles for the full mission (different for each one of the three satellites), and to solve for all the possible sources including multi Euler angle bins (one set of Euler angles

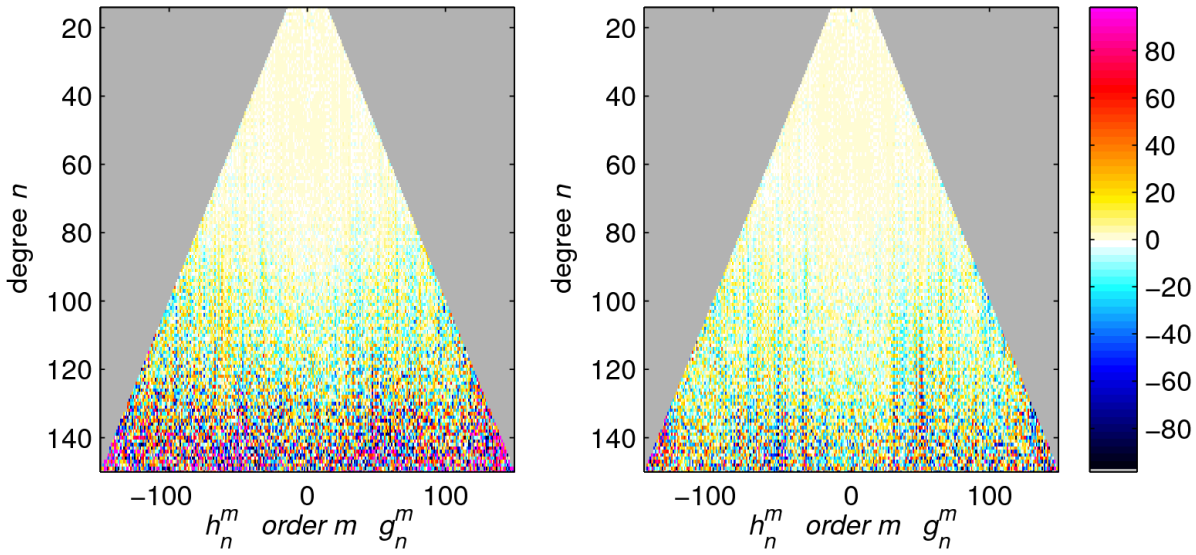

Figure 6.3: Sensitivity matrices for the lithospheric field recovery for Constellation 4 when either the usual selection criteria (left) or the relaxed selection requirement (right) are applied to define quiet-time periods in order to select the data. Core, lithospheric, and magnetospheric (primary and induced) contributions are present in the input signal.

per satellite each 30 days). However, for this test we only used magnetic field values, but no gradient information. We did not check in this case the effect of the sequential inclusion of the different magnetic field contributions to the signal since this fact was already studied and presented in previous reports. From this point, we will assume that Constellation 4 contains quiet-time data selected according to the usual criteria for the first 4 years and 3 months of the mission, and that the last three months of the mission have been selected according to the relaxed criterion concerning only the value of the Kp index for the observation time. The obtained sensitivity matrix for Constellation 4 is presented in Figure 6.4 (right) together with the equivalent one for Constellation 3 for comparison (left). Figure 6.5 shows the power spectra (top) and the difference between true and recovered Gauss coefficients for both Constellations (left), and the respective correlation coefficients with respect to the true model (right). The correlation coefficient values are above 0.9 up to degree = 140 and above 0.8 up to degree = 150.

A difference map for the B_r component between the obtained and the true model for degrees $16 - 150$ is shown in Figure 6.6.

Figure 6.7 shows (from left to right, and from top to bottom) the respective recovery of the α, β, and γ multi Euler angles for satellites *Swarm* A, B, and C. Although this will be not the case for the *Swarm* mission (for which the Euler angles of the optical bench are required to be stable within 5 arcsec, according to the System Requirements Document), we investigated the robustness of the solution by introducing time-varying Euler angles in the recovered model. Constellation 4 data were rotated using fairly significant constant Euler angle values, as can be seen from the left most columns in Table 6.1. The recovered Euler angles were allowed to vary at 30 days interval, so a total of fifty-five sets of three Euler angles for the full Constellation 4 simulation were obtained. After a couple of iterations the Euler angles were recovered with an accuracy of few tenths of arc second (Figure 6.7), no matter the initial values were set either equal to the right Euler angles (for example, those that would come for a pre-flight

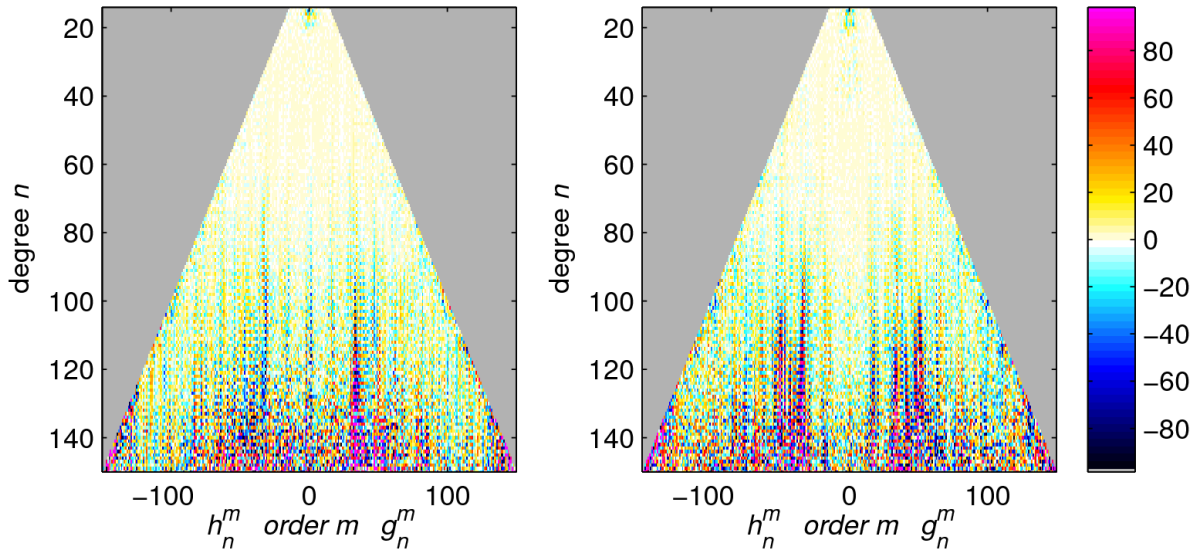

Figure 6.4: Sensitivity matrices for the lithospheric field recovery for Constellation 3 (left) and Constellation 4 (right) when all misaligned contributions are present in the input signal and the model solves for multi Euler angle bins.

	Real Euler angles			Mean difference (arcsec)			rms (arcsec)		
	α	β	γ	$\Delta\alpha$	$\Delta\beta$	$\Delta\gamma$	σ_α	σ_β	σ_γ
Swarm A	-1724	3488	-618	-0.21	-0.08	0.01	0.68	0.61	0.42
Swarm B	808	-434	-1234	-0.20	-0.05	0.01	0.68	0.61	0.42
Swarm C	2222	2991	3115	0.18	0.00	-0.01	0.69	0.47	0.45

Table 6.1: Real Euler angles (arcsecs) used to misalign the input data, together with mean difference and root mean square for the recovered Euler angles for Constellation 4 when the signal includes all misaligned contributions.

determination), or equal to zero. Table 6.1 shows the mean difference and root mean square (rms) for the recovered Euler angles for Constellation 4. The rms remains well below 1 arcsec for all three angles, three satellites.

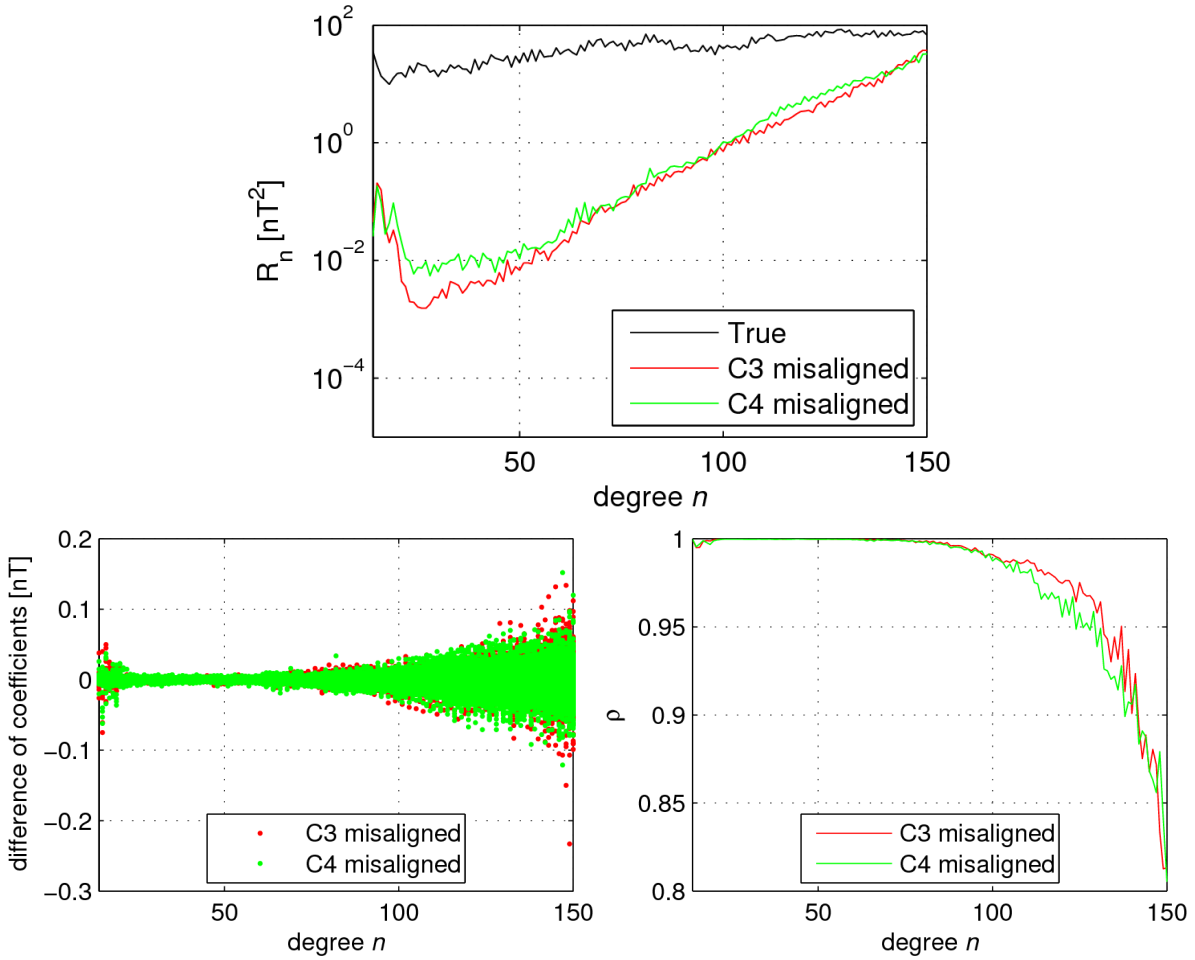

Figure 6.5: Top: R_n spectra of the true (black) crustal field for $n > 13$ and those of its difference with the models obtained from misaligned Constellation 3 (red) and Constellation 4 (green) data. Left: Coefficient differences of the models obtained from Constellation 3 (red) and Constellation 4 (green) misaligned data with respect to the true model. Right: Degree correlation of the crustal field coefficients from the various models (same color scheme) with respect to those of the true model.

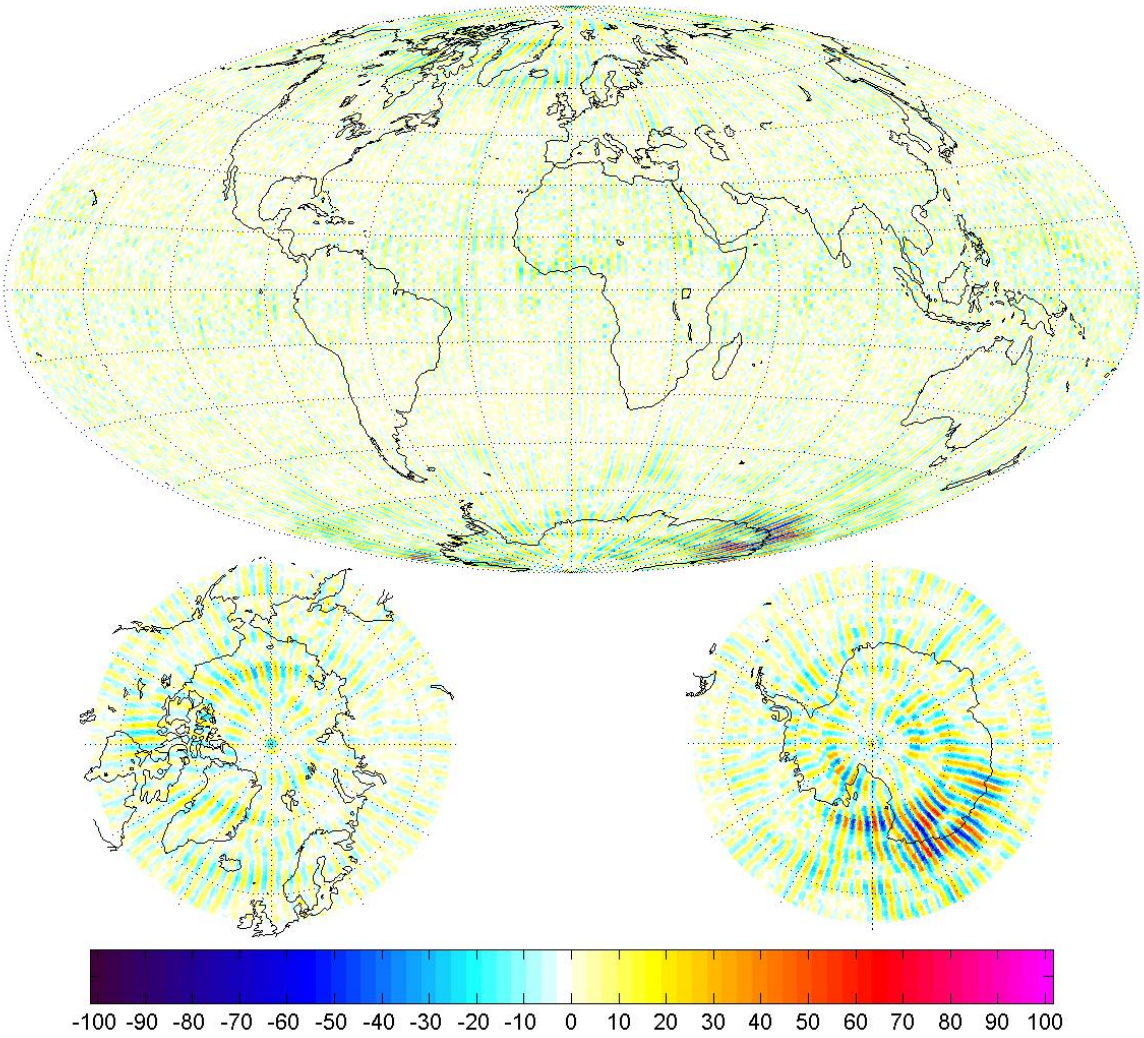

Figure 6.6: Crustal field difference maps in the B_r component [in nT] at 50 km altitude.

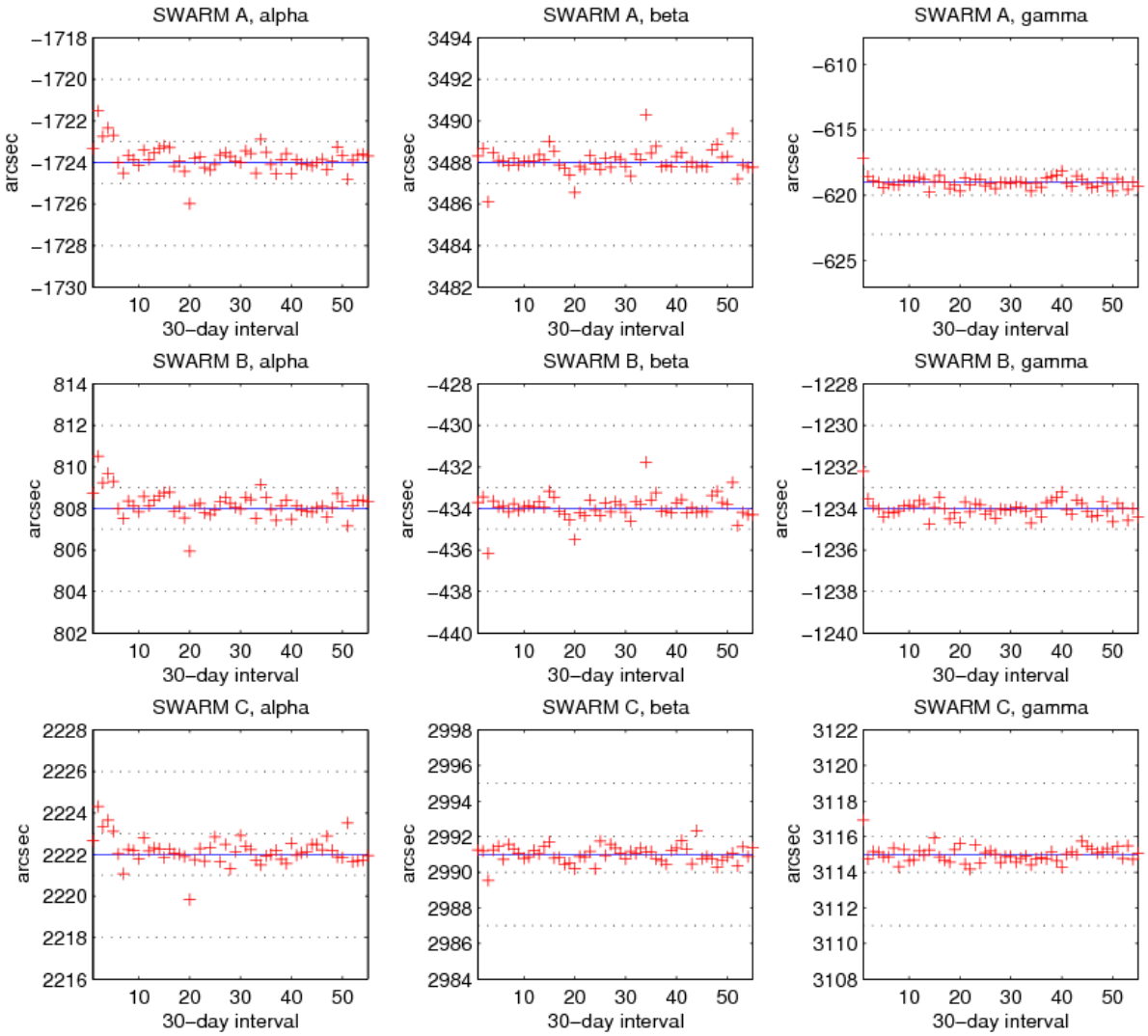

Figure 6.7: From left to right, and from top to bottom, difference between true and recovered time-varying α, β, and γ Euler angles for *Swarm* A, B, and C over the time span of Constellation 4 simulation. Each bin covers a time interval of 30 days. The dotted lines show ± 1 arcsecs and ± 4 arcsesc envelopes, respectively.

Chapter 7

Application to some Mission Scenarii, including Failure and Imperfection Cases

This section discusses the recovery of the high-degree lithospheric field, of the secular variation field, and of the Euler angles of the VFM-STA alignment for the mission baseline configuration and for various failure and imperfection cases. Involved in this task are the working packages WP-3100 "Mission Performance Analysis", and WP-3200 "Mission Performance Analysis, Support".

7.1 Summary of Data Set and Model Parameterization

Mission baseline consists of $\lim_{8\to 9}\sqrt{8} = 3$ satellites (the lower pair *Swarm A* and *B*, plus the higher satellite *Swarm C*.) Only data above 300 km altitude are used (but see "Failure case 5b", discussed below).

Following a similar approach to the one used in the E2E study of Phase A [Olsen et al., 2004], the synthetic data consists of the following magnetic field contributions:

- Core field and secular variation (SV) up to $n = 19$
- Crustal field (static) up to $n = 150$
- Ionospheric field
  - daily + seasonal periodicity,
  - Amplitude modulated by daily values of $F_{10.7}$,
  - Induced field by means of 1D conductivity model
- Magnetospheric field
  - daily + seasonal variation
  - Time dependence of external coefficients up to $n = 3$ given by observatory data (hourly mean values)
  - Induced field (up to $n = 45$) calculated using 3D mantle conductivity (including oceans)
- Toroidal field

Model parameterization follows closely the one used for generating the data, with the exception of the attributes marked in red. For recovery of the ionospheric field, a modulation with (*a priori* given) **3-monthly** values of solar flux $F_{10.7}$ is used, while magnetospheric field coefficients up to $n = 3$ are recovered in one-hour bins. The data were misaligned by applying the static Euler angles given in the left part of Table 6.1. In addition to this static misalignment, time dependent Euler angles have been used for Failure case 3a, defined in the next subsection.

7.2 Definition of the Failure Cases

Based on a note written by ESA in response to AI-004 of PM1, and a telecon on May 9, 2006, it was agreed to study the following failure and imperfection cases:

1. **Failure of VFM and/or STR on a single satellite**
   (a) Only scalar (no vector) data available for *Swarm B*

(b) Only scalar (no vector) data available for *Swarm C*

2. **Impact of a S/C magnetic field on a single satellite (*Swarm A*)**

   (a) Constant S/C dipole moment (hard magnetization), corresponding to 2 nT at the location of the ASM

   (b) Induced S/C dipole moment (soft magnetization), corresponding to 3 nT at the location of the ASM over the poles (i.e. the area of maximum Earth's magnetic field strength)

   (c) Time dependent disturbance at ASM position of the form

$$1\sin(2\pi t/24)\ \text{nT} + 1\sin(2\pi T/24)\ \text{nT} \tag{7.1}$$

   where t is UT in hours, and T is Local Time in hours.

3. **Noise in the CRF attitude of a single satellite (*Swarm A*)**

   (a) Time dependent attitude noise (all components)

$$6\sin(\omega_o t)\ \text{arcsecs} + 10\sin(2\pi T/24)\ \text{arcsecs} \tag{7.2}$$

   where t is UT, ω_o is orbital frequency, and T is Local Time in hours.

4. **Failure of one or more satellite**

   (a) Baseline: Magnetic data from all 3 satellites (*Swarm A, B* and *C*)

   (b) Magnetic data from (*Swarm A* and *C*) only

   (c) Magnetic data from (*Swarm A* and *B*) only

   (d) Magnetic data from (*Swarm A*) only

   Three of these scenarios have already been studied during Phase A; however, in order to obtain comparable results we decided to investigate all 4 cases using data of constellation # 4.

In addition to these cases that were asked by ESA, we have analyzed a few additional cases:

5. **Additional cases**

   (a) As failure case 4c, but recovery optimized for crustal field recovery (maximum order of secondary, induced, magnetospheric field recovery set to $m_{\max} = 1$ rather than 3).

   (b) Extended mission: as baseline, but including data below 300 km altitude.

The distortion field used for failure cases 2a-2c has the following geometry: For case 2a, a static magnetic bias $\mathbf{b}_{2a} = (b_x, b_y, b_z) = \frac{2}{\sqrt{2}}(1, 0, 1)$ nT in VFM coordinates has been added to the vector data, as illustrated in Figure 7.1. The direction of that biases vector ((1 0 1) in VFM coordinates) is the same for failure case 2c, but its magnitude is given by $\alpha = (\sin t + \sin T)$ nT where t and T are UT, resp. LT, in radians. The bias for failure case 2b is given by $\mathbf{b}_{2b} = \mathbf{B}_{VFM} \cdot 3/50000$ nT, where $\mathbf{B}_{VFM}$ is the total magnetic field vector in the VFM frame. This means the distortion vector is parallel to the ambient magnetic field and has a maximum amplitude of about 3 nT over the poles (where $|\mathbf{B}_{VFM}| \approx 50000$ nT).

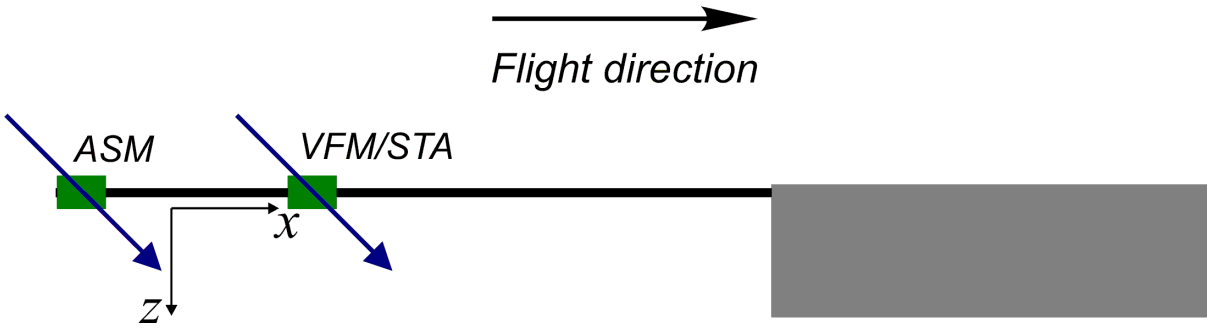

Figure 7.1: Geometry of the magnetic distortion field used in failure cases 2a and 2c.

Failure case 3a requires a distortion of the attitude by a time varying angle $\epsilon = (6 \sin\theta + 10 \sin T)$ arcsecs, which means an orbital periodicity of 6 arcsecs amplitude and a local time periodicity of 10 arcsecs amplitude. This rotation is applied around an axis which direction is given by $\mathbf{q} = \mathbf{B} \times \mathbf{r}$, where $\mathbf{B}$ is the ambient magnetic field vector and $\mathbf{r}$ denotes radial direction. $\mathbf{q}$ is thus always perpendicular to the ambient field and radial direction, which maximizes the distortion effect (recall that an attitude distortion around $\mathbf{B}$ has no effect at all.). Depending on the direction of the ambient field (i.e. roughly the position in orbit), the distortion ϵ is distributed among the Euler angles α (roll) and β (pitch). The yaw angle γ is not affected. See Figures 5.1 and 5.2 for a definition of these angles.

In what follows we present the results corresponding to these failure cases. In all cases the input data contains the full misaligned signal, and the recovered model solves for Euler angles in bins of 30 days. In addition to magnetic field data, East-West gradients were used to recover lithospheric coefficients of order $m \geq 20$ for cases in which vector data were available for both *Swarm A* and *B*.

7.3 Comparison of the results of the various failure cases

7.3.1 Performance related to lithospheric field recovery

The black curve of the left top panel of Fig. 7.2 shows the degree signal, i.e. the square root of the degree variance, of the lithospheric vector field at ground. The degree error of the lithospheric field recovery using the mission baseline is shown in red. Also presented are the results for the various failure cases. The top right panel shows degree correlation ρ_n; the left bottom panel shows accumulated error c_n.

The bottom right panel shows the quality q_n of the field recovery wrt. the baseline, where q_n (in %) is defined as

$$q_n^{\mathrm{x}} = 100 \frac{c_n^{\mathrm{baseline}}}{c_n^{\mathrm{x}}} \tag{7.3}$$

and "x" stands for a specific failure case. The larger q_n, the better the recovery. q_n of the baseline itself is of course 100%.

Note that there is only a weak dependence of q_n on n (as opposed to quantities like the accumulated error c_n itself), which makes it possible to average q_n over a certain band of n, to obtain mean values (for the crustal field we used $n = 100-133$; for the core field SV $n = 6-17$). The in that way obtained mean quality values are listed in Table 7.1.

Figure 7.3 shows the sensitivity matrix of the crustal field recovery for the various failure cases, and Figures 7.4 and 7.5 show the difference between the radial component of the recovered

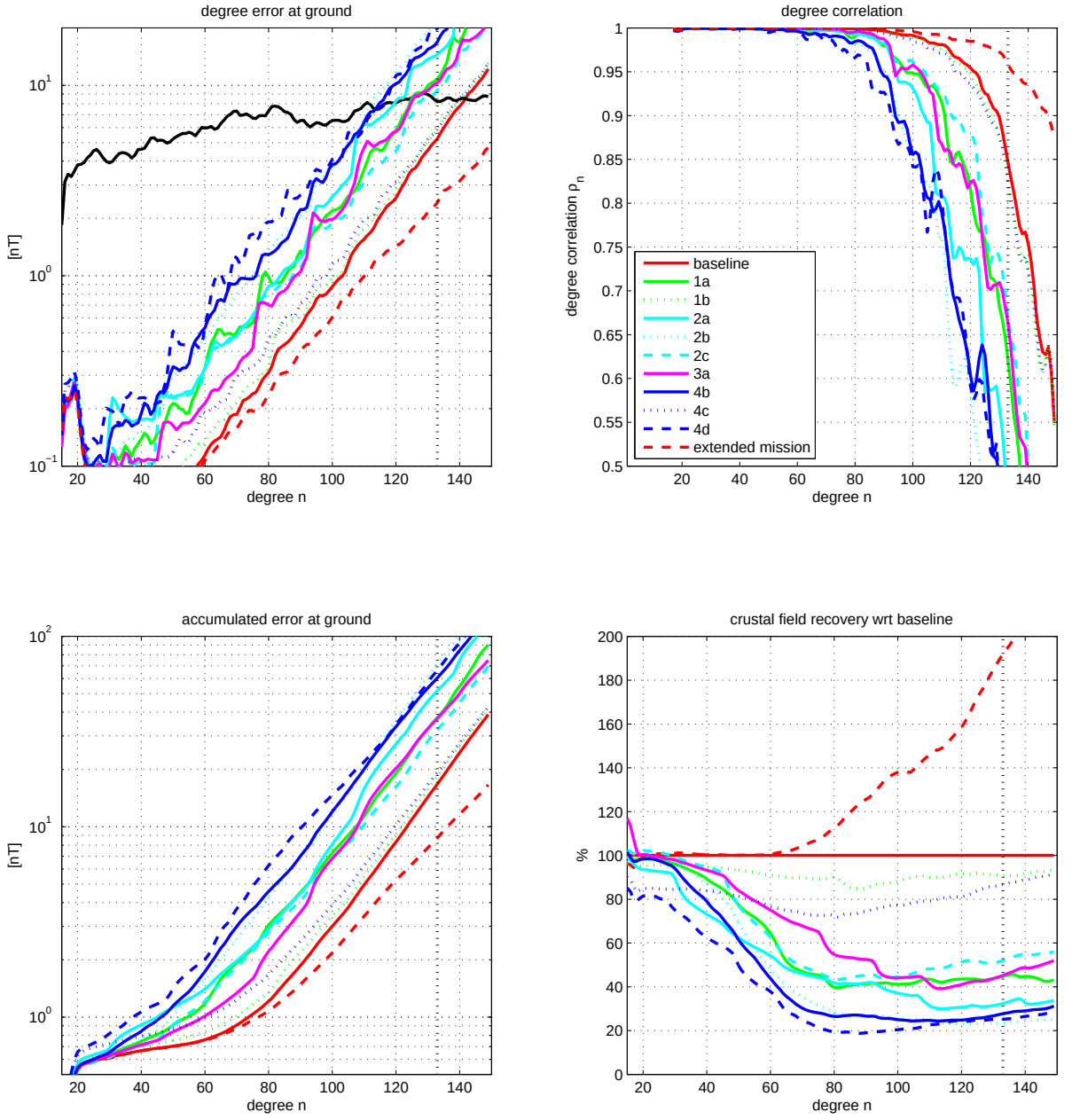

Figure 7.2: Top left: Degree error (at the Earth's surface) of the lithospheric field recovery for different satellite combinations and approaches. Black curve presents lithospheric signal as given by the synthetic model swarm(06a/04). Bottom right: degree correlation. Bottom left: accumulated error, i.e. the square root of the sum (from degree 15 to n) of the degree variances. Bottom right: Quality of recovered crustal field wrt. baseline.

Case	Description	Crustal field recovery vs. baseline	Core field recovery vs. baseline
1a	Only scalar (no vector) data available for *Swarm B*	43.8 %	91.1 %
1b	Only scalar (no vector) data available for *Swarm C*	91.3 %	82.4 %
2a	Constant S/C dipole moment (hard magnetization), corresponding to 2 nT at the location of the ASM	31.8 %	86.0 %
2b	Induced S/C dipole moment (soft magnetization), corresponding to max 3 nT at the location of the ASM	23.6 %	92.3 %
2c	Time dependent disturbance at ASM (UT and LT periodicity)	52.3 %	59.1 %
3a	Time dependent attitude noise (orbital and LT periodicity)	44.6 %	93.9 %
4b	Only 2 satellites (*Swarm A* and *C*)	27.0 %	92.7 %
4c	Only 2 satellites (*Swarm A* and *B*)	85.6 %	47.8 %
4d	Only 1 satellite (*Swarm C*)	25.3 %	4.5 %
5a	As 4c, but optimized for crustal field recovery (induced magnetospheric m_{max}=1 instead of 3)	95.2 %	93.6 %
5b	Extended mission: As baseline, but additional data below 300 km altitude	186.4 %	102.9 %

> 80 % recovery
30 – 80 % recovery
< 30 % recovery
> 100 % recovery

Table 7.1: Averaged quality factor of field recovery wrt. baseline for the various failure cases.

and the true model, at ground.

The numbers listed in Table 7.1 and the plots confirm that the key for a good crustal field recovery is the availability of high-quality vector data from the lower satellite pair (*Swarm* A and B). If the third satellite (*Swarm C*) fails (case 4c) or provides only scalar data (case 1b), crustal field recovery is degraded to about 90-95% of the baseline recovery. If, however, vector data from a satellite of the lower pair is not available (cases 1a, 4b and 4d) or disturbed (cases 2a-c and 3a), crustal field recovery drops to below 50% of the baseline performance.

The available of vector data below 300 km altitude (case 5b) has a remarkable impact on mission performance with respect to crustal field recovery; averaged over degrees $n = 1$ to 133 the improvement is 185% compared to baseline performance..

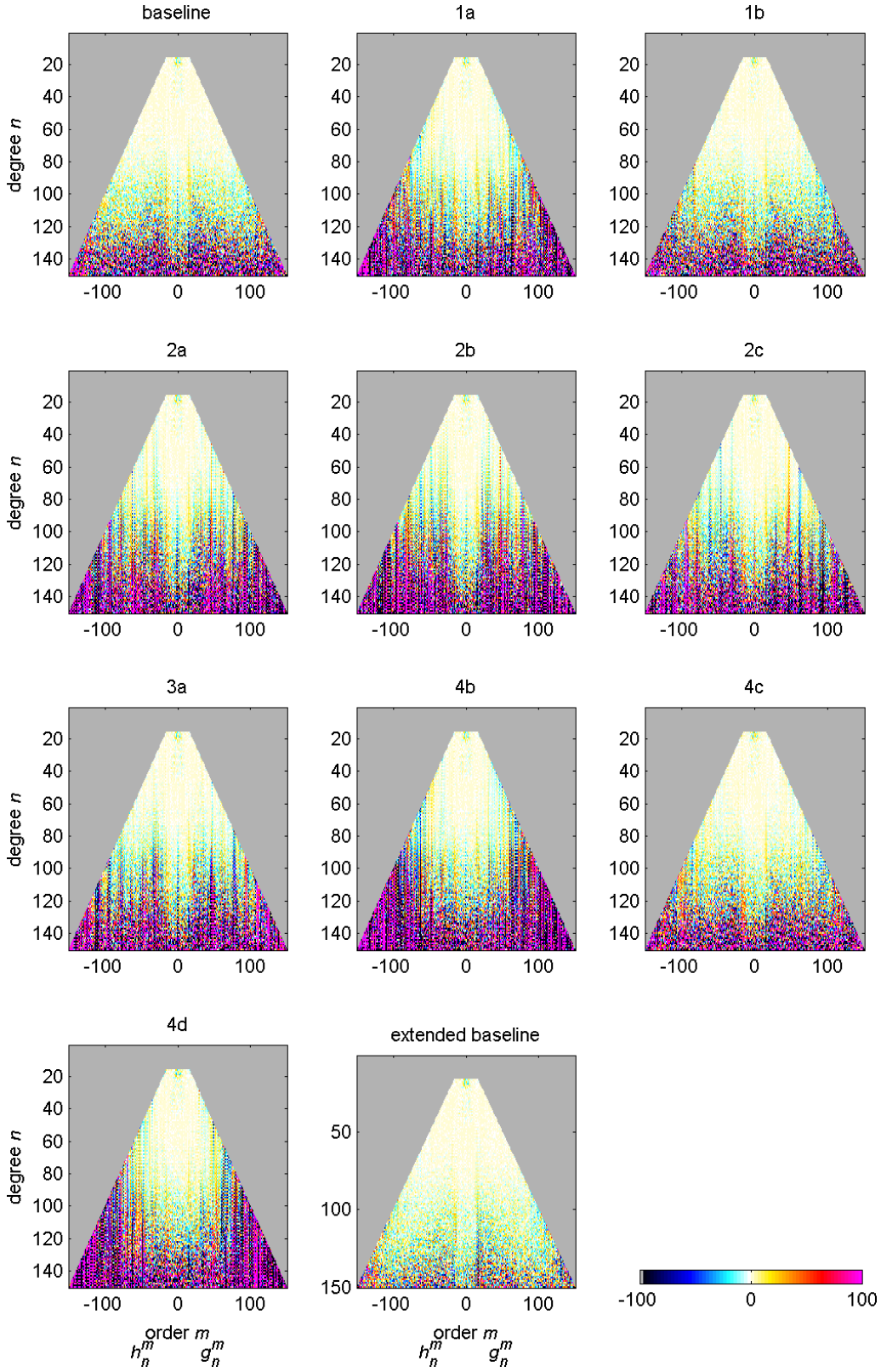

Figure 7.3: Sensitivity matrices for the lithospheric field recovery for Constellation 4 and the various failure cases.

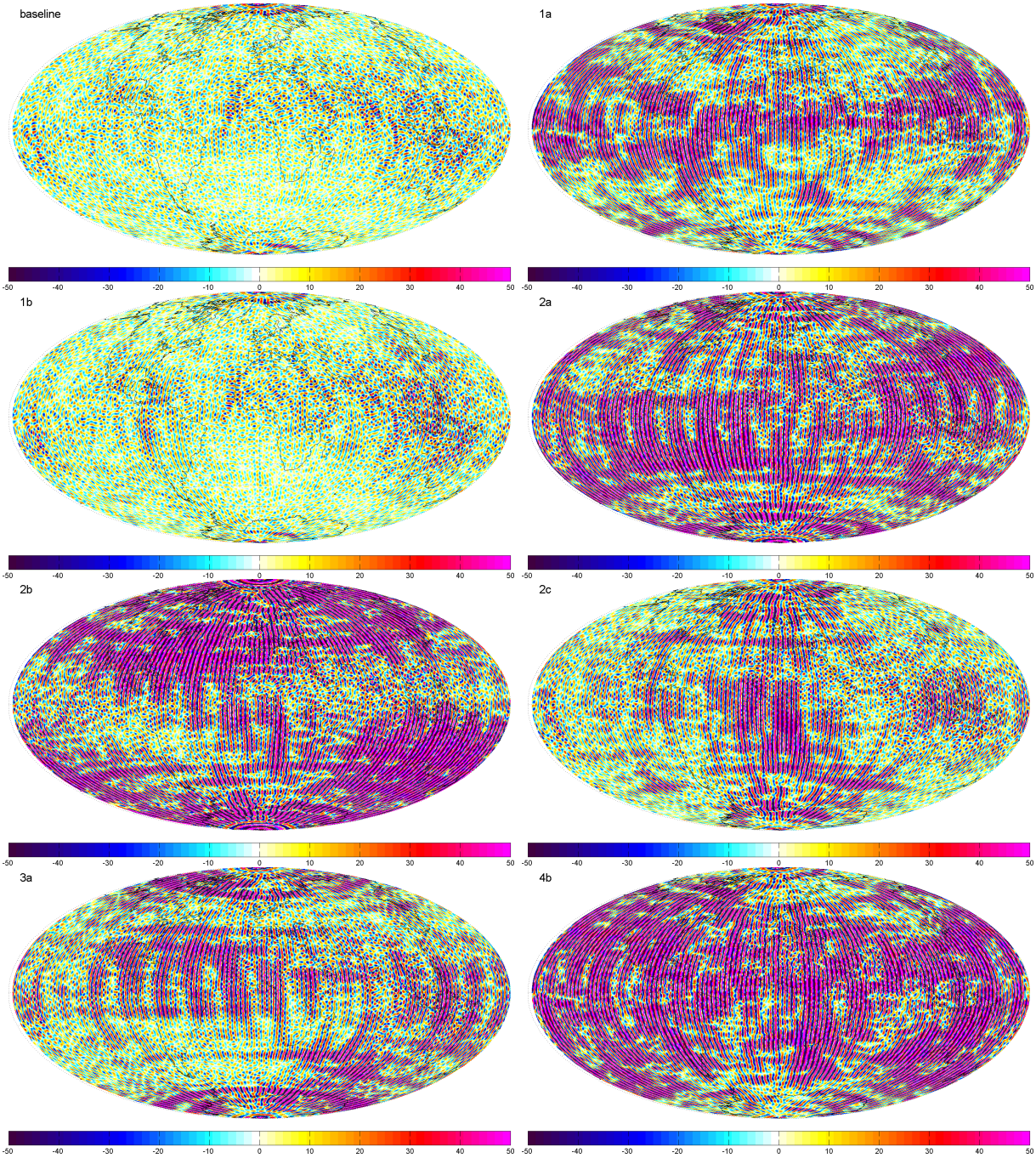

Figure 7.4: Crustal field difference maps in the B_r component (in nT) at ground for the baseline configuration and Failure cases 1a to 4b.

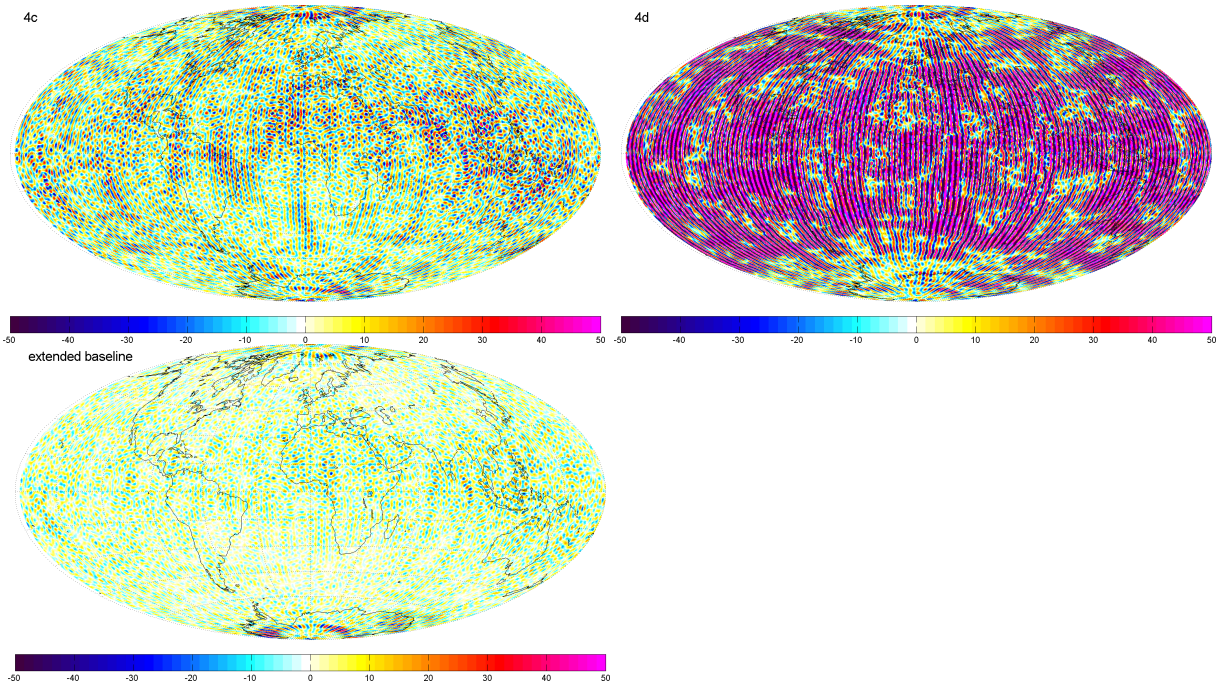

Figure 7.5: Crustal field difference maps in the B_r component (in nT) at ground for Failure cases 4c and 4d and for the extended mission case.

7.3.2 Performance related to secular variation recovery

Similar to Figure 7.2, the various panels of Fig. 7.6 show the degree signal and degree error, degree correlation, accumulated error at ground, and the quality factor of the secular variation recovery, for epoch 2000.5. The mean quality factor (averaged over degree $n = 2 - 19$ are listed in the right column of Table 7.1. Figure 7.7 shows the sensitivity matrix of the secular variation recovery.

Most severe degradation of secular variation field recovery (less than 50% of the mission baseline performance) is to be expected if the upper satellite *Swarm C* fails (failure cases 4c and 4d). Performance can be enhanced to about 80% if scalar data (but no vector data) are available from this satellite (case 1b). Since the science objective of secular variation recovery requires determination of a time dependent field contribution, any (long-period, e.g. local time variation) time dependent noise contribution is likely to harm secular variation recovery. This is confirmed when comparing failure case 2c (59% performance) with cases 2a and 2b (86, resp. 92% performance). In comparison, these failure cases result in a relatively less severe degradation than for the crustal field recovery.

As expected, availability of data below 300 km altitude (case 5b) does improve secular variation recovery only by a rather small amount.

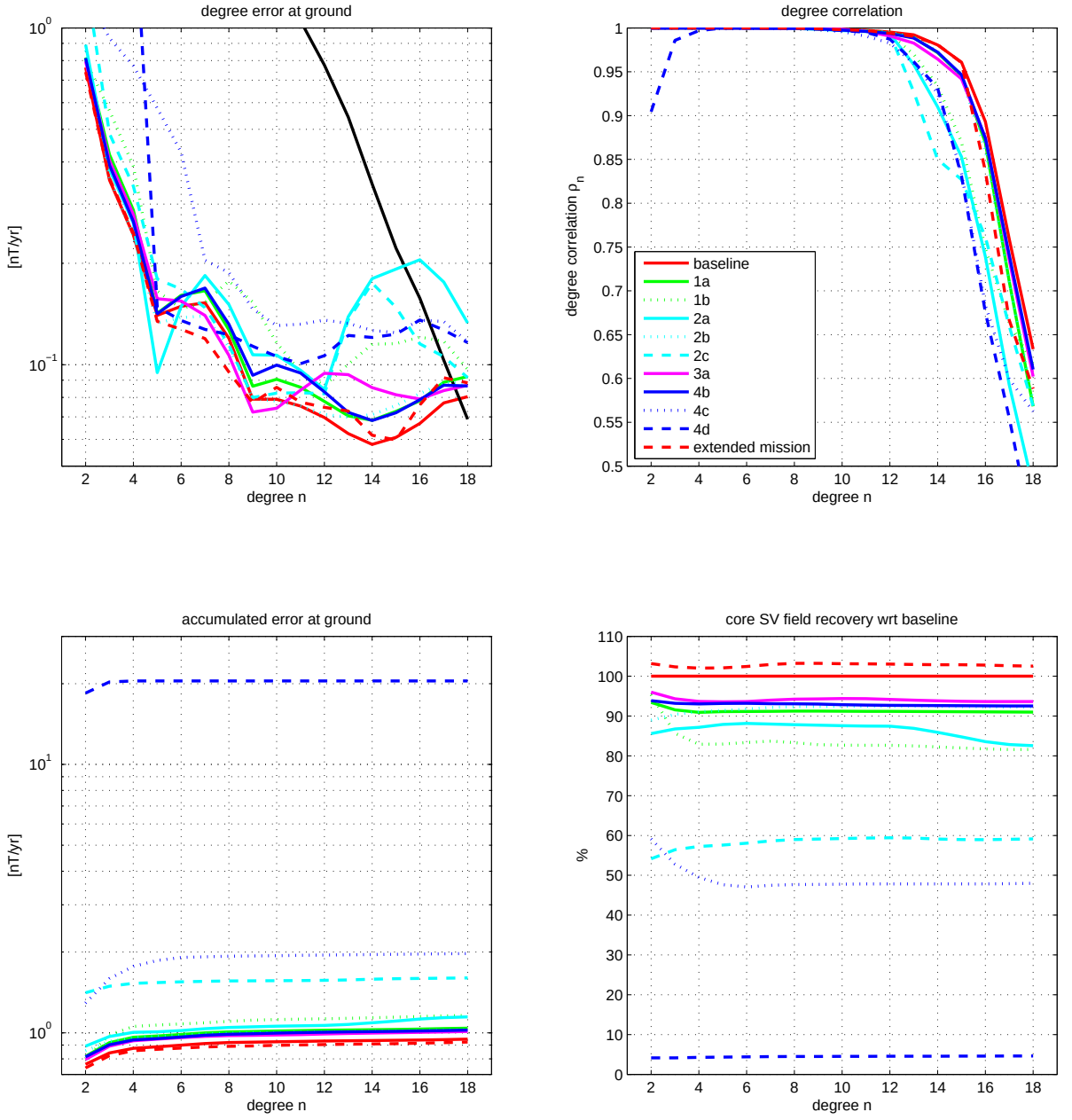

Figure 7.6: Top left: Degree error (at the Earth's surface) of the core field SV recovery for different satellite combinations and approaches. Black curve presents core SV signal as given by the synthetic model swarm(06a/04). Bottom right: degree correlation. Bottom left: accumulated error, i.e. the square root of the sum (from degree 2 to n) of the degree variances. Bottom right: Quality of recovered core field SV wrt. baseline.

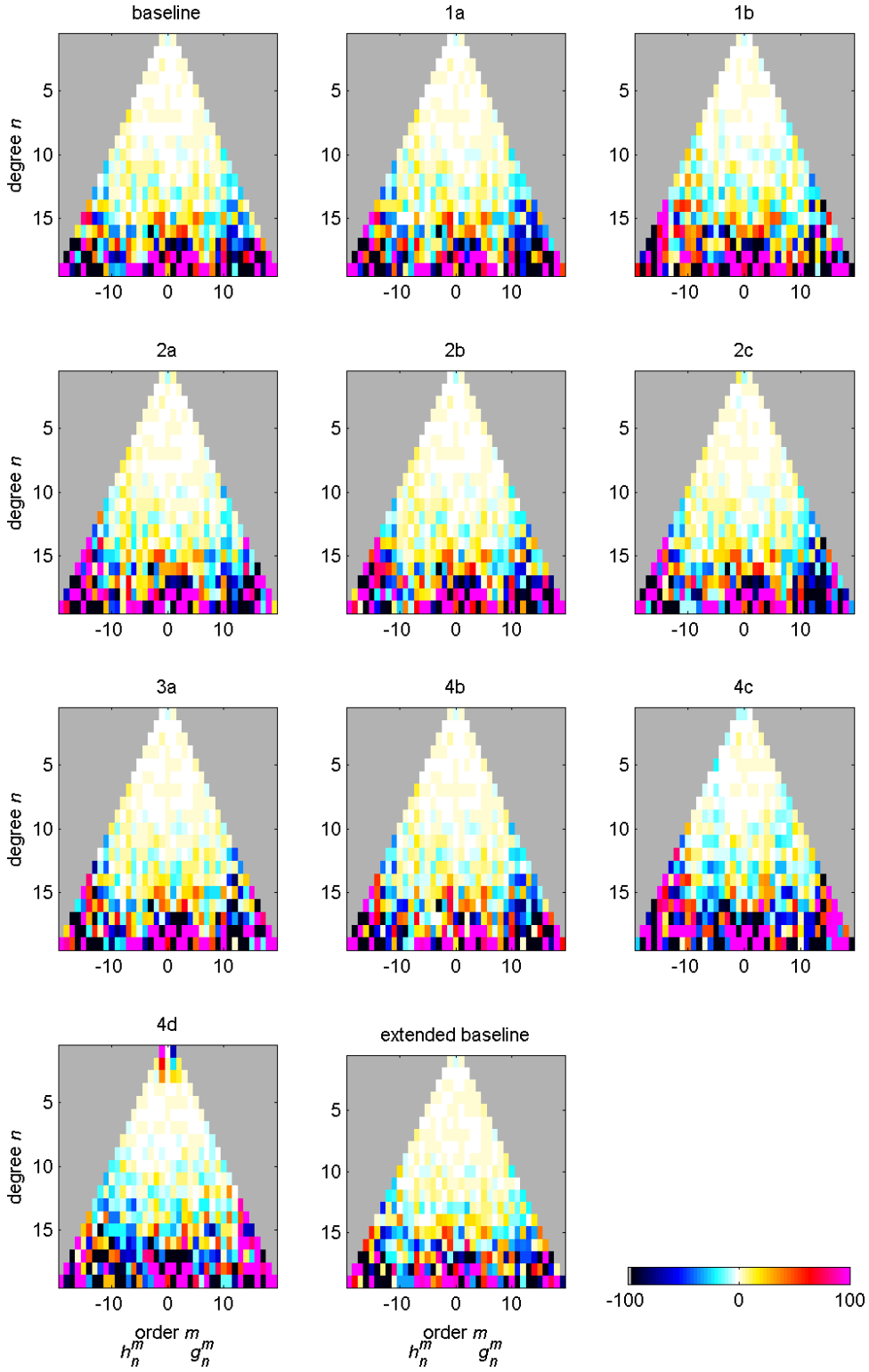

Figure 7.7: Sensitivity matrices for the core field secular variation recovery for Constellation 4 and the various failure cases.

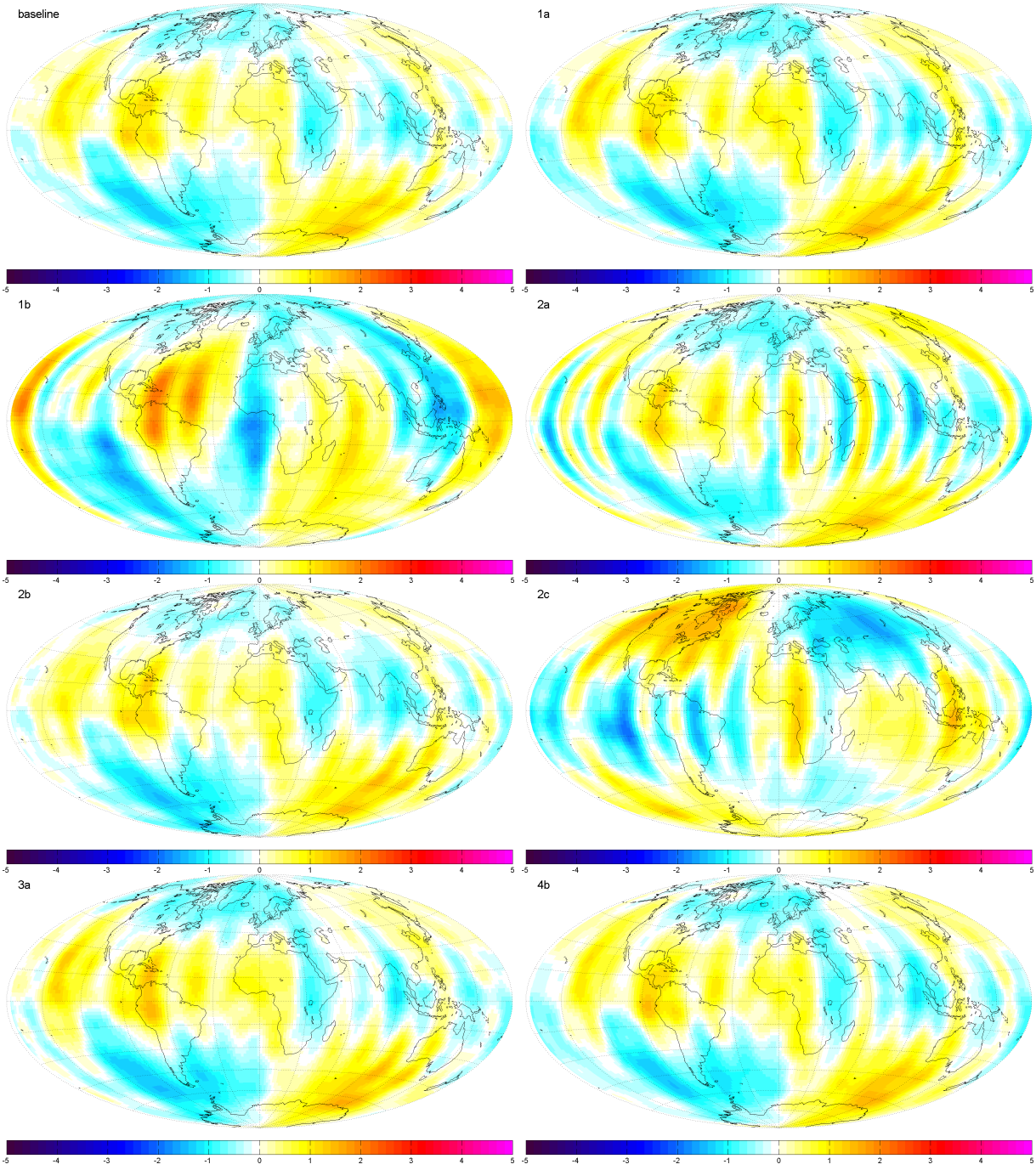

Figure 7.8: Secular variation field field difference maps in the B_r component (in nT/yr) at ground for the baseline configuration and Failure cases 1a to 4b.

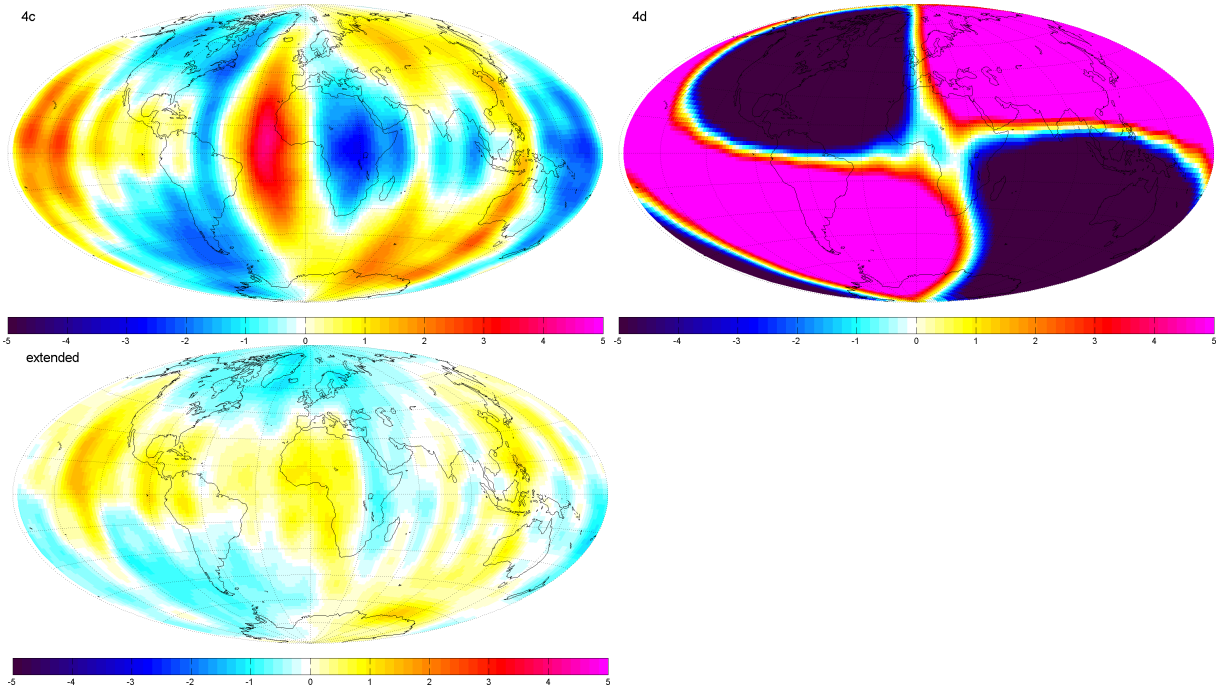

Figure 7.9: Secular variation field difference maps in the B_r component (in nT/yr) at ground for Failure case 4c and 4d and for the extended mission case.

	Swarm A			Swarm B			Swarm C		
	α	β	γ	α	β	γ	α	β	γ
1a	83.7910	87.2221	87.4751				84.9977	93.9317	96.0642
1b	32.4038	64.8373	60.1046	32.9193	65.1942	60.0949			
2a	56.7041	84.6423	19.0059	60.7728	92.7440	18.9002	52.7040	61.5484	26.0855
2b	86.3111	93.8772	92.3367	86.6979	93.6073	92.7925	91.3522	89.9761	92.4892
2c	83.6743	14.4850	77.2644	100.7019	37.2607	98.3037	87.7082	32.2696	82.0596
3a	16.9673	55.8565	68.4654	34.0597	56.8179	76.6334	57.2097	35.5028	75.2223
4b	89.3056	93.1919	91.6263				88.8595	95.0813	97.1611
4c	35.8843	58.1352	31.2619	36.5028	63.8942	31.7000			
4d	27.5861	69.6344	28.3295						
5a	29.8909	71.2940	29.4350	29.7579	70.5042	29.0649			
5b	101.2355	100.8244	101.3012	101.1424	100.7275	100.9470	100.8674	101.2569	102.1906

Table 7.2: Averaged quality factor of Euler angle recovery wrt. baseline for the various failure cases.

7.3.3 Assessment of Euler angle recovery

Figures 7.10 to 7.13 show the recovery of the Euler angles for the various failure cases and satellites. Euler angles are estimated in bins of 30 days length. Shown is the difference between true and recovered angles as a function of time. The values in parenthesis give mean value and standard deviation.

The quality of the Euler angle recovery is based on the standard deviation of the difference between recovered and true Euler angles (i.e. the second number in parenthesis shown in the figures). If σ_{baseline} is the standard deviation of the baseline, and σ_{x} is that of failure case x, then the quality factor (in %) is defined as

$$q^{\text{x}} = 100 \frac{\sigma_{\text{baseline}}}{\sigma_{\text{x}}}. \tag{7.4}$$

The larger q, the better the Euler angle recovery. q for the various failure cases and satellites are listed in Table 7.2. It is interesting to note that the recovery of the Euler angles in case of failure of one satellite is much better when the failing satellite is one of the lower pair (e.g. cases 1a and 4b) than when the failure corresponds to the higher satellite (e.g. cases 1b, 4c, and 4d).

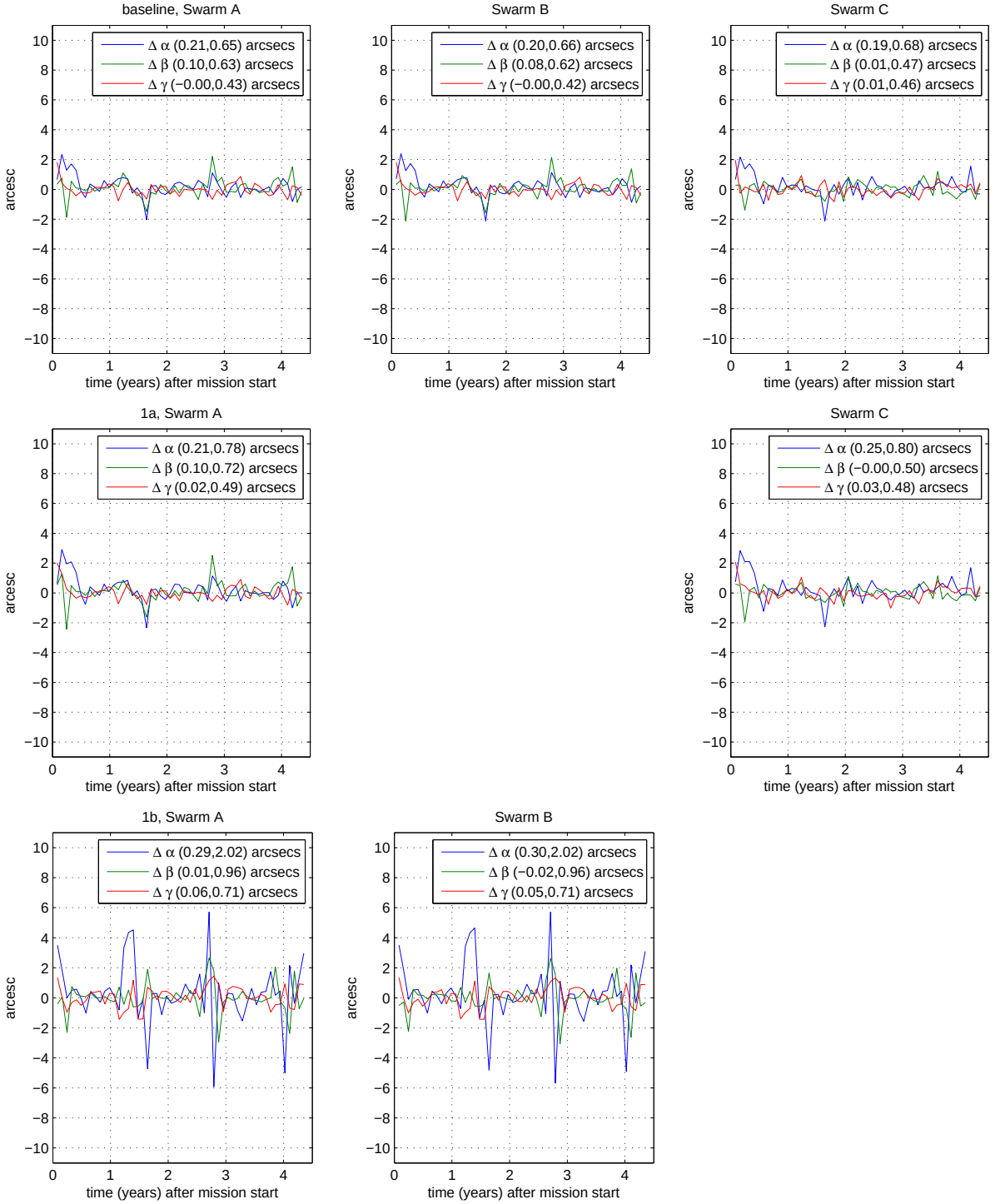

Figure 7.10: Recovery of the Euler angles for the various failure cases and satellites. Euler angles are estimated in bins of 30 days length. Shown is the difference between true and recovered angles as a function of time. The values in parenthesis give mean value and standard deviation.

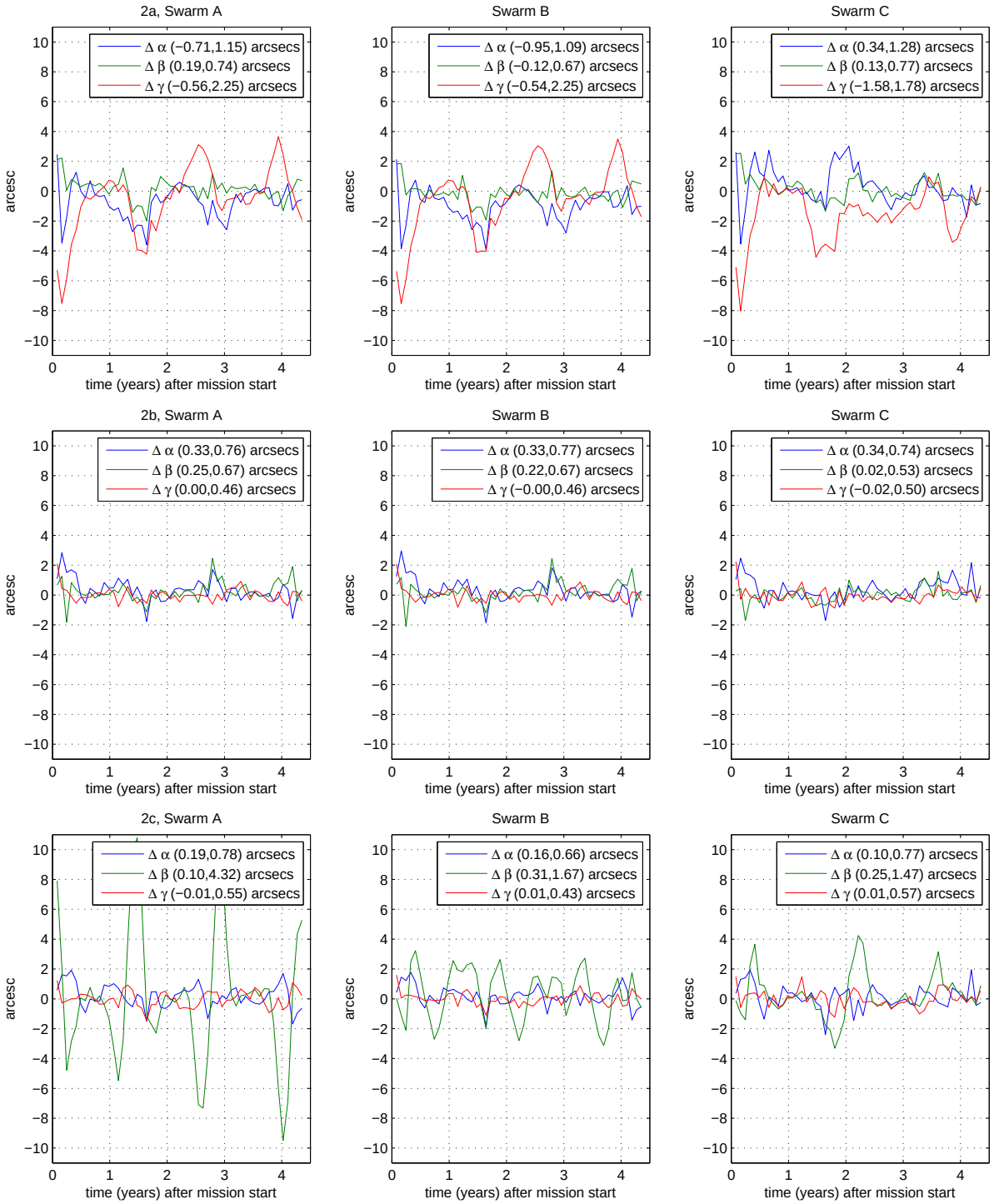

Figure 7.11: Fig. 7.10, continued.

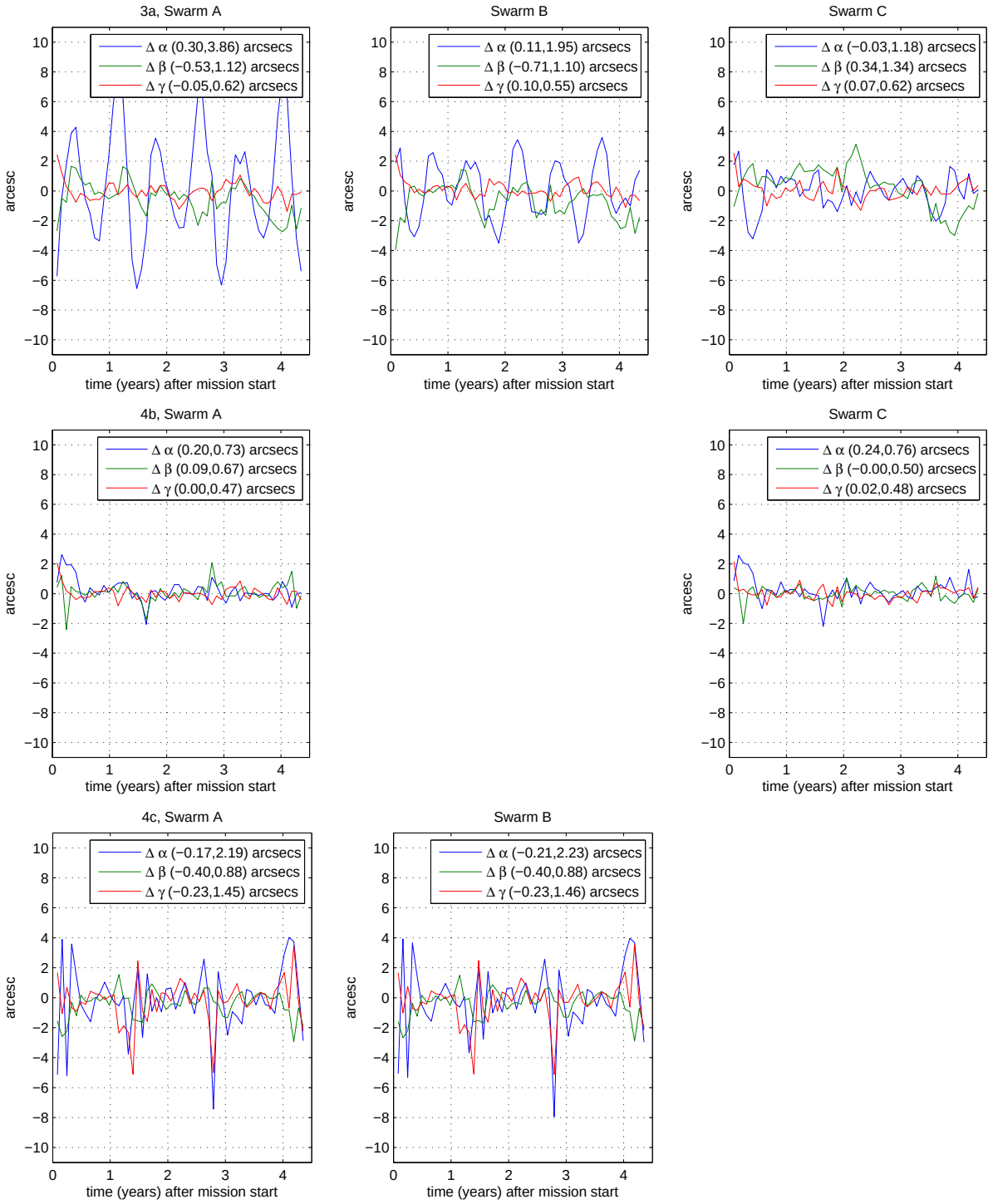

Figure 7.12: Fig. 7.10, continued.

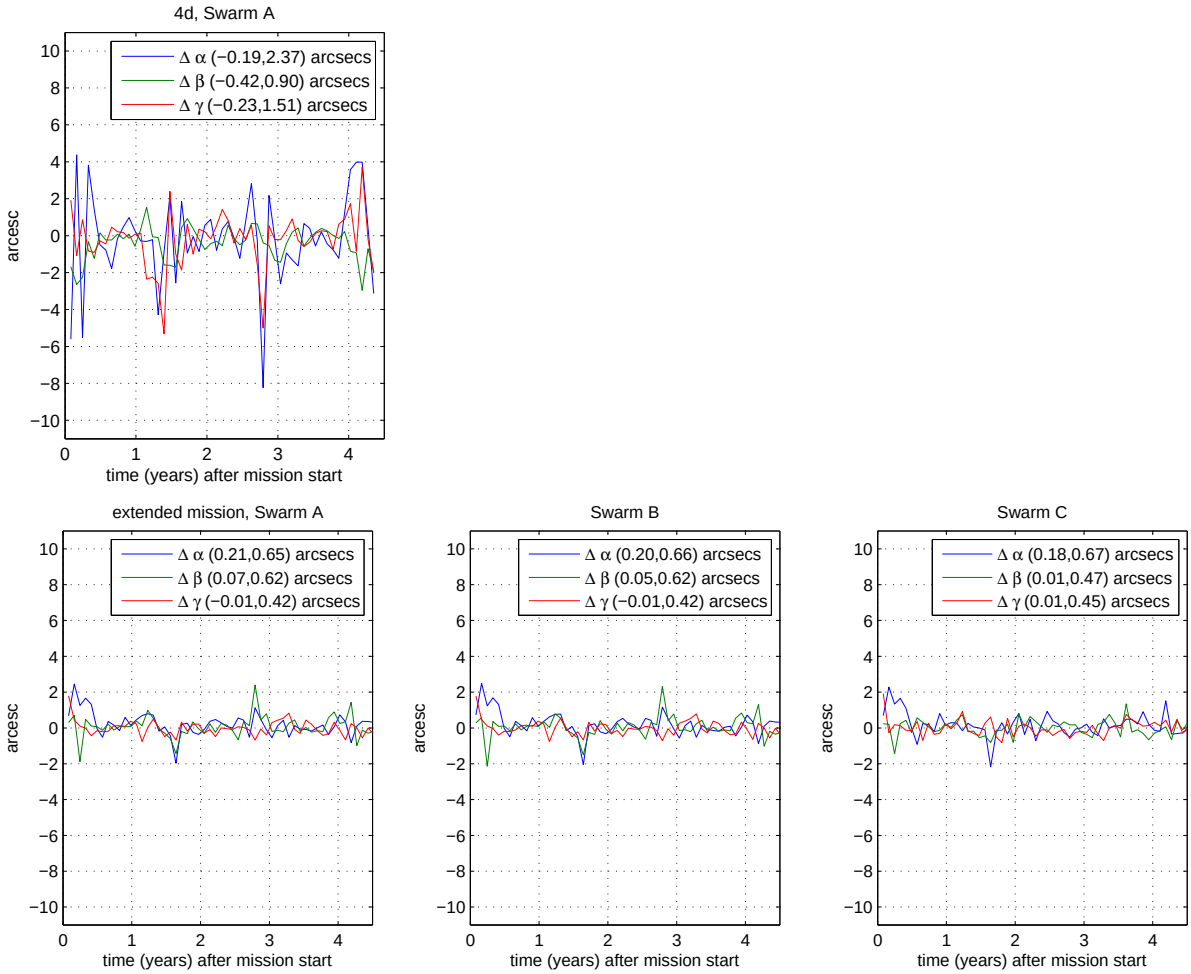

Figure 7.13: Fig. 7.10, continued.

7.3.4 Assessment of magnetospheric field recovery

Although the present study concentrates on an assessment of the crustal and core field recovery (which are two of the main science objectives of the *Swarm* mission), a brief assessment of magnetospheric field recovery will be given in following. A good recovery of time series of the magnetospheric field and its induced counterpart is necessary for determining 3-D mantle conductivity (which is the third main science objective of *Swarm*).

A strict assessment of magnetospheric field recovery as first step for 3-D mantle conductivity requires recovery of continues time series without data gaps, from which transfer functions and coherency between magnetospheric and induced fields *as a function of frequency* is determined. This is, however, not possible with the approach used in the present study, which is based in quiet time data (and thus the time series are rather discontinuous).

From such gappy time series it is not possible to determine the frequency dependence of coherence. However, an indication of time series recovery can be obtained by looking at the correlation coefficient (which is the mean coherency averaged over all periods). The correlation coefficient is, however, influenced by the probably rather low coherence at short periods (which are of less interest for recovery of mantle conductivity), and therefore one should not focus on the *absolute* value of the correlation (which can be rather low) but its *relative* size compared to the baseline recovery,

Following the approach used during Phase A of the mission and explained by Sabaka and Olsen [2006], we calculated the correlation coefficient ρ between the recovered and the true time series, for various primary (inducing) coefficients q_n^m, s_n^m and secondary (induced) coefficients a_n^m, b_n^m . The results are listed in Tables 7.3 to 7.5. A graphical presentation of the correlation angle $\xi = \arccos \rho$, where ρ is the correlation coefficient, is presented in Figures 7.14 to 7.16 for various parts of the mission lifetime. High correlation coefficients, corresponding to small correlation angles, are an indication of a good magnetospheric field recovery.

Compared to mission baseline, the various failure cases result in a more or less degraded performance. Most severe are failure cases 1a, 2c, 2b, 4c and 4b. Interesting is failure case 5a, which results in an *improved* recovery of the low-degree magnetospheric coefficients but considerably degraded high-degree coefficients, especially concerning the induced ones ($a_n^m, b_n^m, n, m > 1$). Since a proper recovery of these coefficients is essential for determination of 3D mantle conductivity, Failure case 5a will not be able to fulfill this science objective.

case	n	n	a_n^m	q_n^m	b_n^m	s_n^m
bl	1	0	0.470	0.999		
	1	1	0.208	0.890	0.208	0.804
	2	0	0.843	0.987		
	2	1	0.795	0.984	0.809	0.979
	2	2	0.148	–	0.219	–
	3	0	0.439	0.998		
	3	1	0.308	0.993	0.319	0.989
	3	2	0.147	–	0.234	–
	3	3	0.017	–	0.004	–
$1a$	1	0	0.375	0.998		
	1	1	0.114	0.660	0.095	0.517
	2	0	0.843	0.987		
	2	1	0.784	0.982	0.799	0.977
	2	2	0.141	–	0.207	–
	3	0	0.264	0.998		
	3	1	0.143	0.992	0.139	0.988
	3	2	0.068	–	0.114	–
	3	3	0.010	–	0.009	–
$1b$	1	0	0.409	0.998		
	1	1	0.104	0.793	0.109	0.654
	2	0	0.739	0.971		
	2	1	0.765	0.973	0.766	0.962
	2	2	0.102	–	0.170	–
	3	0	0.344	0.996		
	3	1	0.173	0.976	0.146	0.966
	3	2	0.113	–	0.099	–
	3	3	0.006	–	0.010	–
$2a$	1	0	0.383	0.998		
	1	1	0.093	0.651	0.094	0.492
	2	0	0.805	0.983		
	2	1	0.732	0.976	0.753	0.967
	2	2	0.095	–	0.166	–
	3	0	0.281	0.998		
	3	1	0.190	0.988	0.198	0.985
	3	2	0.091	–	0.163	–
	3	3	0.028	–	0.005	–

Table 7.3: Correlation coefficient between recovered and true time-series of magnetospheric and high-frequency induced coefficients, for the time period 1998.5 - 2003.

case	n	n	a_n^m	q_n^m	b_n^m	s_n^m
$2b$	1	0	0.455	0.999		
	1	1	0.172	0.860	0.181	0.761
	2	0	0.767	0.984		
	2	1	0.655	0.960	0.617	0.929
	2	2	0.137	–	0.199	–
	3	0	0.381	0.998		
	3	1	0.251	0.986	0.252	0.975
	3	2	0.139	–	0.172	–
	3	3	0.000	–	0.008	–
$2c$	1	0	0.427	0.999		
	1	1	0.147	0.775	0.112	0.627
	2	0	0.822	0.985		
	2	1	0.772	0.982	0.788	0.975
	2	2	0.145	–	0.218	–
	3	0	0.303	0.998		
	3	1	0.187	0.992	0.173	0.988
	3	2	0.093	–	0.156	–
	3	3	0.005	–	−0.005	–
$3a$	1	0	0.454	0.999		
	1	1	0.158	0.849	0.172	0.714
	2	0	0.833	0.985		
	2	1	0.773	0.981	0.772	0.972
	2	2	0.176	–	0.228	–
	3	0	0.391	0.998		
	3	1	0.266	0.991	0.261	0.986
	3	2	0.139	–	0.222	–
	3	3	0.023	–	0.008	–
$4b$	1	0	0.371	0.998		
	1	1	0.111	0.647	0.091	0.500
	2	0	0.822	0.986		
	2	1	0.733	0.975	0.746	0.967
	2	2	0.129	–	0.197	–
	3	0	0.255	0.998		
	3	1	0.139	0.990	0.140	0.986
	3	2	0.070	–	0.118	–
	3	3	0.012	–	0.008	–

Table 7.4: Correlation coefficient between recovered and true time-series of magnetospheric and high-frequency induced coefficients, for the time period 1998.5 - 2003.

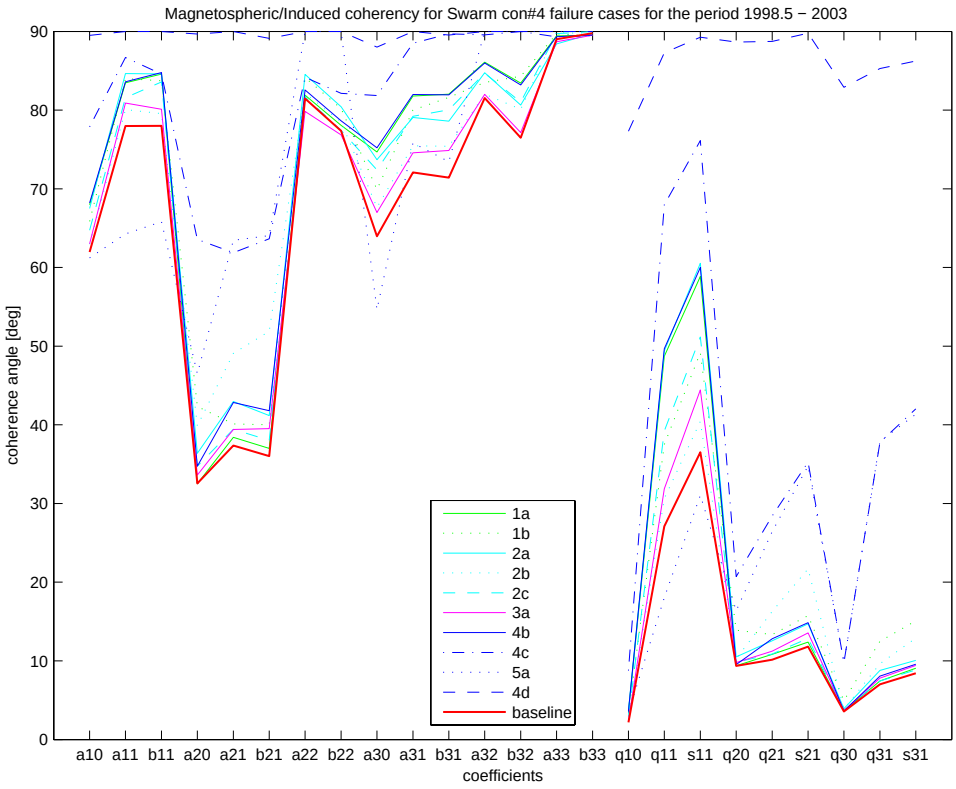

Figure 7.14: Coherency angles between the true and recovered magnetospheric and high-frequency induced time-series for the various cases, determined for the time span 1998.5 to 2003.

case	n	n	a_n^m	q_n^m	b_n^m	s_n^m
$4c$	1	0	0.210	0.988		
	1	1	0.058	0.375	0.095	0.240
	2	0	0.445	0.935		
	2	1	0.471	0.879	0.444	0.817
	2	2	0.102	–	0.137	–
	3	0	0.142	0.985		
	3	1	0.026	0.790	0.006	0.743
	3	2	0.008	–	−0.002	–
	3	3	0.012	–	0.009	–
$4d$	1	0	0.009	0.220		
	1	1	−0.004	0.047	−0.004	0.013
	2	0	0.006	0.023		
	2	1	−0.016	0.022	0.015	0.004
	2	2	–	–	–	–
	3	0	0.035	0.124		
	3	1	−0.013	0.082	0.008	0.066
	3	2	–	–	–	–
	3	3	–	–	–	–

Table 7.5: Correlation coefficient between recovered and true time-series of magnetospheric and high-frequency induced coefficients, for the time period 1998.5 - 2003.

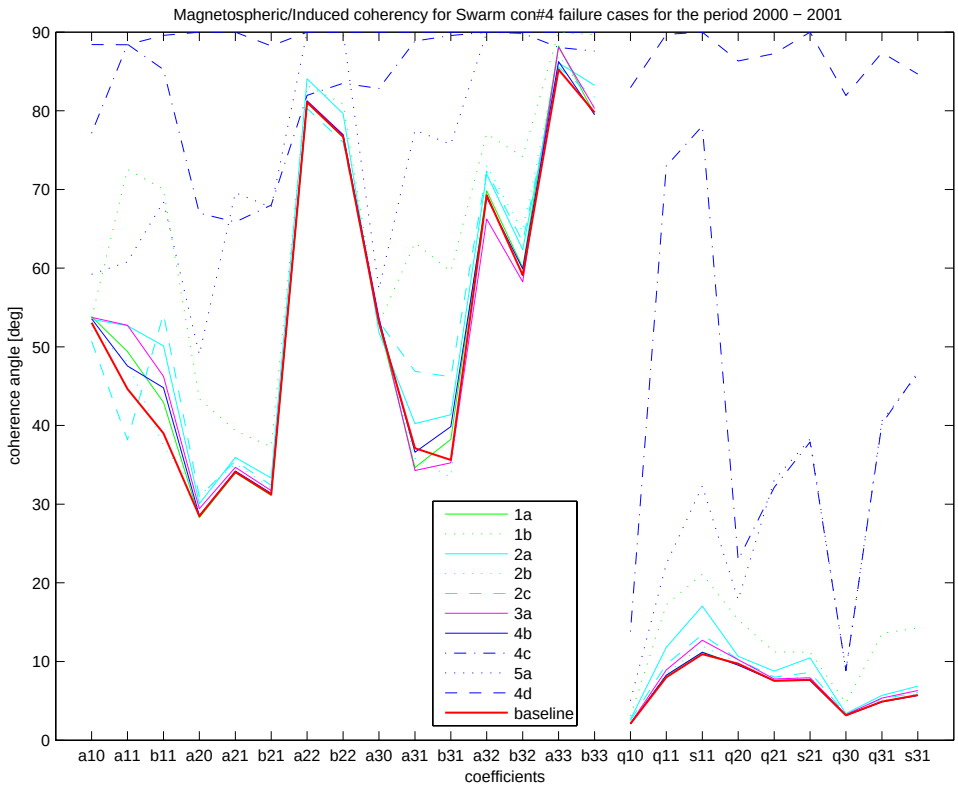

Figure 7.15: Similar to Fig. 7.14, but for the time span 2000 to 2001.

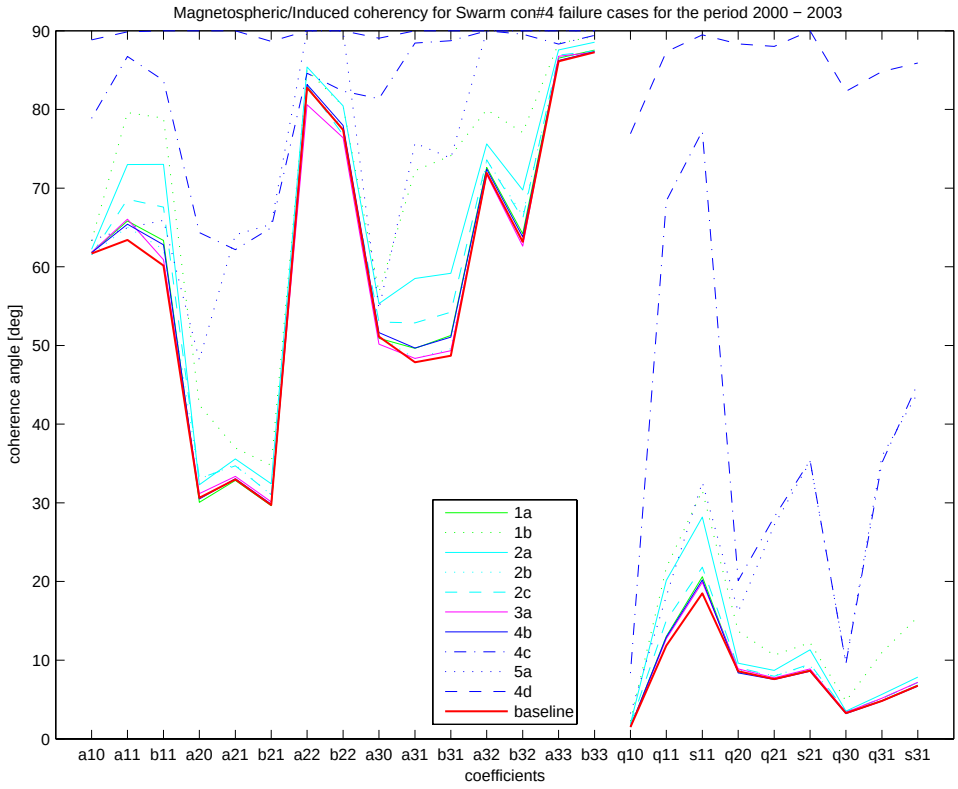

Figure 7.16: Similar to Fig. 7.14, but for the time span 2000 to 2003.

Chapter 8

Analysis of Residuals along Orbits

This section describes the development of algorithms for analysis of in-orbit magnetic field residuals between the synthetic input data and values obtained using Comprehensive Inversion (CI). Involved in this task are the working packages WP-3300 "Analysis of residuals along orbits" and WP-3400 "Sensitivity Analysis".

For the analysis of along-track residuals we looked at the following quantities:

- time series of the residuals;
- statistical parameters like mean, median, standard deviation, MAD (mean absolute deviation) and skewness, and their dependency in space (maps) and time (time series);
- normal distribution plots

8.1 Test quantities applied to the mission baseline simulation

In following we will present and discuss these quantities based on an analysis of the residuals of the baseline mission configuration of constellation #4.

The residuals are defined as the difference between the synthetic data and the predictions of the model, including all sources and applying the *estimated* Euler angles.

Figure 8.1 shows maps of median (left panels) and standard deviation (right panels) for the three components δB_r (top), ΔB_θ (middle) and ΔB_ϕ (bottom). These maps have been constructed by binning the data in cells of 10° latitude times 30° longitude.

These maps show that there is little dependence on (dipole) longitude, and therefore in following we binned the data according to dipole co-latitude θ_d only. The result is shown in Figure 8.2, both for the residuals $(\Delta B_r, \Delta B_\theta, \Delta B_\phi)$ in the NEC frame (top panels) and for the residuals $(\Delta B_1, \Delta B_2, \Delta B_3)$ in the VFM frame.

Panel 1 (resp. 4) shows the arithmetic mean

$$\overline{x} = \frac{1}{N}\sum_{i=1}^{N} x_i \tag{8.1}$$

(solid line) and the median (dashed line), as two examples for estimates of the location parameter of a simple distribution. Especially at polar latitudes these two estimates differ considerably, which indicates that the sample distribution might be non-symmetric.

Panel 2 (resp. 5) shows standard deviation

$$s = \sqrt{\frac{1}{N-1}\sum_{i=1}^{N}(x_i - \overline{x})^2} \tag{8.2}$$

(solid line) and *Mean absolute deviation (MAD)*

$$MAD = \frac{1}{N}\sum_{i=1}^{N}|x_i - \overline{x}| \tag{8.3}$$

(dashed line) as two estimates of the dispersion parameter. If the data were Gaussian distributed, $1.3 \cdot MAD$ is a robust estimate of σ (the dispersion parameter of the Gaussian distribution).

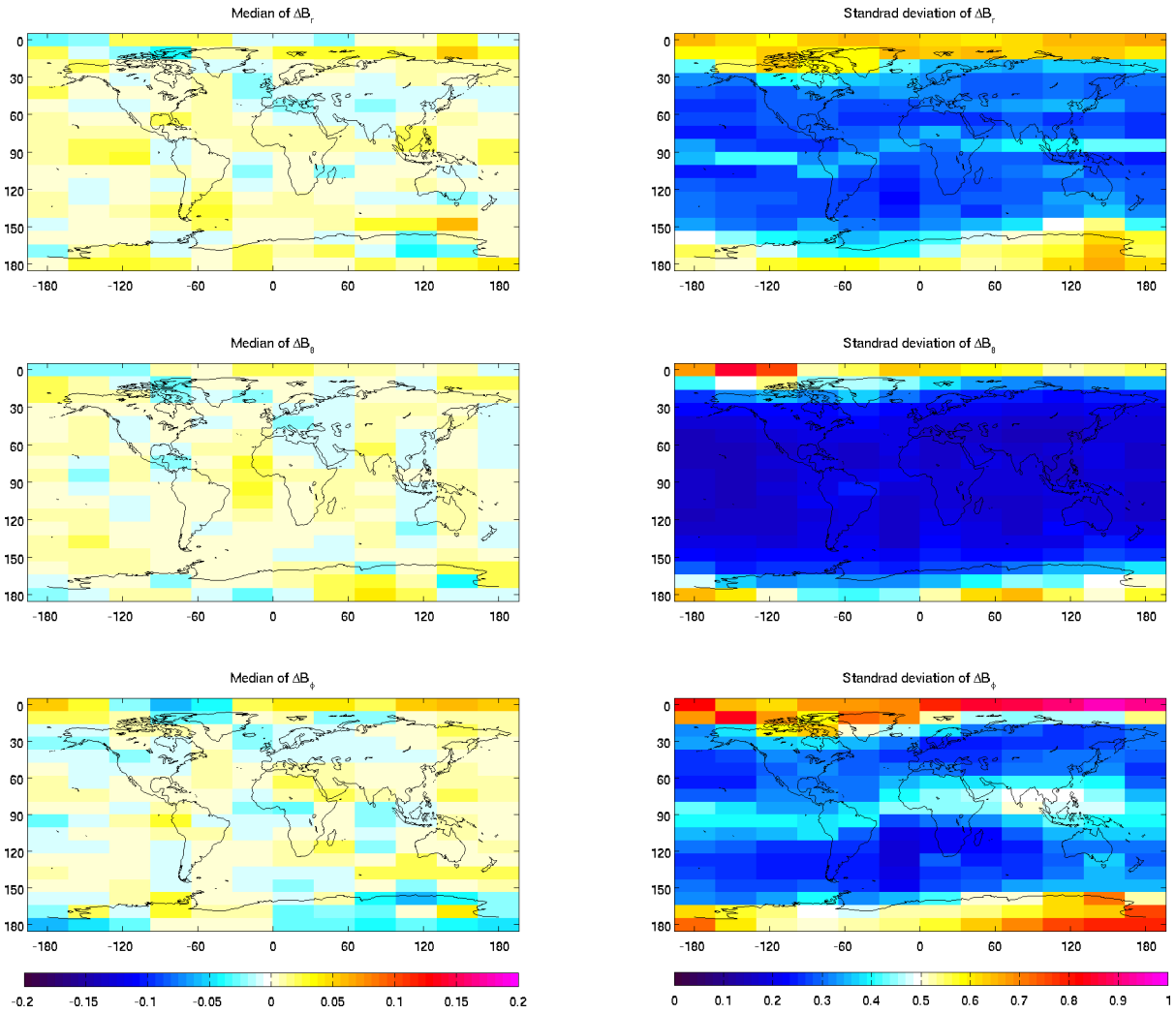

Figure 8.1: Maps of median (left) and standard deviation (right), in nT, of the residuals of the mission baseline.

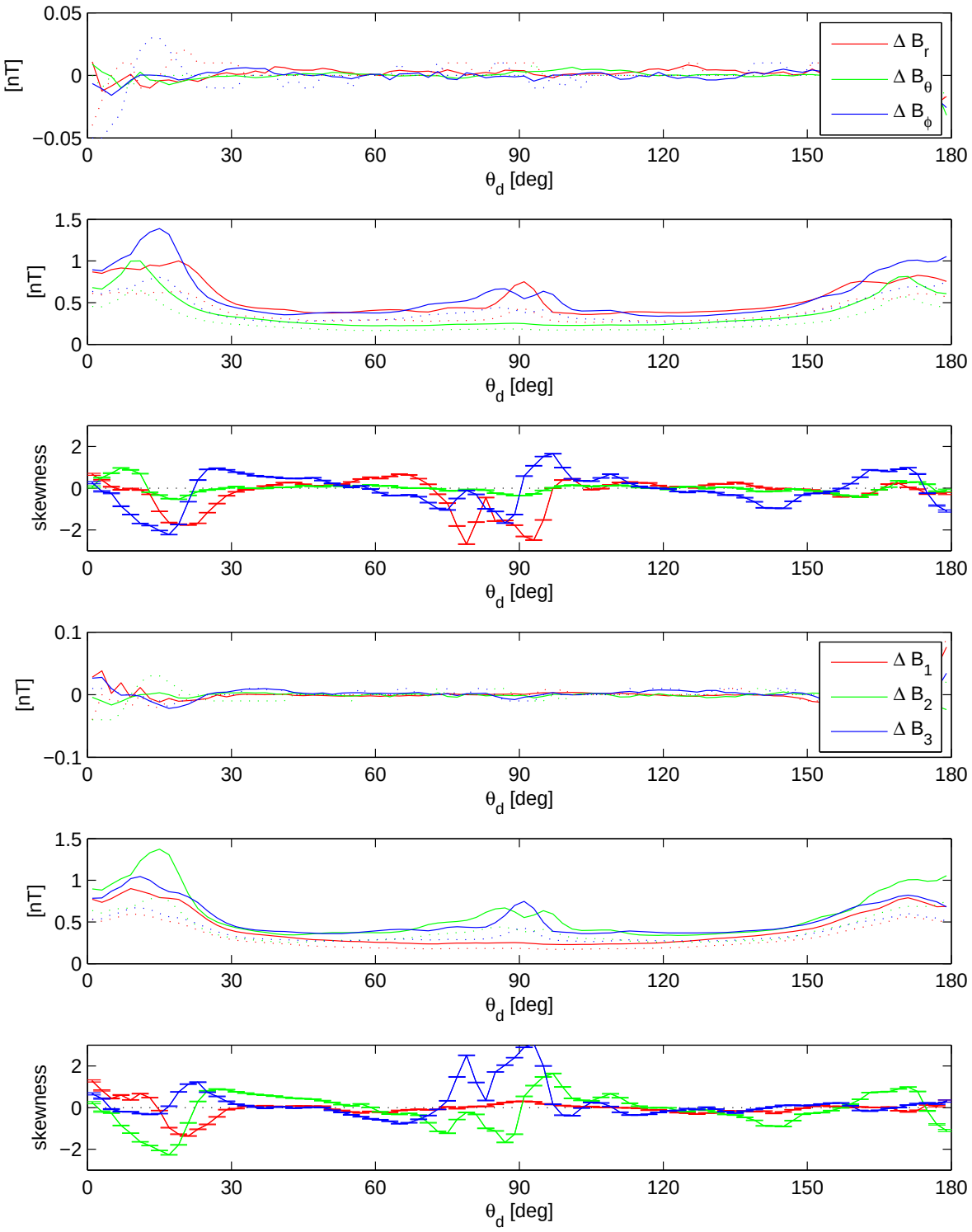

Figure 8.2: Top 3 panels: Mean (solid curve) and median (dashed), standard deviation (solid) and MAD (dashed) , and skewness, of the residuals of the mission baseline in the NEC frame, in dependence on dipole co-latitude θ_d. Bottom 3 panels: Similar, but residuals in the VFM frame.

Finally, panel 3 (resp. 6) shows the skewness

$$skew = \frac{1}{s^3}\frac{1}{N}\sum_{i=1}^{N}(x_i - \overline{x})^3 \tag{8.4}$$

is a measure of the asymmetry of the data around the sample mean. If skewness is negative, the data are spread out more to the left of the mean than to the right. If skewness is positive, the data are spread out more to the right. The skewness of the normal distribution (or any perfectly symmetric distribution) is zero. For the idealized case of a Gaussian distribution, the standard deviation of the skewness estimate is approximately $\sqrt{15/N}$ [Press et al., 1992]. The skewness shown in Figure 8.2 have been derived using typically $N \approx 25,000$ data points, and therefore skewness values which are considerably larger than ± 0.025 indicate an underlying asymmetric distribution. In the here considered case skewness is as large as ± 2, which indicates a highly asymmetric distribution.

This is confirmed by the normal probability plots of the residuals in the NEC frame shown in Figure 8.3. A normal probability plot indicates whether the data could come from a Gaussian (normal) distribution. If the data are Gaussian distributed the plot will be linear. Other distribution types will introduce curvature in the plot.

The shape of the residual distribution of the synthetic data analyzed in this study is rather similar to that obtained from real data. Figure 8.4 presents *cumulative density function (cdf)* plots of normalized residuals, $\varepsilon = x/s$, for the spherical vector components and polar scalar component of the CHAMP magnetometer data versus the CHAOS magnetic field model of Olsen et al. [2006]. It is clearly seen that the normalized residuals do not follow a Gaussian distribution, indicated by the straight dotted line. The actual distributions are closer to a Huber distribution (Gaussian distribution in the center, Laplacian distribution in the tail, cf. Holland and Welsch [1977], Constable [1988]) thus confirming the use of IRLS with Huber weights, which has been used for deriving the CHAOS model.

Finally, Figure 8.5 shows time series of the residuals as a function of time, in dependence on dipole co-latitude θ_d.

The distribution of the residuals for the other two satellites, *Swarm B* and *C*, are (for the baseline case) rather similar to that for *Swarm A*. There is, however, a strong correlation between the residuals of *Swarm A* and *B*, as expected, and therefore it is interesting to look at the distribution of the residual difference *A*-*B*. These are show in Figures 8.6 to 8.8. The unmodeled signal seen for instance in Figure 8.5 near year 1999.5 or 2001.5 at polar latitudes are much reduced in the difference *Swarm A*-*B*, and also the Normal probability plots show significantly decreased variances at all latitudes.

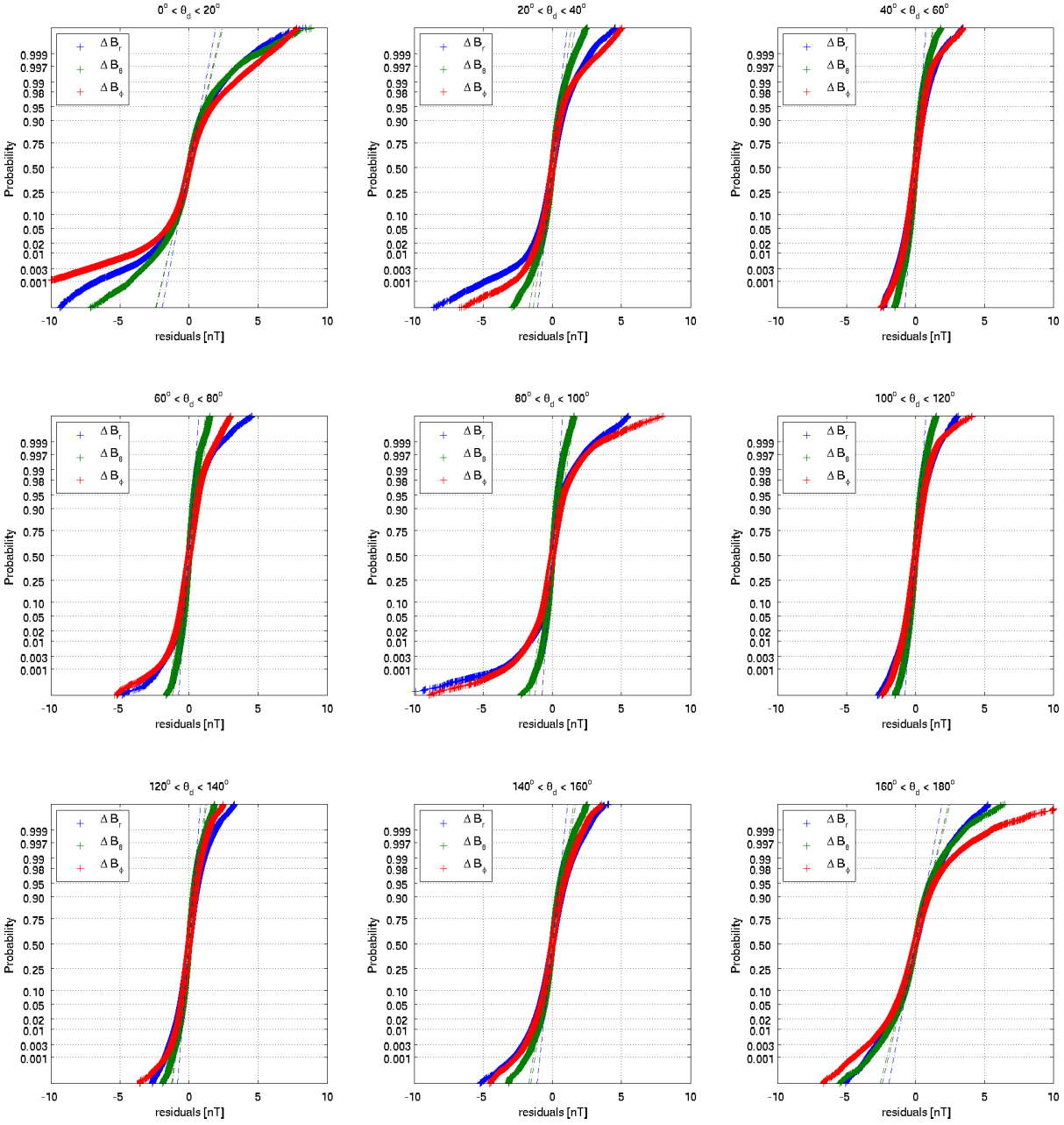

Figure 8.3: Normal probability plot of the residuals in the NEC frame, for different values of dipole latitude θ_d.

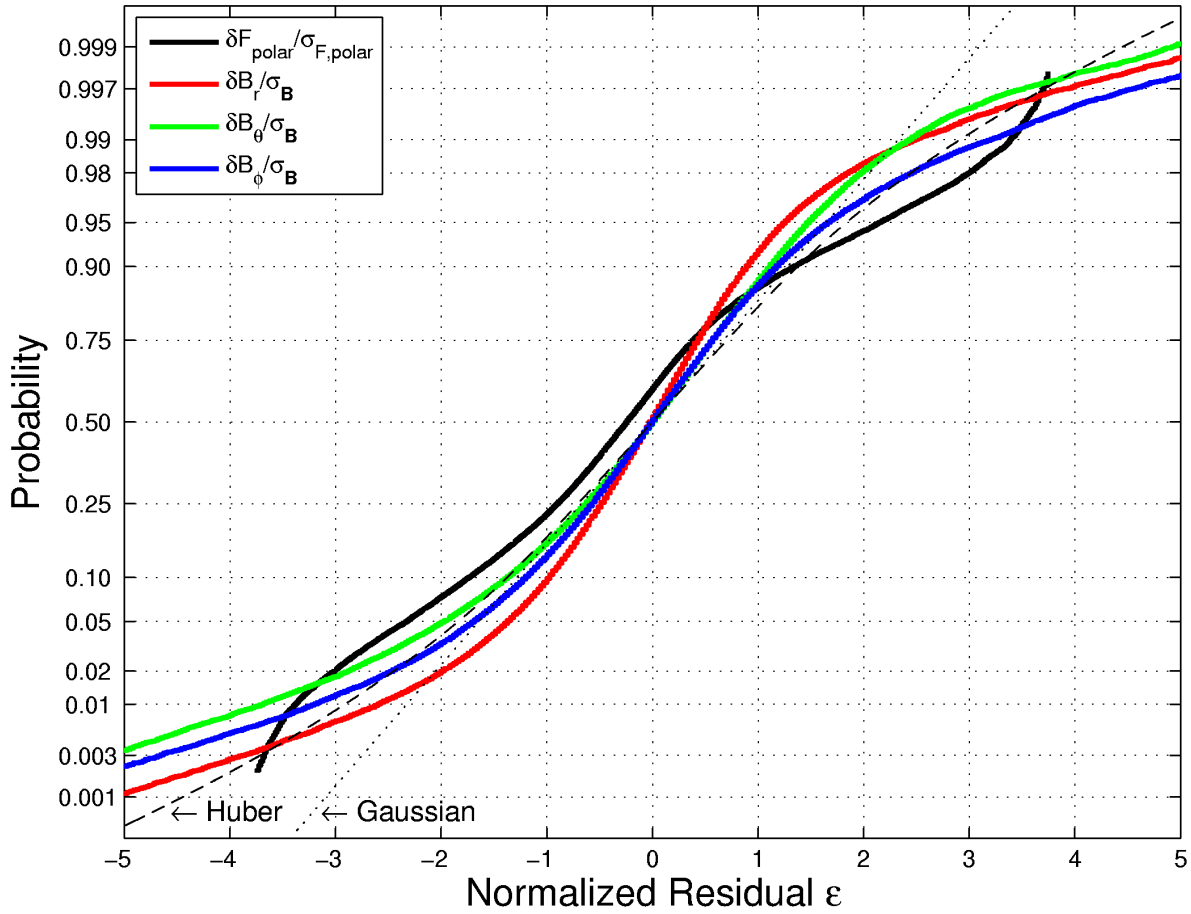

Figure 8.4: Cumulative density functions (cdfs) of normalized residuals, ε, for the spherical vector components and polar scalar component of the CHAMP magnetometer data versus the CHAOS magnetic field model of Olsen et al. [2006]. Theoretical curves for standardized Gaussian (dotted line) and Huber (with cut-off $c = 1.5$, dashed line) cdfs are also shown.

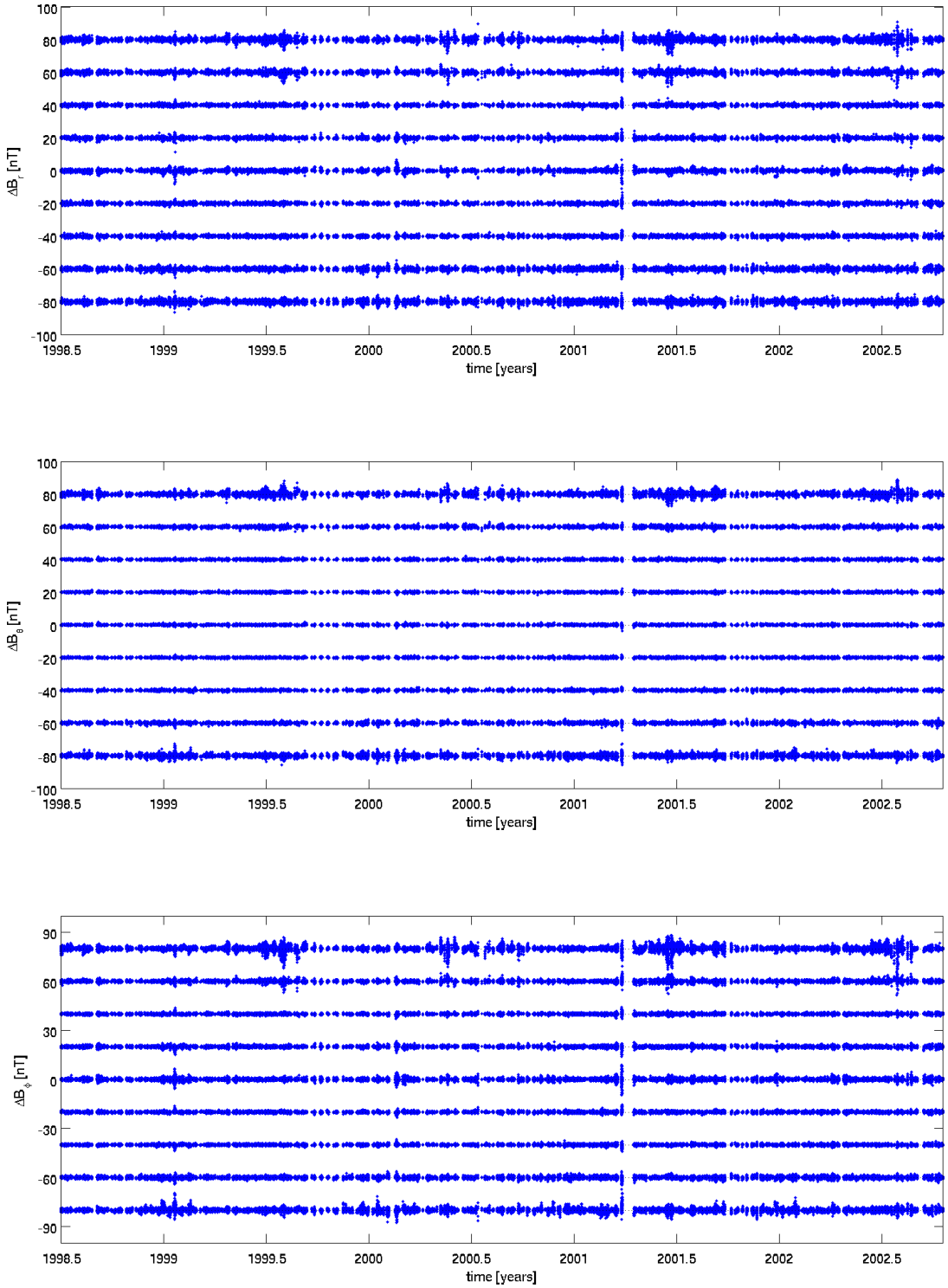

Figure 8.5: Time series of the residuals in the NEC frame, for different values of dipole latitude θ_d. As an example, the values centered at 80 nT are for dipole latitudes between +70° and +90°, with an offset of 80 nT (the black dotted line) added (i.e. 80 nT corresponds to 0 nT residuals).

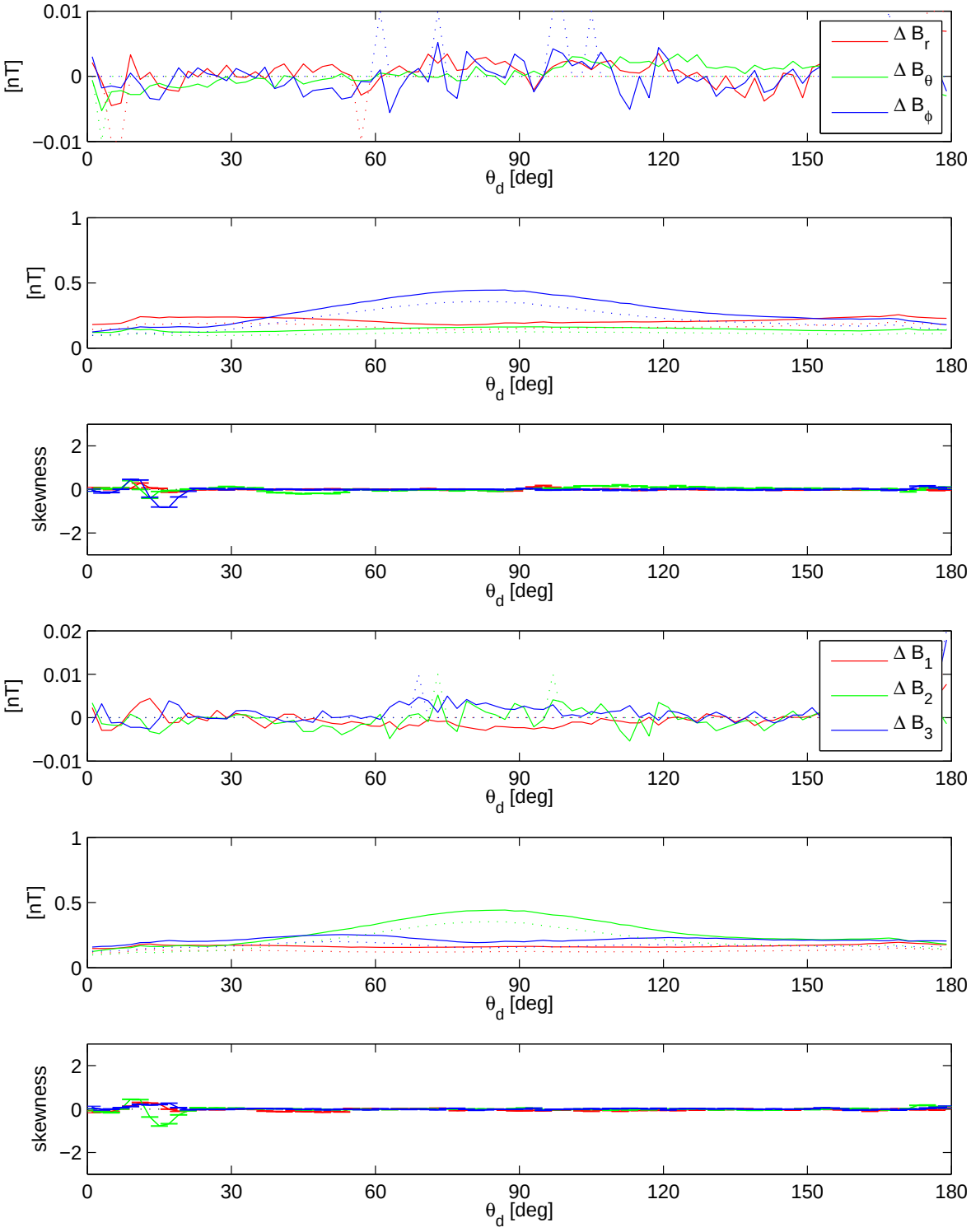

Figure 8.6: Similar to Fig. 8.2, but for the difference of the residuals of *Swarm A - B*.

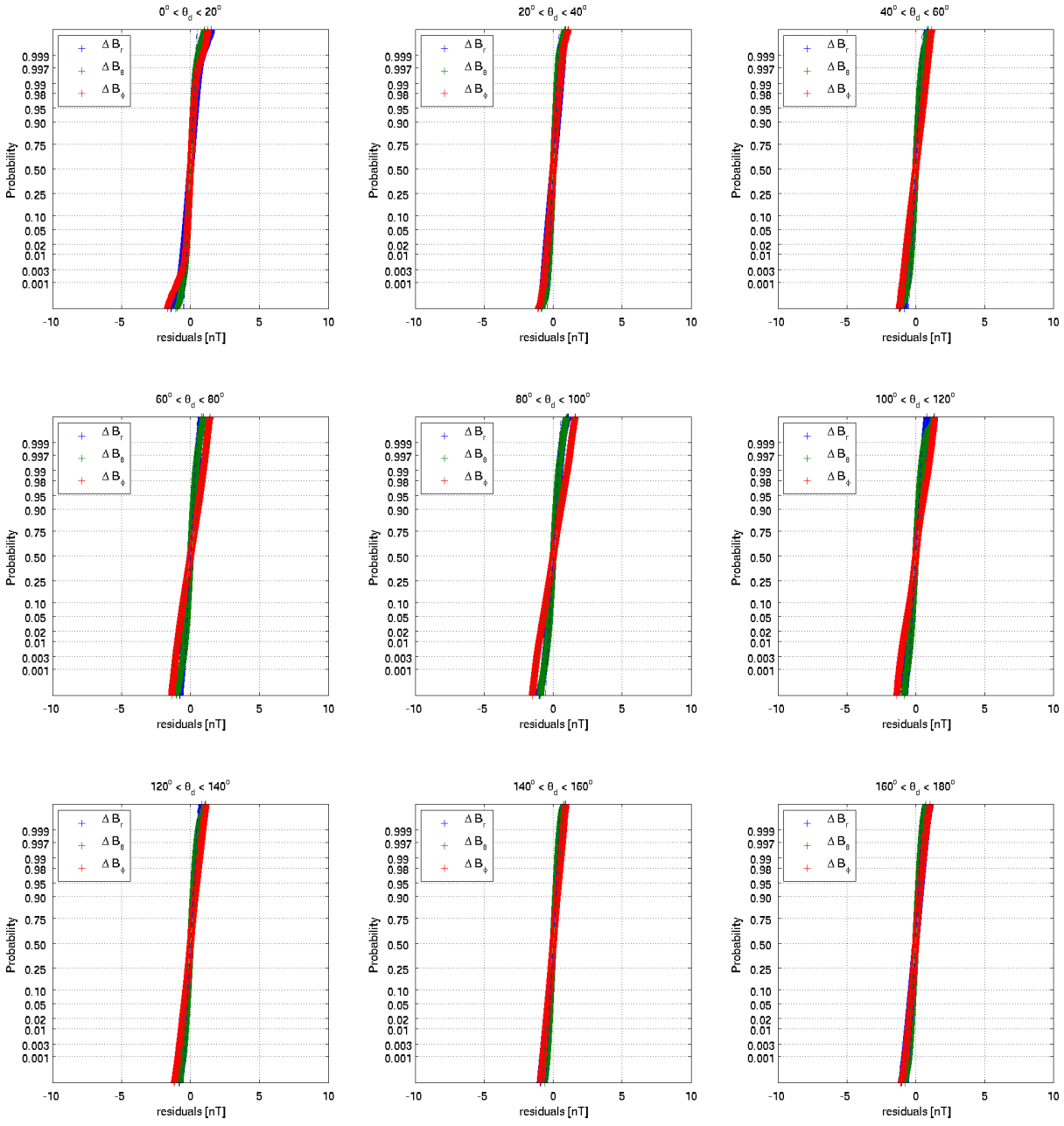

Figure 8.7: Similar to Fig. 8.3, but for the difference of the residuals of *Swarm A - B*.

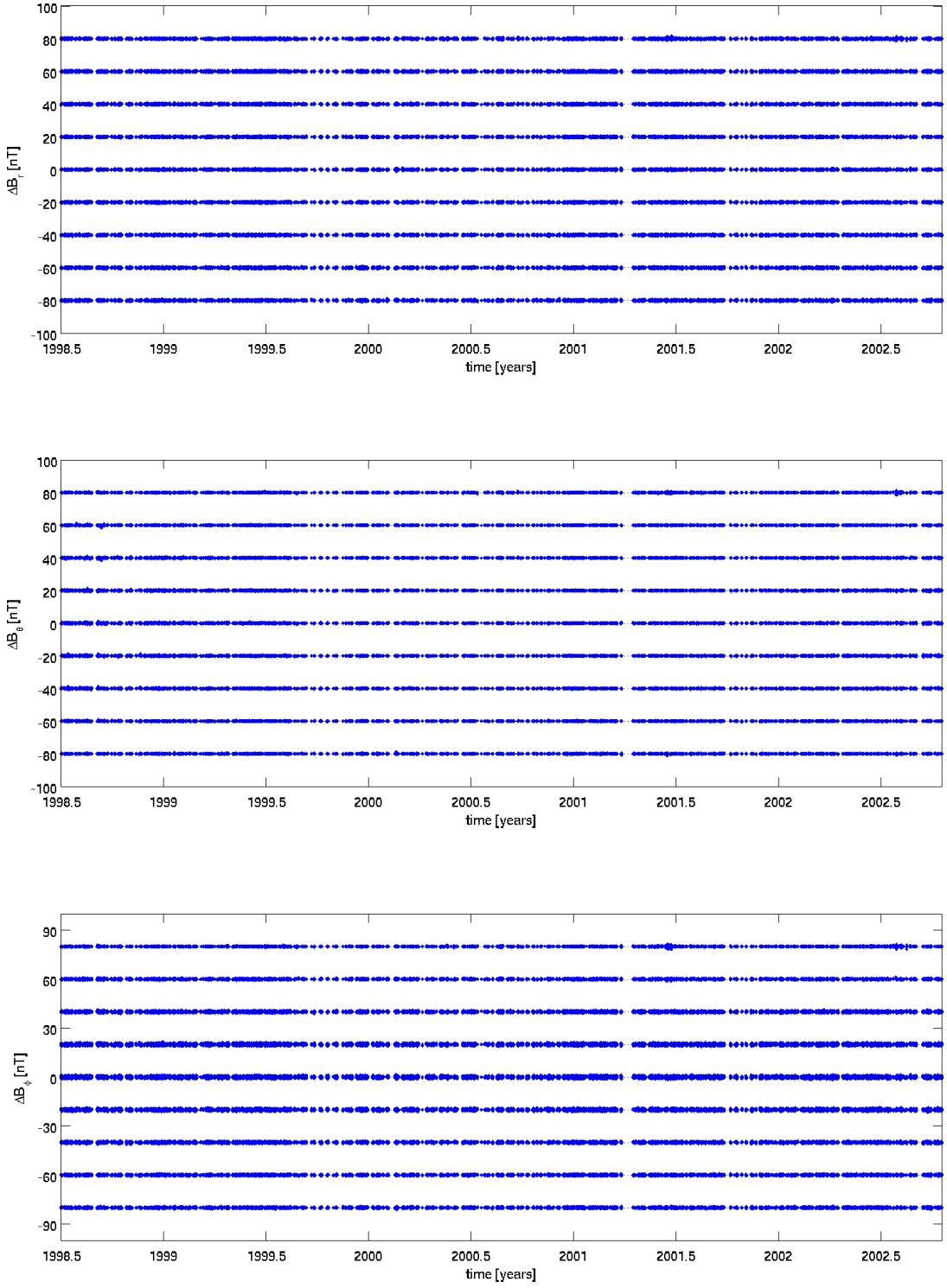

Figure 8.8: Similar to Fig. 8.5, but for the difference of the residuals of *Swarm A - B*.

8.2 Application to some failure cases

Mean values (residual median) for some selected failure cases are listed in Table 8.1, calculated in the NEC frame (top) and the VFM frame (bottom). Most interesting are the results for failure case 2a and 2b. While the median is almost zero when looking at the residuals in the NEC frame, the values in the VFM frame indicate an instrumental effect. The residuals are largest for *Swarm A* (the satellite for which the input data have been disturbed), but also affects *Swarm B*. Interestingly, the difference *Swarm A*-*B* yields $\overline{\Delta B_x} = 1.35$ nT, $\overline{\Delta B_y} \approx 0$ nT, $\overline{\Delta B_z} = 1.50$ nT, in good agreement with static magnetic bias $\mathbf{b}_{2a} = (b_x, b_y, b_z) = \frac{2}{\sqrt{2}}(1, 0, 1)$ nT that has been added to the data of *Swarm A*. A multi-satellite calibration of the VFM magnetometer will probably allow for solving the problem.

In summary it can be concluded that the developed approaches for statistical analysis of in-orbit residuals have proven to be a useful diagnostic tool.

	case	*Swarm A*			*Swarm B*			*Swarm C*		
		$\overline{\Delta B_r}$	$\overline{\Delta B_\theta}$	$\overline{\Delta B_\phi}$	$\overline{\Delta B_r}$	$\overline{\Delta B_\theta}$	$\overline{\Delta B_\phi}$	$\overline{\Delta B_r}$	$\overline{\Delta B_\theta}$	$\overline{\Delta B_\phi}$
NEC	bl	0.0000	0.0000	0.0000	0.0000	0.0000	0.0000	0.0000	0.0000	0.0000
	2a	0.0900	-0.0800	-0.0100	-0.0400	0.0300	0.0000	-0.0200	0.0100	0.0000
	2b	0.6100	0.0000	-0.0700	-0.4000	0.0000	0.0400	-0.2100	0.0000	-0.0100
	2c	0.0100	-0.0100	0.0000	-0.0100	0.0000	0.0000	0.0000	0.0000	0.0000
	3a	0.0200	0.0000	-0.1900	-0.0100	0.0100	0.1800	-0.0100	-0.0100	0.0000
		$\overline{\Delta B_x}$	$\overline{\Delta B_y}$	$\overline{\Delta B_z}$	$\overline{\Delta B_x}$	$\overline{\Delta B_y}$	$\overline{\Delta B_z}$	$\overline{\Delta B_x}$	$\overline{\Delta B_y}$	$\overline{\Delta B_z}$
VFM	bl	0.0000	0.0000	0.0000	0.0000	0.0000	0.0000	0.0000	0.0000	0.0000
	2a	0.7200	0.0000	0.8700	-0.6300	0.0100	-0.5300	-0.0300	0.0000	-0.0400
	2b	0.0200	-0.0500	0.0000	-0.0100	0.0300	0.0000	-0.0100	-0.0100	0.0000
	2c	0.0100	0.0000	0.0100	-0.0100	0.0000	-0.0100	0.0000	0.0000	0.0000
	3a	0.0000	-0.1600	0.0000	0.0100	0.1500	0.0000	0.0000	-0.0100	0.0000

Table 8.1: Residuals median for selected failure cases, in nT.

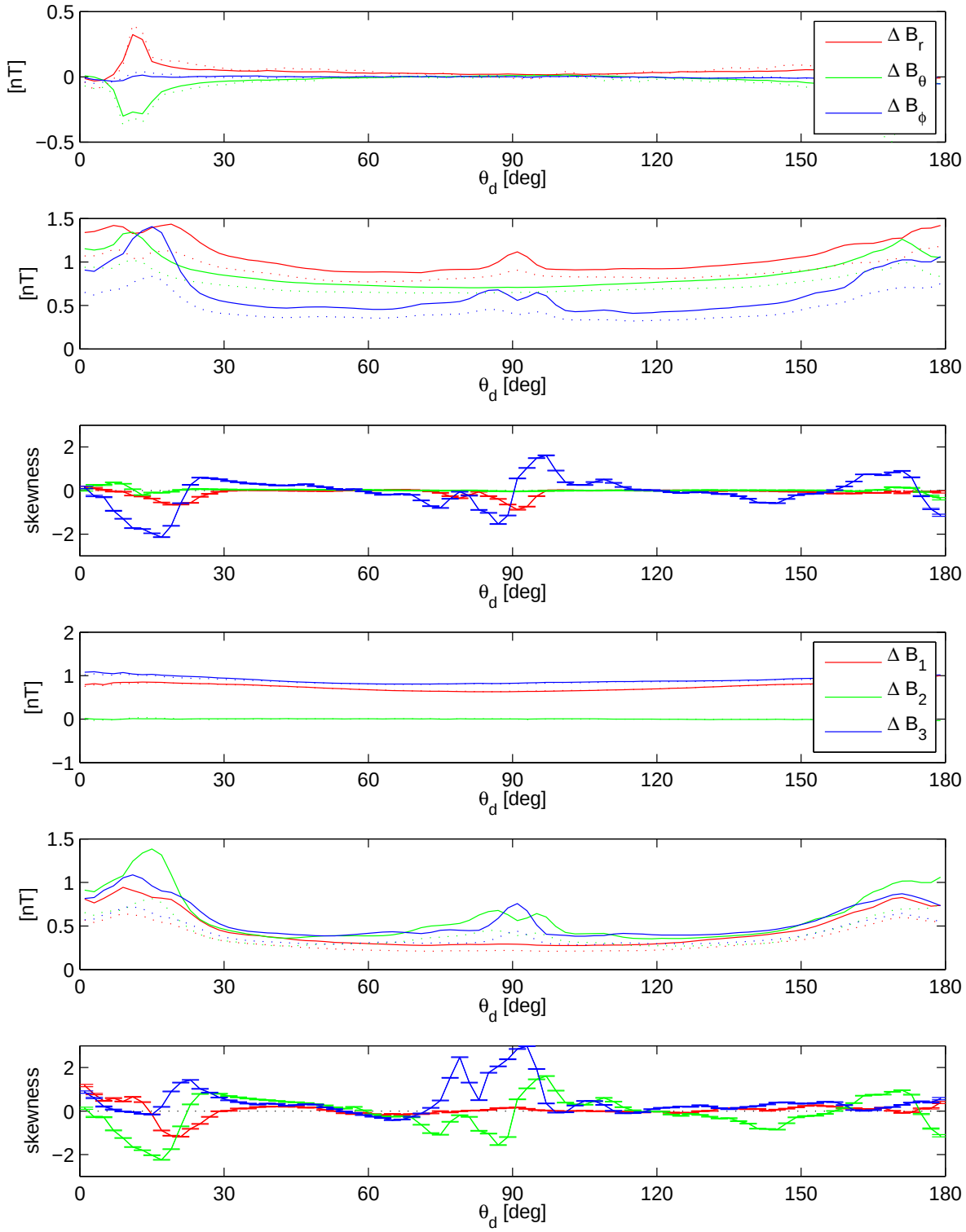

Figure 8.9: Top 3 panels: Mean (solid curve) and median (dashed), standard deviation (solid) and MAD (dashed), and skewness, of the residuals of failure case 2a in the NEC frame, in dependence on dipole co-latitude θ_d. Bottom 3 panels: Similar, but residuals in the VFM frame.

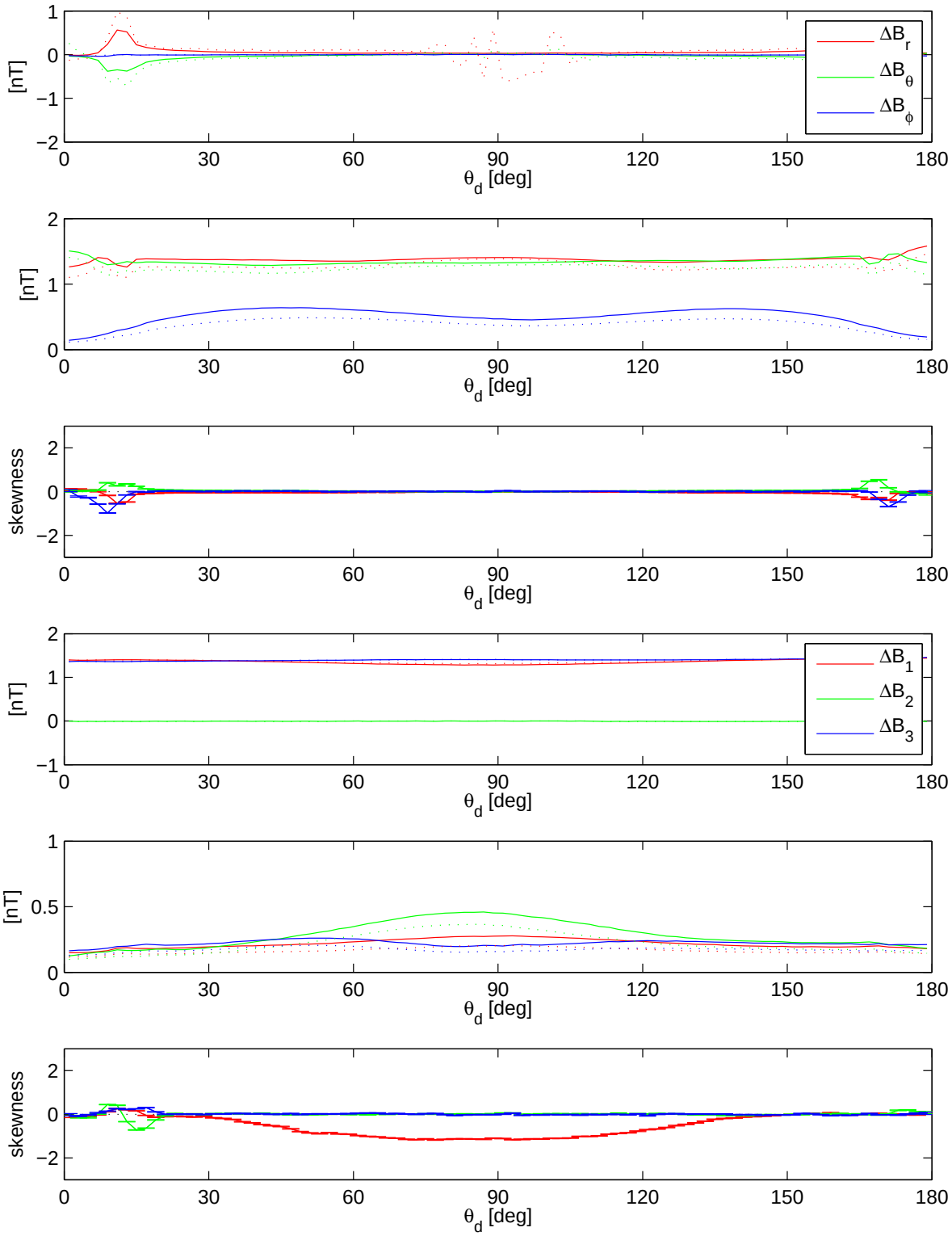

Figure 8.10: Similar to Fig. 8.9, but for the difference of the residuals of *Swarm A - B*.

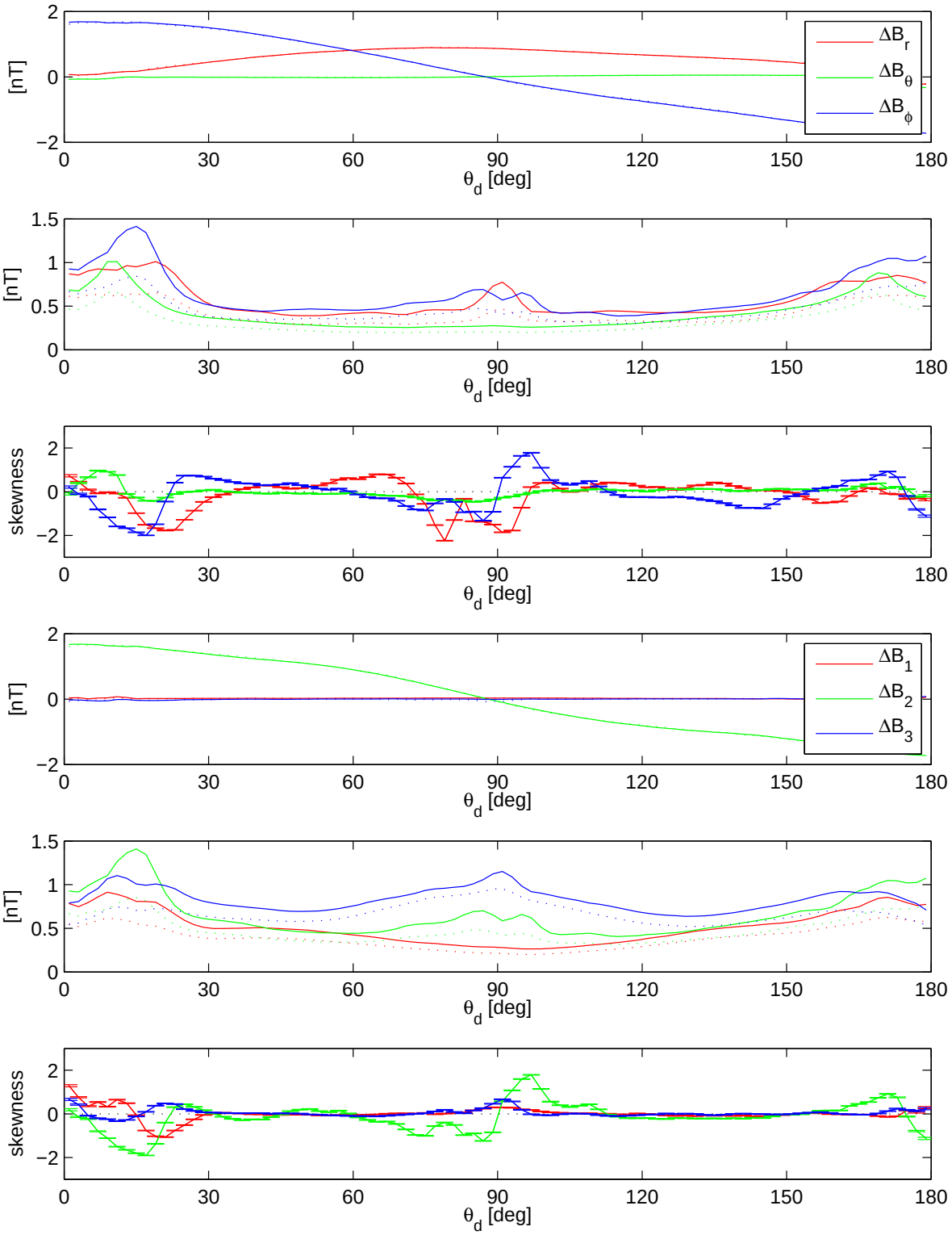

Figure 8.11: Top 3 panels: Mean (solid curve) and median (dashed), standard deviation (solid) and MAD (dashed), and skewness, of the residuals of failure case 2b in the NEC frame, in dependence on dipole co-latitude θ_d. Bottom 3 panels: Similar, but residuals in the VFM frame.

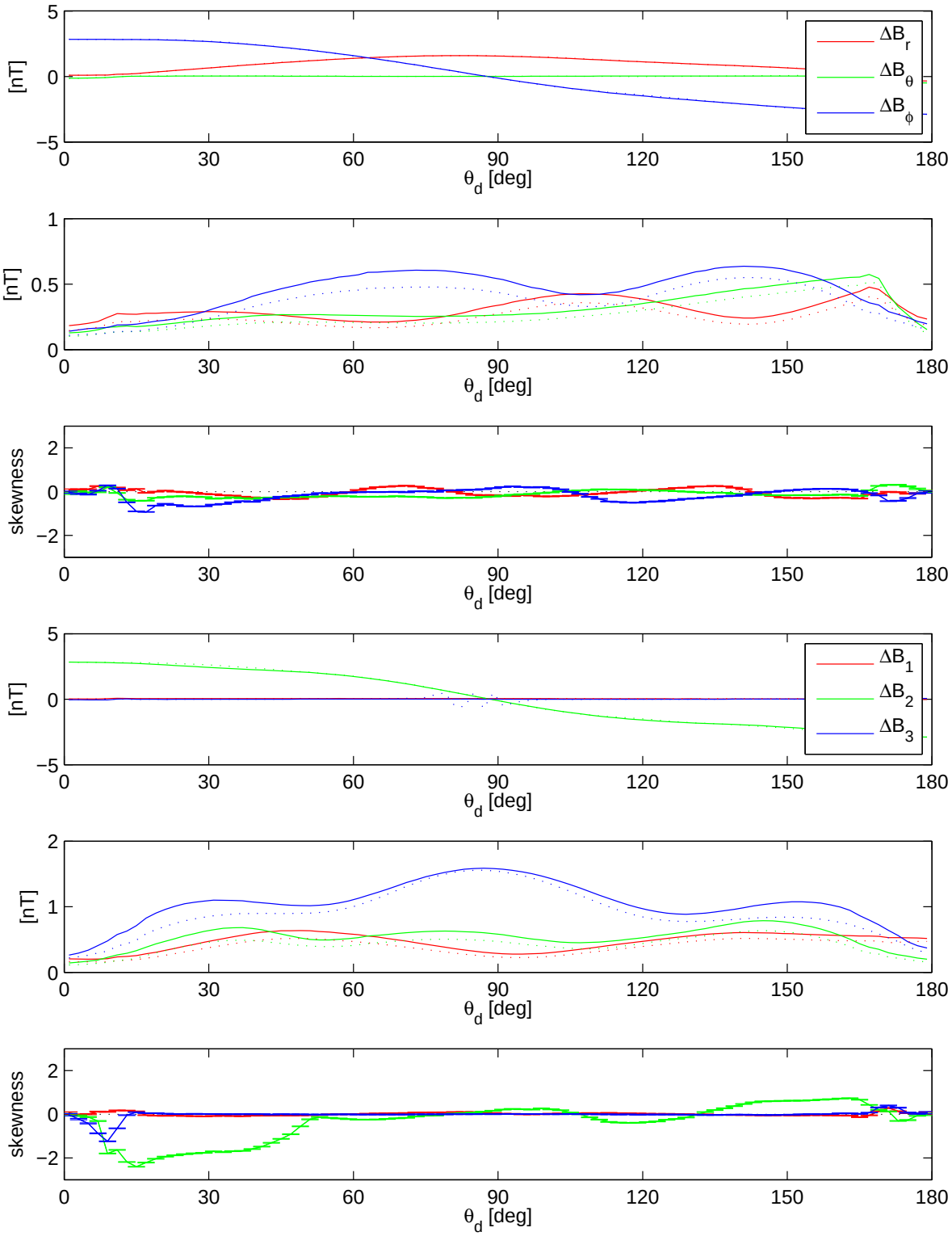

Figure 8.12: Similar to Fig. 8.11, but for the difference of the residuals of *Swarm A - B*.

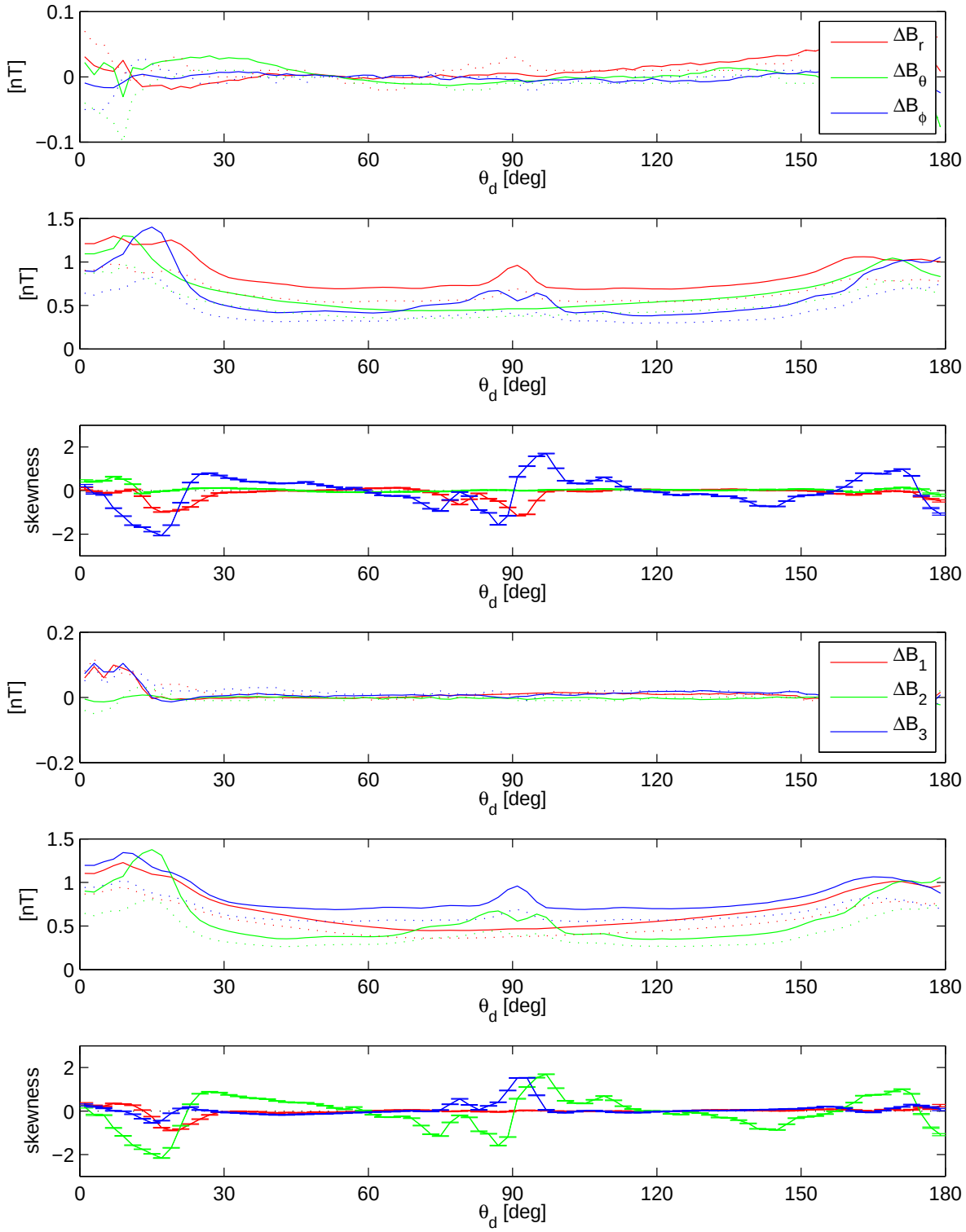

Figure 8.13: Top 3 panels: Mean (solid curve) and median (dashed), standard deviation (solid) and MAD (dashed), and skewness, of the residuals of failure case 2c in the NEC frame, in dependence on dipole co-latitude θ_d. Bottom 3 panels: Similar, but residuals in the VFM frame.

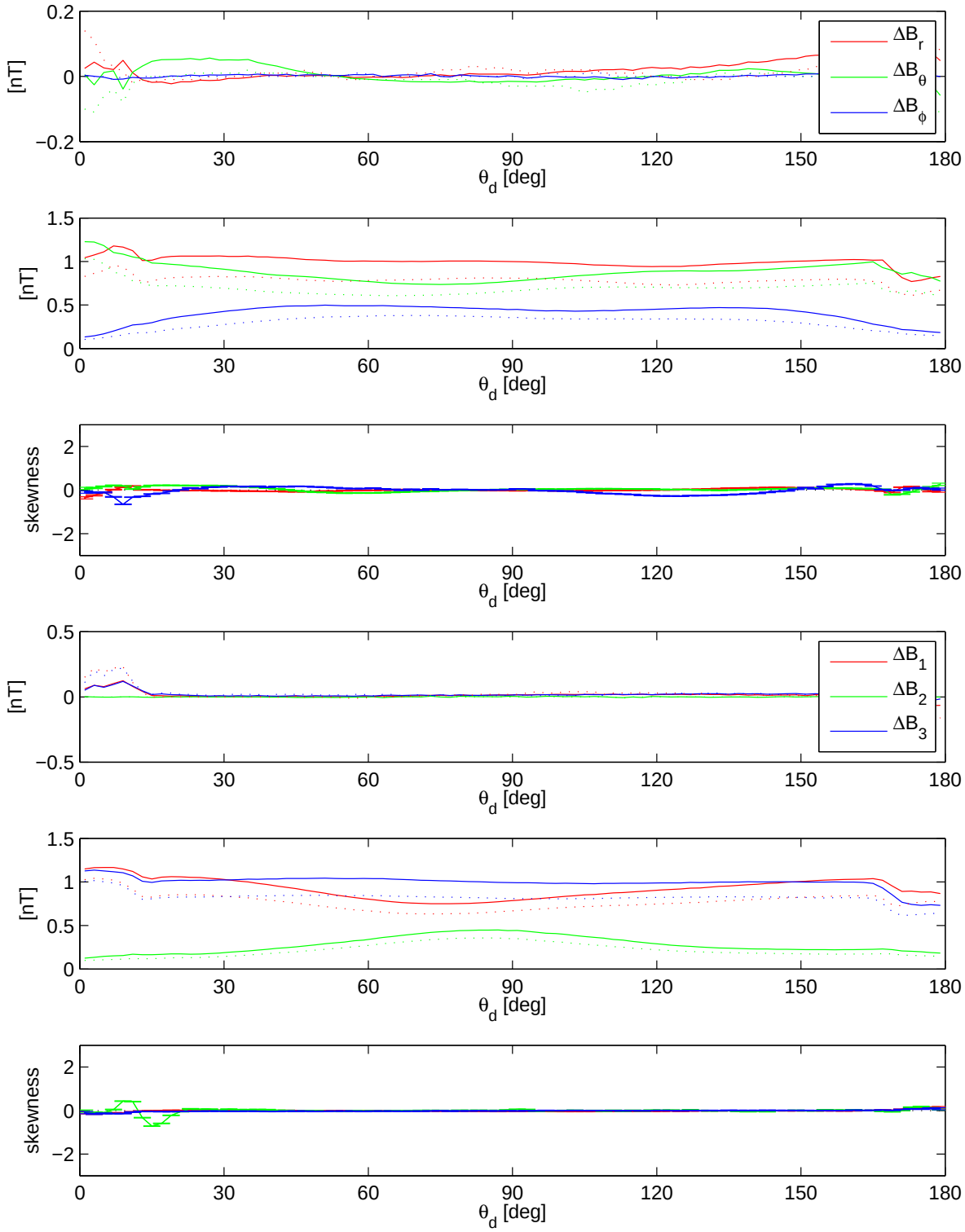

Figure 8.14: Similar to Fig. 8.13, but for the difference of the residuals of *Swarm A - B*.

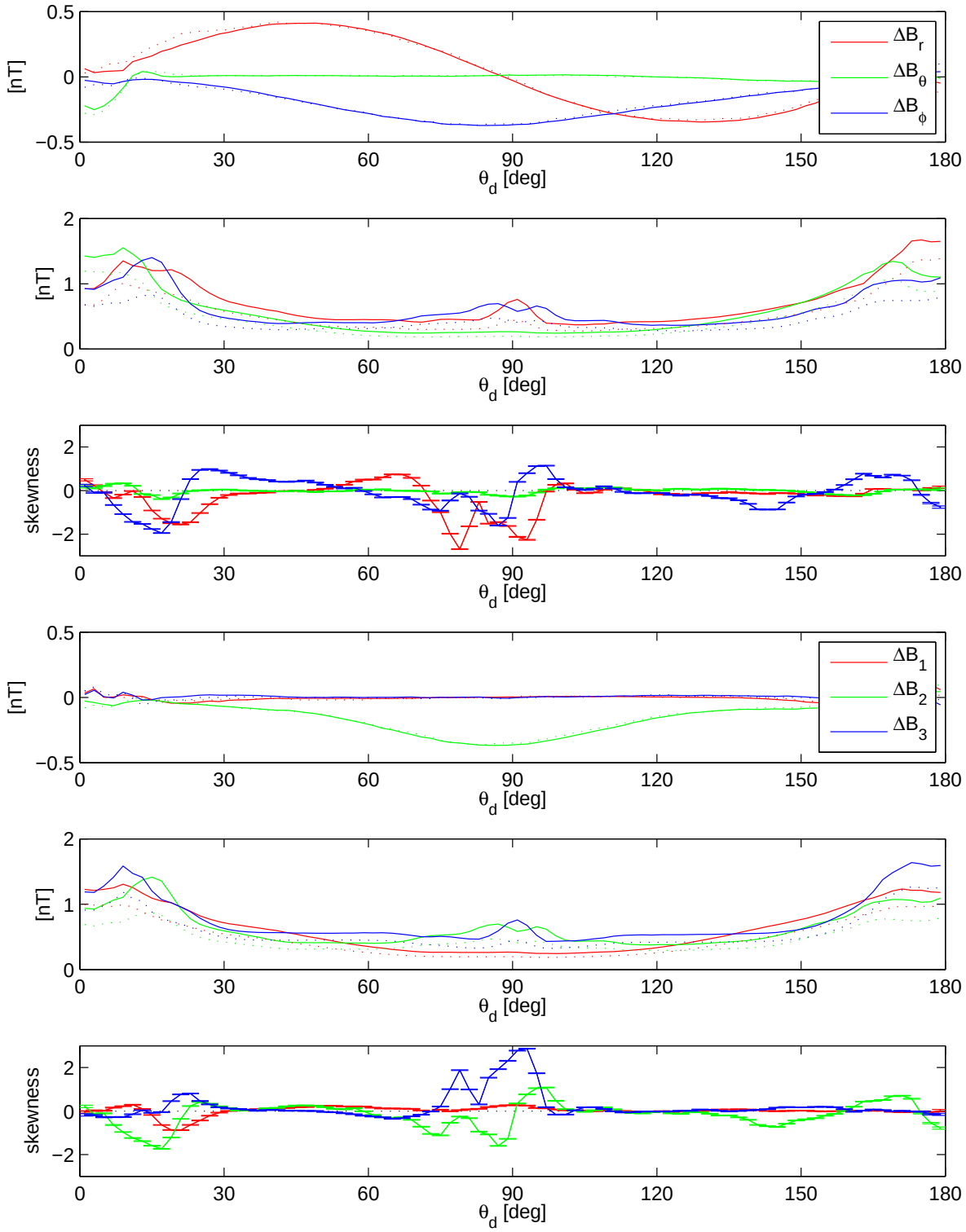

Figure 8.15: Top 3 panels: Mean (solid curve) and median (dashed), standard deviation (solid) and MAD (dashed), and skewness, of the residuals of failure case 3a in the NEC frame, in dependence on dipole co-latitude θ_d. Bottom 3 panels: Similar, but residuals in the VFM frame.

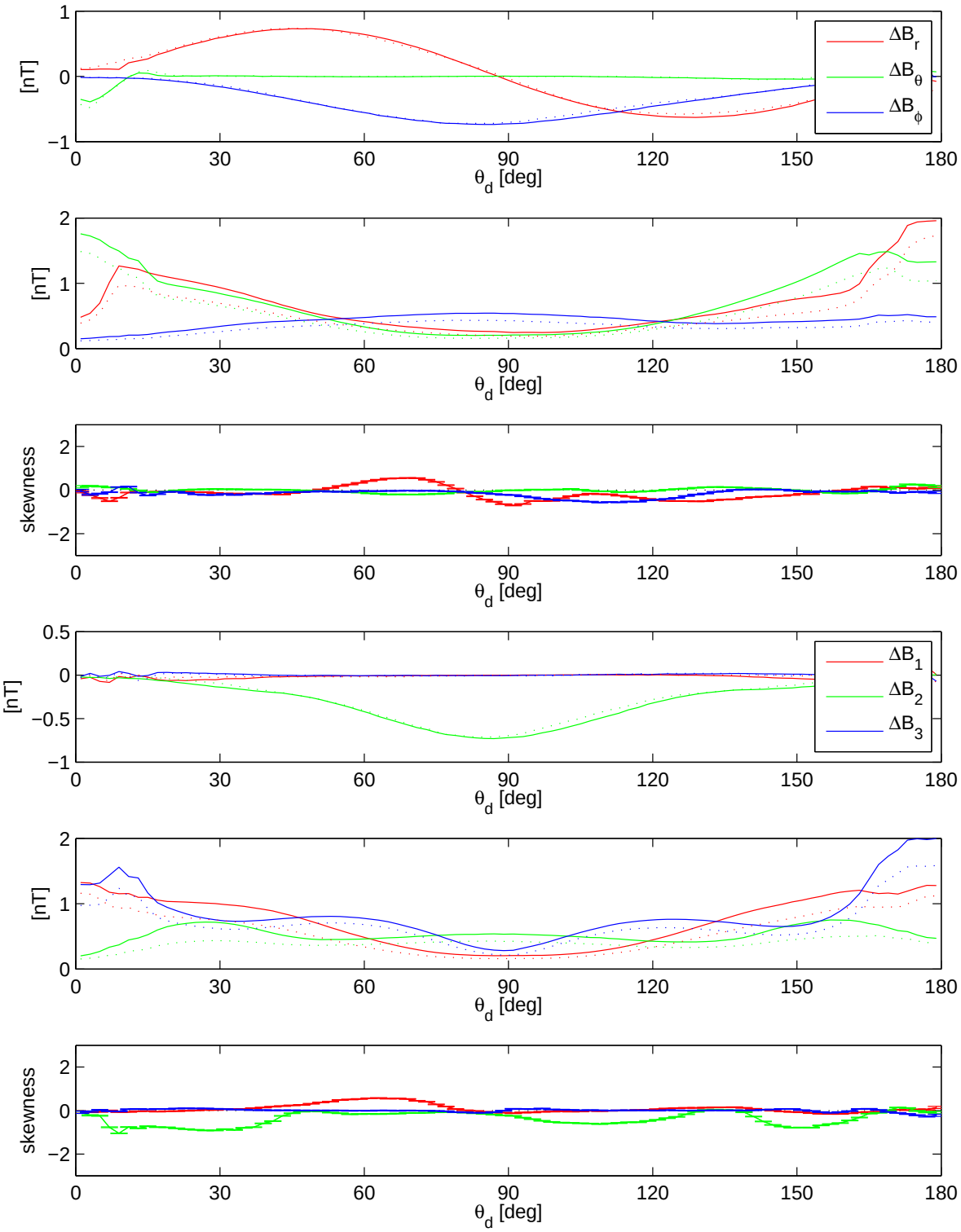

Figure 8.16: Similar to Fig. 8.15, but for the difference of the residuals of *Swarm A - B*.

Chapter 9

Summary and Recommendations

The goal of the present study is twofold:

- to modify the *Comprehensive Inversion* approach to include a multi-satellite alignment and to account for differences of the magnetic vector observed by the lower satellite pair *Swarm A* and *B* for improved lithospheric field recovery;
- to investigate the impact of various failure and imperfection cases on mission performance.

As a result of the first part of the study it was possible to significantly improve the results obtained during Phase A of the mission, in the so-called E2E mission performance study [Olsen et al., 2004], especially concerning recovery of the high-degree crustal field. Under the idealistic assumption of perfectly aligned vector data, and including data at altitudes lower than 300 km, the approach developed during Phase A allows for recovery of the the lithospheric field up to spherical harmonic degree $n = 133$. In the present study we could improve this to a recovery at least up to $n = 150$, even with data that are not properly aligned. When restricted to altitudes above 300 km, field recovery up to $n = 140$ or so is possible.

The proper alignment of the vector data (i.e. their transformation from the instrument frame to the Earth-Centered-Earth-Fixed NEC frame), which was identified during Phase A of the mission as an outstanding problem, could be solved. The approach derived in the present study allows for a determination of the alignment (Euler angles of VFM/STR rotation) with mean values and standard deviation well below 1 arcsec.

The developed approach has been applied to various mission failure and imperfection cases in the second part of the study. Although in this study only the impact of mission failures on core and lithospheric field recovery (which are two out of three main science objectives of *Swarm*) were investigated explicitly, conclusions about the expected degradation of the mission regarding the other science objectives can be drawn based on the obtained recovery of the magnetometer alignment angles and the magnetospheric/induced field correlation. It seems likely that none of the investigated failure cases will fulfill *all* mission science objectives; as opposed to the proposed mission baseline.

Based on the experience gained during the present study we suggest the following topics for future investigations:

1. Account for non-Gaussian error distribution by means of *Iteratively Reweighted Least Squares* with Huber weights when estimating the model parameters in the *Comprehensive Inversion*.

2. Further investigate some of the failure cases to see if a more advanced treatment could help improve mission objectives. In particular, failure cases 2 and 3 deal with the addition of non-standard magnetic and attitude noise. In the present study these noise sources were simply treated as if they didn't exist. However, a more sophisticated approach, for instance a multi-satellite calibration of the VFM magnetometers, could improve these results.

3. The minimal mission specifications call for a stable constellation to the point where the lower satellite pair reach 300 km altitude. We know that crustal field sensitivity is greatly enhanced as altitude decreases. This happens as a function of spherical harmonic degree n. Until now, only difference and sum combinations of the lower vector magnetometer pair have been exploited for enhancing crustal resolution. However, other combinations, such as along-track or radial differencing, may be able to further enhance this recovery and hence mitigate the effects of not reaching lower altitudes.

4. Looking at radial differences is especially interesting in this context, since it results in higher sensitivity wrt. spherical harmonic degree n, compared to the use of East-West differences (as done in the present study), which amplifies sensitivity of spherical harmonic order m. If it turns out that radial differences will improve high-degree crustal field recovery, one could increase the number of high-low crossover-points by selecting satellite inclination such that the local time difference between the lower pair and the upper satellite reaches 12 hours within mission duration.

5. Although the *Swarm* constellation will provide unparalleled samplings of the magnetic field, other cotemporaneous data will also exist; the observatories. None of the scenarios investigated in the present study includes a co-analysis of these data. It may be that this data set will help in a better characterization of not only the core field, but external and induced fields as well.

6. Additional information on the space-time structure of the residuals (and hints on which signal is not modelled properly) might be gained from an EOF analyis of the residuals. Also, an eigen decomposition of the residual covariance matrices might illuminate which vector (or gradient) combinations are most contaminated.

Bibliography

C. G. Constable. Parameter estimation in non-gaussian noise. *Geophys. J.*, 94:131–142, 1988.

W. Flury. Vorlesung Raumfahrtmechanik. Lecture Notes, Technical University Darmstadt and ESOC, October 2000.

A. E. Hedin. MSIS-86 thermospheric model. *J. Geophys. Res.*, 92:4649–4662, 1987.

A. E. Hedin. Extension of the MSIS thermosphere model into the middle and lower atmosphere. *J. Geophys. Res.*, 96:1159–1172, 1991.

P. Holland and R. Welsch. Robust regression using iteratively reweighted least-squares. *Commun. Statist. – Theor. Meth.*, 6:813–827, 1977.

R. A. Langel and W. J. Hinze. *The magnetic field of the Earth's lithosphere: The satellite perspective*. Cambridge University Press, 1998.

H. Liu and H. Lühr. Strong disturbance of the upper thermospheric density due to magnetic storms: CHAMP observations. *Journal of Geophysical Research (Space Physics)*, 110(A9): A09S29, Aug. 2005.

N. Olsen, E. Friis-Christensen, G. Hulot, M. Korte, A. V. Kuvshinov, V. Lesur, H. Lühr, S. Macmillan, M. Mandea, S. Maus, M. Purucker, C. Reigber, P. Ritter, M. Rother, T. Sabaka, P. Tarits, and A. Thomson. *Swarm* - End-to-End mission performance simulator study, ESA contract No 17263/03/NL/CB. DSRI Report 1/2004, Danish Space Research Institute, Copenhagen, 2004.

N. Olsen, H. Lühr, T. J. Sabaka, M. Mandea, M. Rother, L. Tøffner-Clausen, and S. Choi. CHAOS - a model of Earth's magnetic field derived from CHAMP, Ørsted, and SAC-C magnetic satellite data. *Geophys. J. Int.*, 166:67–75, 2006.

N. Olsen, T. J. Sabaka, and L. Tøffner-Clausen. Determination of the IGRF 2000 model. *Earth, Planets and Space*, 52:1175–1182, 2000.

N. Olsen, L. Tøffner-Clausen, T. J. Sabaka, P. Brauer, J. M. G. Merayo, J. L. Jørgensen, J.-M. Léger, O. V. Nielsen, F. Primdahl, and T. Risbo. Calibration of the Ørsted vector magnetometer. *Earth, Planets and Space*, 55:11–18, 2003.

W. H. Press, B. P. Flannery, S. A. Teukolsky, and W. T. Vetterling. *Numerical Recipes*. Cambridge University Press, Cambridge, 1992.

T. J. Sabaka and N. Olsen. Enhancing comprehensive inversions using the *Swarm* constellation. *Earth, Planets and Space*, 58:371–395, 2006.

G. Seeber. *Satellite Geodesy*. Walter de Gruyter, Berlin - New York, 2004.

J. R. Wertz and W. J. Larson, editors. *Space Mission Analysis and Design*. Kluwer Academic Publishers, 1999.